# DOMECair 2013
# Final Report

ESTEC Contract No. 4000107850/13/NL/FF/lf

## DOMECair Campaign EMIRAD Data: Presentation & Analysis

Steen S. Kristensen, Sten S. Søbjærg, Jan E. Balling, and Niels Skou

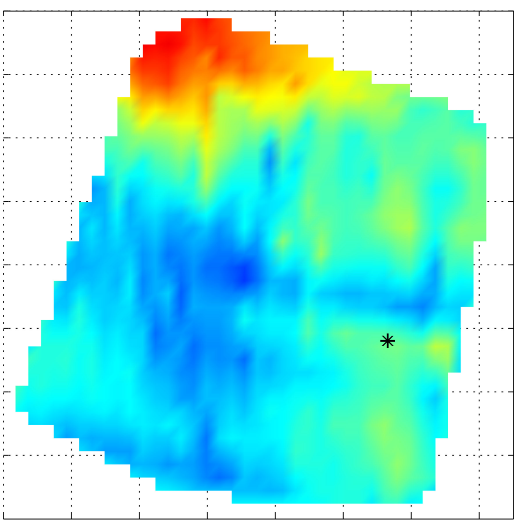

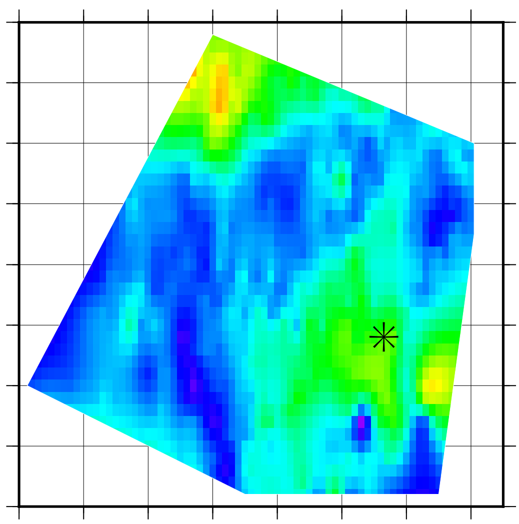

# Introduction

The airborne survey DOMECair 2013 and its instrumentation was designed to obtain calibration and validation data for two different satellite missions of ESA's Earth Explorer mission, for satellites SMOS and GOCE. As area of investigation a 300 km by 300 km large area near the French-Italian wintering station Concordia on Dome C in East Antarctica was chosen. The instrumentation of the research aircraft consisted of the radiometer EMIRAD-2 by DTU Space, a modified LaCoste-Romberg gravity meter, a Riegl laser scanner, nadir foto camera, several geodetic GPS receivers, an IMU unit, and a basic data acquisition system recording the data of the aircraft's INS unit.

The region was covered by 11 parallel survey lines, a so-called tie line, and a star pattern. Furthermore two flights with two sets of ten circles each were flown for calibration of EMIRAD-2. The tie-line is a requirement of the gravity survey. Cross-over poins are needed for estimating data quality. The star-patern was centered on the DOMEX observation tower at Concordia station. All flown survey lines are shown in Figure 1.

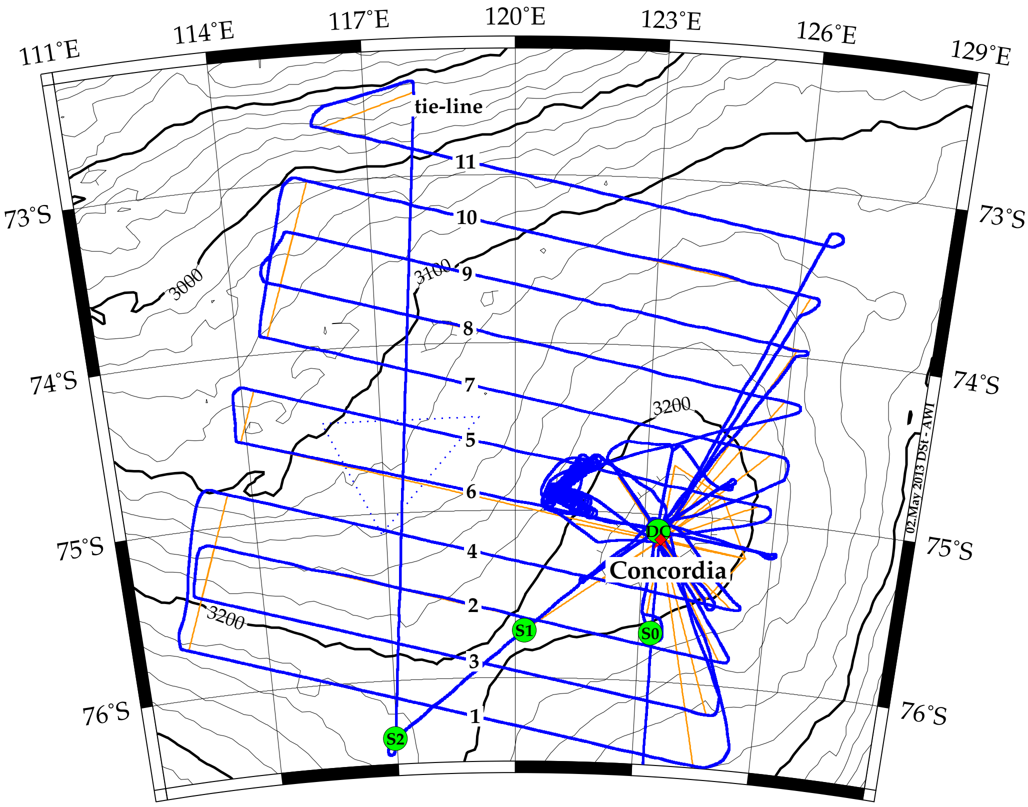


**Figure 1**: Flown profiles of the DOMCair 2013 survey. The line spacing the parallel is 30 km, the length of lines is 300 km.

Therefore two final reports have been compiled, one focusing on the EMIRAD data and the other on the gravity data:

- DOMECair Campaign EMIRAD Data: Presentation & Analysis
  Steen S. Kristensen, Sten S. Søbjærg, Jan E. Balling, and Niels Skou
  DTU-Space, Denmark
  September 10th 2013, 114 pages including title page

- Dome-C airborne gravity measurements and comparison to GOCE
  Daniel Steinhage, Graeme Eagles AWI-Bremerhaven, Germany
  Rene Forsberg, Hasan Yildiz*, DTU-Space, Denmark
  $*$ at General Command of Mapping, Ankara, Turkey
  DEC 2013, 21 pages including title page
  and 2 pages appendix on airborne laser scanner processing

# DOMECair Campaign
# EMIRAD Data: Presentation & Analysis

Prepared by

Steen S. Kristensen, Sten S. Søbjærg, Jan E. Balling, and Niels Skou

DTU Space

September 10th 2013

## DISTRIBUTION LIST

| Name | Organization | Issue | Date |
|---|---|---|---|
| Susanne Mecklenburg | ESA | 1.1 | 10/9/13 |
| Malcolm Davidson | ESA | 1.1 | 10/9/13 |
| Tânia Casal | ESA | 1.1 | 10/9/13 |
| Matthias Drusch | ESA | 1.1 | 10/9/13 |
| Daniel Steinhage | AWI | 1.1 | 10/9/13 |
| Giovanni Macelloni | IFAC | 1.1 | 10/9/13 |
| Sten Søbjærg | DTU-Space | 1.1 | 10/9/13 |
| Niels Skou | DTU-Space | 1.1 | 10/9/13 |
| Jan Balling | DTU-Space | 1.1 | 10/9/13 |
| Steen Savstrup Kristensen | DTU-Space | 1.1 | 10/9/13 |

## DOCUMENT CONTROL DATA

| Issue | Revision | Date | Description |
|---|---|---|---|
| 1 | 0 | 26/8/13 | Draft |
| 1 | 1 | 10/9/13 | Revised with ESA comments |

## TABLE OF CONTENTS

## 1. INTRODUCTION

In November 2009, SMOS was launched with the purpose of measuring sea-surface salinity and soil moisture by means of L-band radiometry.

In search of a stable, well characterized Earthly calibration check point, the East Antarctic Plateau around Dome C, with the Concordia station, has been identified as an interesting candidate. Temporal stability has been investigated within the DOMEX framework, using a tower based L-band radiometer situated near Concordia [Giovanni et al, 2013]. In January 2013 an airborne campaign using the L-band radiometer EMIRAD-2 [Søbjærg et al, 2013], the DOMECair campaign, was carried out with the aim of investigating the spatial homogeneity of the area [Skou and Forsberg, 2012].

The present report presents the EMIRAD-2 L-band data, and a first level analysis hereof.

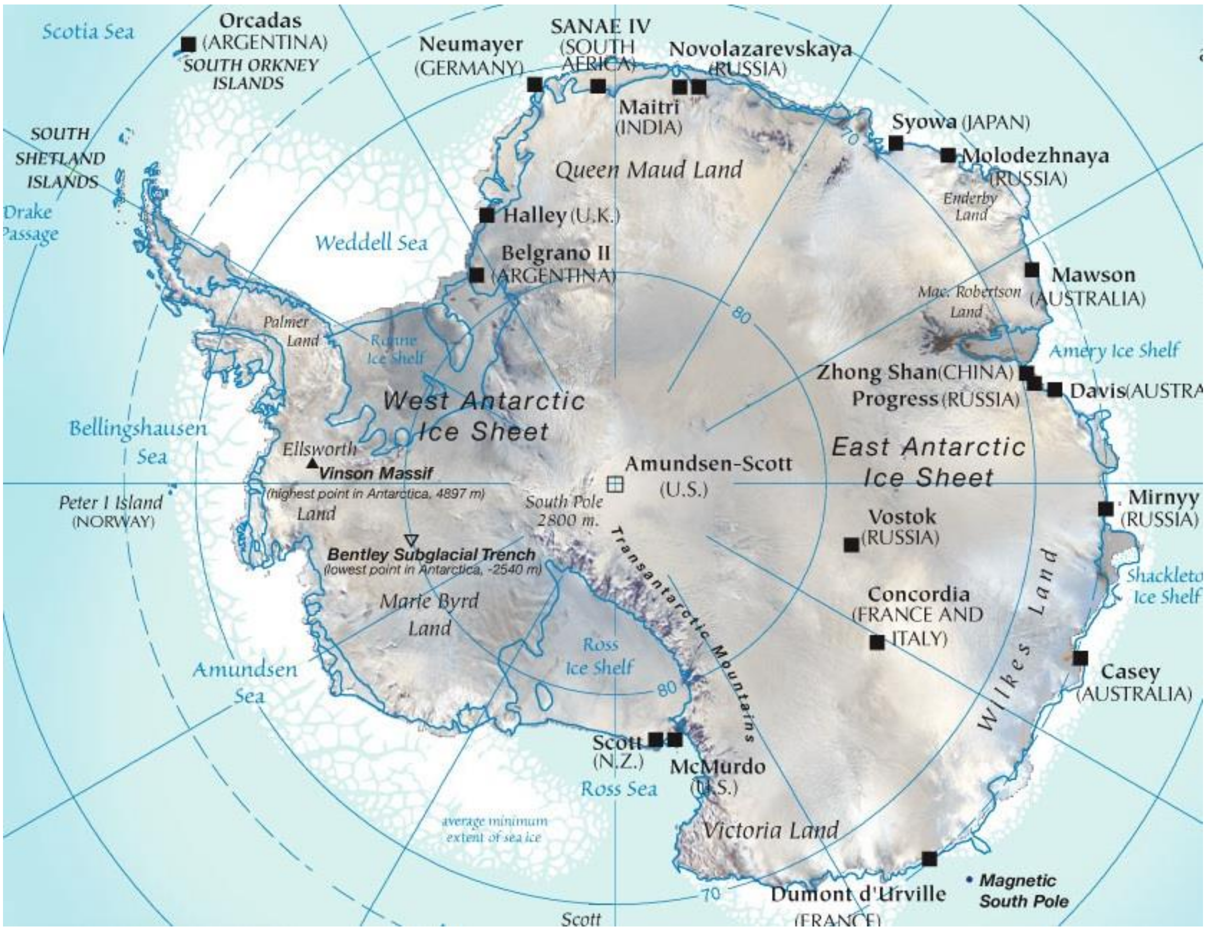


Figure 1.1: Antarctica

## 2. PLANNED FLIGHT PATTERN

This chapter is in fact an abbreviated copy of what was presented in the Campaign Implementation Plan, but its contents is deemed so crucial for understanding the discussion in the following chapters, that it is repeated here.

In order to evaluate the homogeneity of the area around Dome-C, the raster pattern shown in Figure 2.1 was flown (red lines). The area around Concordia is covered by a grid of 11 each 350 km long lines, separated by 35 km. Thus an area of 350 x 350 km is covered. These major grid lines are numbered 1 to 11, line 1 being closest to the South Pole. The area encompasses the Concordia area as well as Giovanni's optimal calibration triangle. In order to properly cover the area around the Concordia tower based measurements, the lines starts 50 km before Concordia. For this relatively flat and quasi-homogeneous area, the actual altitude is not so important, and radiometer measurements were carried out at constant flight level enabling the simultaneous recording of gravimetric data. The altitude above terrain was roughly 600 m.

Each line is so long that only 2 lines can be flown per mission. This means that 5 missions are required to cover 10 lines, which is indicated in Figure 2.1. In addition to this, a single, far away line followed by a tie line crossing all other lines (for inter-comparison) is shown.

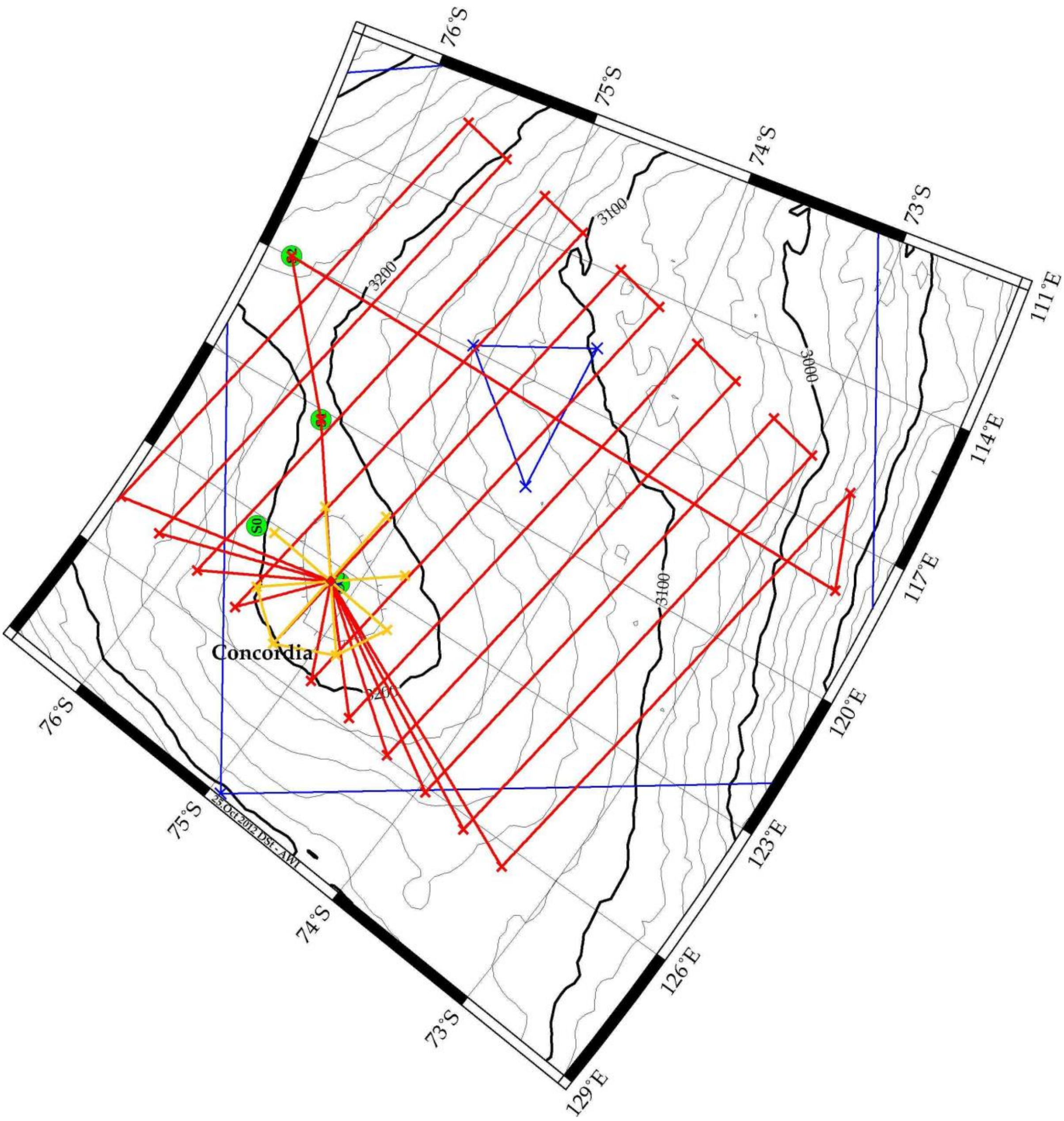


Figure 2.1: Raster pattern (red) and star pattern (yellow)

Normally during CoSMOS, flights were carried out before dawn in order to totally exclude possible Sun interference. This is not possible for the present campaign where the Sun is always above the horizon. But over the ice cap the situation is benign compared with the CoSMOS ocean situation: we expect moderate reflected Sun from the surface since this is closer to a blackbody than is the ocean. The DOMEX-2 experiment indeed indicates Sun signals of some magnitude, especially at H polarization, such that we have to take them into consideration. In addition we have to take into account direct radiation into the antennas via sidelobes. The EMIRAD-2 antennas are Potter horns in principle without sidelobes. However, when installed into the metallic airframe this cannot be guaranteed, but very low levels are expected. Thus the direction of the raster pattern lines combined with the time of radiometer data acquisition was planned such that the Sun is never in an angular sector 100° ± 45° compared to the flight lines (the offset horn looks starboard, 10° aft, and the full main beam is ±45°). As the Sun moves around by 360° in 24 hours, this means that there is a forbidden time slot at 11:20 ±3 hours had the lines been east-west. The pattern is rotated by 15 deg. (≈ 1 hour), and thus the forbidden time slot is 7:20 to 13:20. It was therefore planned to take off at 13:30 when covering the lines in the raster pattern. This schedule is also very compatible with the requirements for adequate time for heating and temperature stabilizing the radiometer before use. Irrespective of how well operations try to avoid Sun effects, they will have to be evaluated and possibly compensated, see sub-section about circle flights.

The area around the tower is covered more intensely by the star pattern also shown in Figure 2.1 (yellow). The lines are 100 km long. By careful planning it is possible to avoid the Sun into the starboard looking horn on all the straight lines.

In order to assess any azimuth signatures circle flights was conducted (Not shown in Figure 2.1). These consist of a total of 10 + 10 circles (right-hand and left-hand) with constant banking angles of +10 deg. and -10 deg., respectively. Constant roll and pitch angles are important, and thus the aircraft was be left to drift with the wind rather that the pilots trying to circle around a fixed point.

Finally, several wing wags were carried out for calibration purposes. Those were generally performed when flying from one line to another, in order not to disturb the data from the proper lines.

# 3. RADIOMETER DATA CALIBRATION AND INITIAL PROCESSING

This chapter describes the calibration of the radiometer data, validation of this calibration and some initial processing.

## 3.1 Radiometer calibration

The EMIRAD radiometer data is calibrated in several steps, which will be discussed in the following sections. The basic output from the radiometer is a set of files, containing only binary numbers. Data is collected through two analog-to-digital converters (ADC), which follow directly after the analog radiometer section. The analog section amplifies and filters the data. Data from the two converters represent the two linearly polarized channels, V-Pol and H-pol, and samples represent $E_{XM}=A_X(E_X+E_{XN})$, where $E_{XM}$ is the measured data, $E_X$ is the incident electric field to the antenna, $E_{XN}$ is the receiver noise contribution, and $A_X$ is the receiver voltage gain, and where X is replaced by either V or H for each of the two polarizations.

The digital section calculates the four basic outputs, $<E_{VM}\,E_{VM}^*>$, $<E_{HM}\,E_{HM}^*>$, $<Re(E_{VM}\,E_{HM}^*)>$, $<Im(E_{VM}\,E_{HM}^*)>$, where <> represents integration to 1 ms, and * represents complex conjugation. Furthermore the digital section provides output products for kurtosis estimation as well as housekeeping data, such as temperature measurements at 16 different points within the receiver, and power supply voltages. For the calibration procedure, temperature measurements are the only important parameters, and hence no further detailed discussion about the data format will be made.

From the output products, the four modified Stokes parameters, ($T_V$, $T_H$, U, V), can be derived. The relation between the incident electric field and the brightness temperatures is shown in the left side of equations 1a-1d, where $\lambda$ is the wavelength, k is Boltzmann's constant and z is the impedance of the medium of wave propagation. The second equal sign follows, as the incident electric field and the receiver noise contributions are statistically independent. The right most equal sign is a simple variable substitution, showing how the desired parameters may be derived from a Gain factor, $G_X$, and an offset term, representing the receiver noise temperature, $T_{NX}$, for each of the two polarizations, respectively.

$$T_V = \frac{\lambda^2}{kz}\left\langle E_V^2 \right\rangle = \frac{\lambda^2}{kz}\left( \frac{1}{A_V^2}\left\langle E_{VM} E_{VM}^* \right\rangle - \left\langle E_{VN} E_{VN}^* \right\rangle \right) = \frac{1}{G_V}\left\langle E_{VM} E_{VM}^* \right\rangle - T_{NV} \quad (1a)$$

$$T_H = \frac{\lambda^2}{kz}\left\langle E_H^2 \right\rangle = \frac{\lambda^2}{kz}\left( \frac{1}{A_H^2}\left\langle E_{HM} E_{HM}^* \right\rangle - \left\langle E_{HN} E_{HN}^* \right\rangle \right) = \frac{1}{G_H}\left\langle E_{HM} E_{HM}^* \right\rangle - T_{NH} \quad (1b)$$

$$U = \frac{\lambda^2}{kz}\left\langle 2\,\mathrm{Re}\left( E_V E_H^* \right) \right\rangle = 2\frac{\lambda^2}{kz}\left( \frac{1}{A_V A_H}\mathrm{Re}\left\langle E_{HM} E_{HM}^* \right\rangle \right) = 2\frac{1}{\sqrt{G_V G_H}}\mathrm{Re}\left\langle E_{HM} E_{HM}^* \right\rangle \quad (1c)$$

$$V = \frac{\lambda^2}{kz}\left\langle 2\,\mathrm{Im}\left( E_V E_H^* \right) \right\rangle = 2\frac{\lambda^2}{kz}\left( \frac{1}{A_V A_H}\mathrm{Im}\left\langle E_{HM} E_{HM}^* \right\rangle \right) = 2\frac{1}{\sqrt{G_V G_H}}\mathrm{Im}\left\langle E_{HM} E_{HM}^* \right\rangle \quad (1d)$$

In total, the equations demonstrate how the binary output product is directly transferred into **all four desired Stokes parameters**, using only two gain factors and two offset terms $G_V$, $G_H$, $T_{NV}$, and $T_{NH}$ like in a traditional dual polarized radiometer.

If a component is present in front of the receiver, the incident brightness temperature is modified. For a lossy component, equation 2a describes the relation between the incident antenna brightness temperature, $T_A$, and the actually measured brightness temperature, $T_M$, where $T_P$ is the physical temperature of the component, and $S_{21}$ is the transmission coefficient (loss expressed as a gain, smaller than 1). For loss less reflective components (mismatched microwave components) equation 2b gives the relation. $S_{22}$ is the reflection coefficient, and $T_R$ is the radiated noise temperature from the receiver, and for this component type the relation $S_{21}$=(1-$S_{22}$) may be used. For the EMIRAD radiometer configuration, $T_R$ equals the physical temperature of the input circulator, measured within the housekeeping data package. $S_{21}$ and $S_{22}$ can be determined using a VNA (Vector Network Analyzer) as well as through external calibration.

$$T_M = S_{21} T_A + \left(1 - S_{21}\right) T_P \quad (2a)$$

$$T_M = S_{21} T_A + S_{22} T_R \quad (2b)$$

For components, which are both lossy and reflective, the equations must be combined, and very special care shall be taken, that $S_{21}$ is split up, so that the (1-$S_{21}$) factor in equation 2a ONLY accounts for the Ohm'ic loss.

For correct measurements of the third and fourth Stokes parameters, U and V, respectively, both receiver channels must have equal phase length. For a small phase difference, $\phi$ (like in EMIRAD, where fringe washing effects may be neglected), the actually measured parameter set, $\bar{T}_B'$, relative to the true parameter set, is found from equation 3. Knowing the actual phase imbalance from calibration, the measured data can easily be corrected through simple matrix inversion of the equation.

$$\overline{T_B}' = \begin{bmatrix} T_V' \\ T_H' \\ U' \\ V' \end{bmatrix} = \begin{bmatrix} T_V \\ T_H \\ U * \cos(\varphi) + V \sin(\varphi) \\ -U * \sin(\varphi) + V \cos(\varphi) \end{bmatrix} = \begin{bmatrix} T_V \\ T_H \\ U \\ V \end{bmatrix} \begin{bmatrix} 1 & 0 & 0 & 0 \\ 0 & 1 & 0 & 0 \\ 0 & 0 & \cos(\varphi) & \sin(\varphi) \\ 0 & 0 & -\sin(\varphi) & \cos(\varphi) \end{bmatrix} \quad (3)$$

## 3.2 Internal calibration

The first calibration step is internal calibration of the radiometer receiver itself, based on equations 1a-1d. In each channel the receiver has a low-loss switch at the input, which selects one of the four input sources: Antenna A (nadir looking horn), Antenna B (side looking horn), Matched load (ML), or Active cold load (ACL). Furthermore a common noise diode (ND) is coupled to the two receiver channels, enabling addition of a known amount of noise on top of the selected source. The feeding network for the noise from the noise diode, which is a purely passive network, is phase matched to better than 1 degree, hence enabling calibration of the phase coherence of the two receiver channels as described above. All three calibration sources are temperature monitored, and the ACL as well as the ND have been characterized with respect to repeatability and temperature sensitivity. Both exhibit an extremely high repeatability, and no measurable changes are observed, even for longer storage or use times. Table 3.2.1 gives a survey of the sources in terms of expected brightness temperatures and temperature sensitivity coefficients. Although the ND is common to the two channels, losses are different through the two signal paths, and hence the sensitivities are not exactly equal.

| **Type** | **Brightness Temperature** | **Sensitivity** |
|---|---|---|
| ML, H-Pol | Physical temperature (individually measured)<br>318-323 K | +1.000 K/K |
| ML, V-Pol | | +1.000 K/K |
| ND, H-Pol | Input source + 141.02 @ $T_{physical}$ = 318.33 K | Input source + 0.144 K/K |
| ND, V-POl | Input source + 132.23 @ $T_{physical}$ = 318.33 K | Input source + 0.127 K/K |
| ACL, H-Pol | 60.294 @ $T_{physical}$ = 323.00 K | +0.669 K/K |
| ACL, V-Pol | 60.285 @ $T_{physical}$ = 323.00 K | +0.630 K/K |

*Table 3.2.1: Calibration sources, expected output and temperature sensitivity.*

For each channel, only two calibration points are required, and the main scheme is either ML/ACL or ML/ML+ND. For both schemes, the third calibration source is used for data validation. For this campaign, ML/ML+ND has been chosen, hence with ACL and ACL+ND as validation points. The ND is pulsed every second with a duty cycle of 20%, independent from the input switch position, and theoretically the gain calibration could be continuously adjusted. However, due to the risk of gain estimation errors caused by RFI, this option is not used, and ND observations are uniquely used during calibration events, when the input switch is set to either ML or ACL. For each calibration period, the calibration constants, G and $T_N$, can be determined, but for correct calibration at all observation times, calibration data is linearly interpolated between calibration events, and an individual set of G and $T_N$ is determined for each data point.

The time interval between calibration events depends on the stability of the radiometer receiver, which again is strongly dependent upon the temperature stabilization. A good impression of the receiver stability is obtained from estimation of the Allan deviation, i.e. the sample-to-sample variation, $\Delta T$, for different integration times, $\tau$. The radiometer is connected to a stable (internal target), and is left without calibration events throughout the whole test. For an ideal radiometer, $\Delta T$ will decrease by the square-root of N, when the integration period length is increased by a factor of N, but for very long integration times, a non-ideal radiometer adds a term to $\Delta T$ based on the internal drifts, and eventually this term will become dominant. For the EMIRAD H-channel, $\Delta T$ as a function of the integration time $\tau$ is seen in Figure 3.2.1, where the dotted line is the behavior of an ideal instrument. The non-linearity between 10 s and 500 s is mainly caused by the period of the temperature regulation system, while the increase from 500 s and beyond is caused by long-term component drifts. It is seen, that the radiometer stays around $\Delta T$=100 mK for a wide interval of observation times, and there is no indication, that drifts are significantly compromising data, when the receiver is only calibrated every 500-1000 s (8-16 minutes).

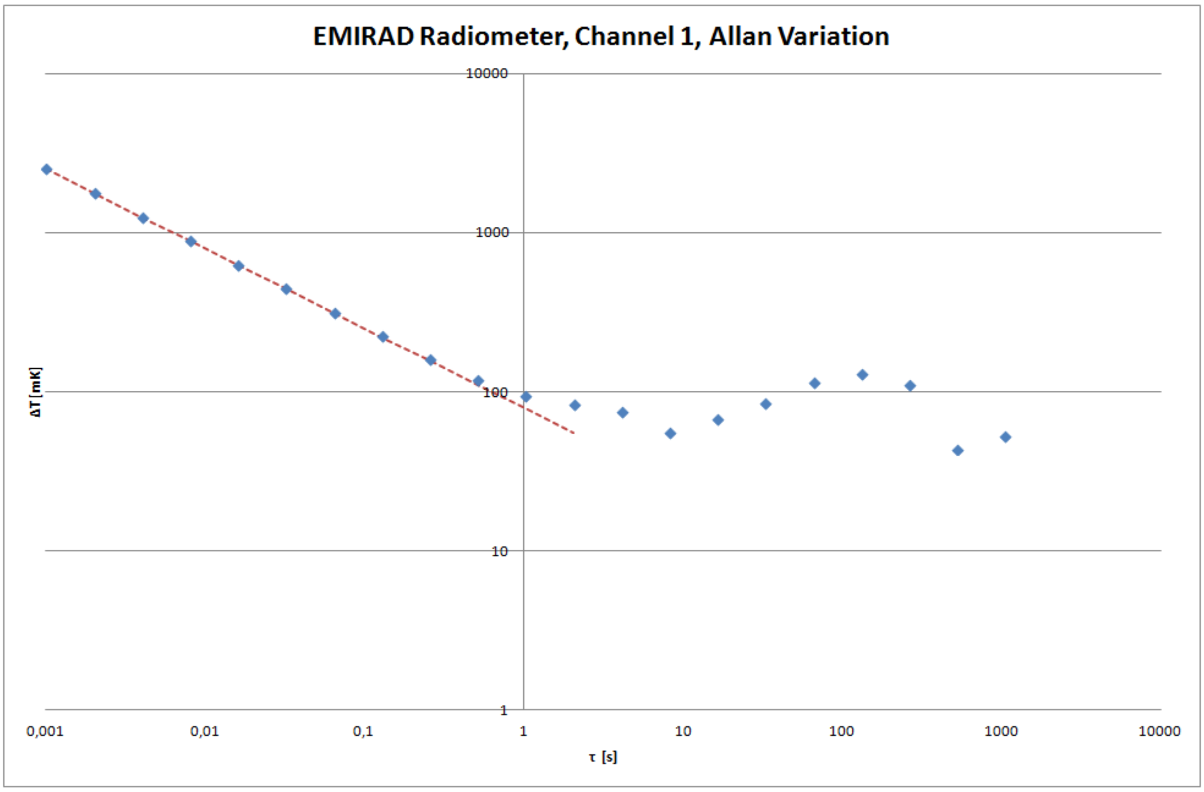


Figure 3.2.1: Allan Variation for EMIRAD H-channel.

Both receiver channels, i.e. the V-pol and the H-pol, are calibrated according to the same calibration procedure, and both channels exhibit similar sensitivities and drifts. The third and fourth Stokes parameters are calibrated according to equation 1c and 1d, using the gain, G, values determined for each of the main channels. Using the ML+ND observations, the actual phase imbalance between the two channels can be found, and through matrix inversion of equation 3, possible influence from imbalance can be removed down to errors of 1 degree. With the internal calibration, the radiometric observations are calibrated to the input connector of the instrument.

### 3.3 External calibration, microwave cables

The next calibration step takes the calibration reference from the instrument input connector to the end of the RF-cables, connecting the instrument to the antenna. RF-cables are very high quality Sucoflex 106 type cables, and typical $S_{21}$ values are in the range of 0.1 dB to 0.3 dB, depending on the cable length. $S_{21}$ is factory measured, and VNA-measurements verify the factory values. However, for radiometric applications, even higher accuracy is desired, and for this purpose, observation of a liquid Nitrogen cooled target is applicable. An Ailtech 7009 Standard Noise Generator, see Figure 3.3.1, which is a cryostat with a broadband matched load ($S_{11}$ < -34 dB), is used for the calibration procedure. Filling the cryostat with liquid Nitrogen yields a brightness temperature equal to the boiling point of the nitrogen, $T_{LN2}$=77.25-0.00825*(1013.25 HPa – p), where p is the air pressure. Finally inversion of equation 2a yields $S_{21}$ for the cable.

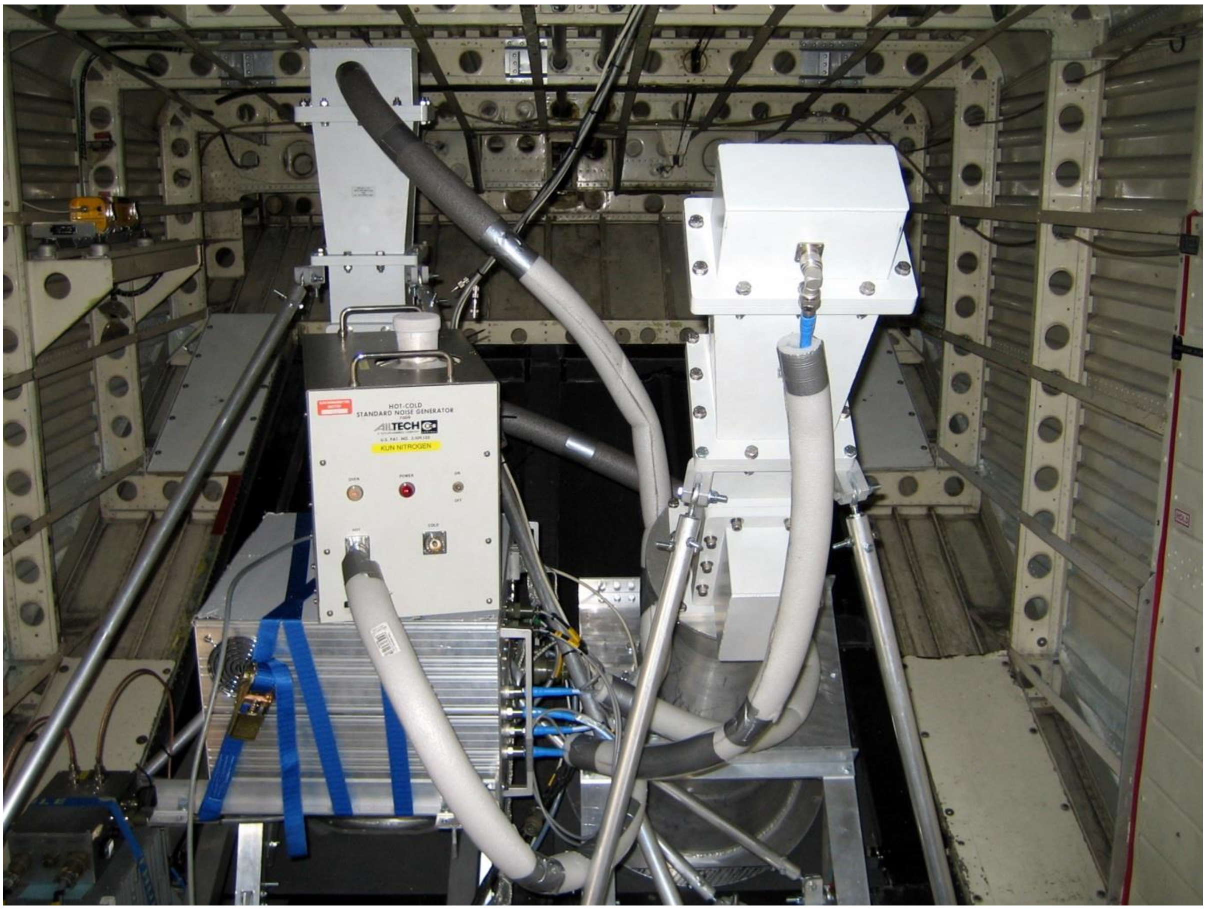


Figure 3.3.1: Ailtech 7009 Standard Noise Generator used for EMIRAD calibration

Theoretically this procedure should only be necessary once, as the cables are passive components, but the observations provide a good system check, and it ensures repeatability and comparability for data sets, taken over longer time intervals, e.g. the actual campaign. Furthermore it also removes any possible uncertainties within the instrument input switch, as the liquid nitrogen observations are made through the exact same signal path as the antenna measurements. Hence all four input cables (V-Pol and H-Pol for each of the two antennas) have been connected to the liquid Nitrogen cooled matched load at least once for each science flight, either prior to take-off or after landing, and a total of 11 liquid Nitrogen calibration events took place during the campaign. Cables were left mounted on the radiometer box through the whole campaign, and only the connector at the antenna/OMT was unmounted/remounted.

For each calibration event, the four $S_{21}$ values were calculated, and for almost all calibration events, the measurements were very consistent within ±0.01 dB. This consistence could not justify individual settings for each flight, as the deviations were of the level of measurement accuracy, and in this case individual settings could introduce artificial measurement deviations. Some outliers were identified during the last calibration event, and after the campaign it was understood, that the reason was a faulty input switch in one channel. The remaining estimates of the $S_{21}$ parameters were averaged for each cable, see Table 3.3.1, and results were found to be consistent with the numbers, provided by the manufacturer. It is noted, that horn B numbers are slightly higher than horn A numbers. This is simply explained by the length of the cables, as Horn B cables are 1,5 m long compared to the 1,0 m horn A cables. Also it is seen, that V-Pol numbers are lower than H-Pol numbers. This is a result of slightly different input switch performances, and again it is well in line with component parameters. Hence the numbers in Table 3.3.1 were used to adjust all measured data according to equation 2a.

| **Cable** | $\mathbf{S_{21}}$ |
|---|---|
| Horn A, H-Pol | -0.2206 dB |
| Horn A, V-Pol | -0.1352 dB |
| Horn B, H-Pol | -0.2913 dB |
| Horn B, V-Pol | -0.2208 dB |

*Table 3.3.1: Estimated cable losses.*

## 3.4 External calibration, antenna system

The last calibration step is to move the calibration reference from the RF-cable connectors to the antenna aperture, i.e. correcting for the influence from the antennas and the Orthomode Transducers (OMTs) using equation 2a and 2b. Prior to the campaign, measurements of $S_{21}$ and $S_{22}$ were made on a VNA, and results are seen in Table 3.4.1.

| **Port** | $S_{21}$ | $S_{22}$ |
|---|---|---|
| Horn A, H-Pol | -0.10 dB | -33.6 dB |
| Horn A, V-Pol | -0.08 dB | -21.0 dB |
| Horn B, H-Pol | -0.10 dB | -29.4 dB |
| Horn B, V-Pol | -0.08 dB | -20.1 dB |

*Table 3.4.1: Estimated S-parameters for the antenna system.*

Radiometer data is adjusted according to the equations, and values have been validated through measurements of the cold sky, using exactly the setup to be installed in the aircraft. Results confirmed expected sky brightness temperatures, and as no external calibration source is available after installation, the numbers were assumed to be constant – a fair assumption as the antenna system consists only of bulky metal structures. However, changes in the parameters due to the presence of the aircraft body itself are not accounted for, when applying this correction!

The OMT has a known phase imbalance between the two polarization ports equal to $\phi$ =-12.4 degrees, which causes the third and fourth Stokes parameters to mix as described by equation 3. Using matrix inversion on the equation, the effect is removed.

Any antenna will cause a coupling between orthogonal channels, known as cross polarization. As the cross polarization level is relatively low for the Potter horn antenna type, the effect is not significant for the pure $T_V$ and $T_H$ measurements at most targets and incidence angles. Only for very high incidence angles over the ocean, where the channels yield very different measurement values, some deviation can be seen. For a polarimetric radiometer, however, cross polarization will cause a false signal in the 3$^{rd}$ (or 4$^{th}$) Stokes parameter, equal to the signal, which would be caused by cross talk between channels. Unlike cross talk, the magnitude and sign of the false signal will vary over the footprint (different sign on opposite sides of boresight), and thus for a completely homogeneously illuminated foot print (e.g. nadir looking at a homogeneous target), the effect will fully cancel. For non-homogeneous target types, and/or when the incidence angle is large, i.e. when the two half-planes of the foot print are relatively different, the cross polarization effect may cause the 3$^{rd}$ Stokes parameter to shift several K. This effect is not corrected for, as it requires a forward model to predict the brightness temperatures of target, but as it affects only the 3$^{rd}$ Stokes parameter for some special cases, it is not considered a problem.

### 3.5 Determination of attitude parameters

During all flight operations navigation data is collected, using the Honeywell H-764 Embedded GPS/INS (EGI).The unit provides information about position (Latitude, Longitude and Altitude), and it also provides attitude data, i.e. pitch, roll and true heading, with an accuracy of 0.05 degrees and with an update rate of 50 Hz. For scientific purposes, this data must be transformed into traditional remote sensing parameters, such as incidence angle with respect to nadir, observation direction with respect to Earth North, and rotation of the antenna reference frame (Horizontal and Vertical linear polarizations) with respect to the true Earth Vertical and Horizontal directions.

This transformation requires detailed knowledge about the actual installation of the antennas in the aircraft, and during the installation process, each antenna probe (V-Pol and H-Pol) orientation is measured using the EGI, and finally the EGI itself is fixed and again readings are made. The EGI readings are used to specify the aircraft reference frame, and using the probe measurements, each antenna probe orientation can be expressed uniquely in this reference frame. For each scientific measurement point, the EGI readings are used to specify, how the aircraft reference frame is oriented within the Earth reference frame, and the actual co-ordinate transformation matrix can be generated. Using standard linear algebra, each antenna probe can be expressed in the Earth reference frame, and finally the desired parameters can be derived.

In the final EMIRAD data set, measured navigation data is provided along with the derived remote sensing parameters for easy data processing and application.

### 3.6 Data calibration validation using wing wags

The overall end-to-end calibration procedure, described in the previous sections, is basically the same procedure, which has been applied to earlier EMIRAD data sets, including the SMOS Cal/Val data, and the steps have been carefully validated as described in the sections. However, the overall end-to-end calibration cannot be completely validated, when the antennas are installed in the aircraft due to aircraft maneuvering limitations. This can be a problem, as antenna parameters – especially $S_{22}$ – may be affected by the presence of the aircraft body. To validate the data, it is necessary to overfly and radiometrically measure an area with known brightness temperature, e.g. a lake, where sea surface temperature and wind speed is carefully monitored. If the lake is sufficiently large, it will be possible to perform wing wags and nose wags, which is a large scale variation of aircraft pitch and roll, respectively, and still avoid influence on radiometric measurements from the lake shores. For a typical aircraft, it should be possible to reach at least ±10 degrees of pitch variation and ±25 degrees of roll variation. For the actual installation, this will provide coverage of incidence angles, approximately ±30 degrees for the nadir looking horn and 15-65 degrees for the side looking horn. The maneuver will yield a range of brightness temperatures from approximately 50 K to 100 K for the H-polarization, and approximately 100 K to 200 K for the V-polarization. Plotting the measured response as a function of the true incidence angle, and comparing the data to model data, e.g. using the widely accepted Klein-Swift model for the brightness temperature of the sea surface, a strong validation tool is present.

For the actual campaign, no lake was present, but after installation at Novo, a test flight was carried out, overflying the Southern Ocean off the ice shelf. During the flight, wing wags were performed as described, but no in-situ data is available. Meteorological data provide information on large scale wind speed (but the local wind scenario can only be guessed), and photographs taken by the aircraft crew indicate a low percentage ice cover (but a clean water surface cannot be guaranteed). Using the Klein-Swift model, and adding the expected contribution from the wind speed, model brightness temperatures are calculated. The result is seen in figure 3.6.1, named “KS-“. The measured brightness temperatures are seen in the same figure, and it is obvious, that the curves have a shape close to the model, while the level for all four channels is offset by several K. The actual average offsets are calculated and presented in column 2 of Table 3.6.1. The reason for the offsets is not known, and validation of the calibration procedure, using the cold sky as described above, does not indicate instrument or processing problems.

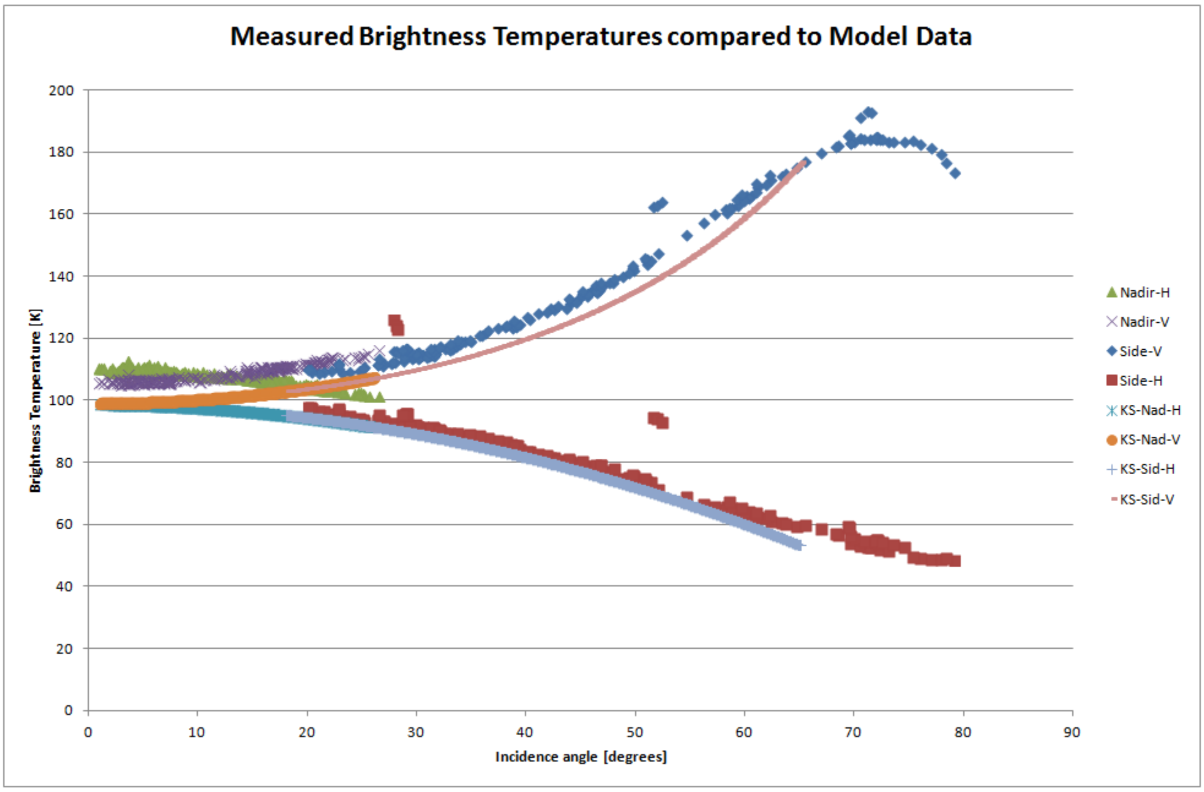


Figure 3.6.1: Model data and measured data for wing wags over the ocean.

One assumption could be, that the actual mechanical installation of the antennas – especially the nadir antenna, which is mounted with a plate around and close to the aperture, and furthermore the aperture is slightly retracted relative to the aircraft skin – could be a reason, causing increase in $S_{22}$ for all ports of the antenna system. Application of this theory yields the necessary $S_{22}$-values, which would eventually make all curves fit the model data, and these values are presented in column 3 of Table 3.6.1. Values should be compared to values in column 3 in Table 3.4.1, and it is seen, that a dramatic change is required. After the campaign, measurements were made on a VNA to investigate the effect of the mounting plate on the nadir horn, but very little effect was seen. Hence it is not fair to accept this parameter change, and the found required values for $S_{22}$ are not applied.

| Channel | Offset | $S_{22}$ required to fit model |
|---|---|---|
| Horn A, H-Pol | 11.10 K | -12.4 dB |
| Horn A, V-Pol | 7.50 K | -14.6 dB |
| Horn B, H-Pol | 3.29 K | -16.3 dB |
| Horn B, V-Pol | 5.32 K | -15.6 dB |

*Table 3.6.1: Offsets found from wing wags, and necessary $S_{22}$ parameters to explain data values.*

As the cause for the offsets is not known, it is difficult to access, whether the effect tends to be multiplicative (loss) or additive (reflection). Figures 3.6.2 and 3.6.3 show adjusted sets of curves for the multiplicative and the additive situation, respectively. The curves and their average deviation over the range up to 60 degrees incidence angle indicate a slightly better agreement with the additive effect, and as no explanation is available, the theory is accepted. However, offsets found from the ocean flight are NOT applied directly to the data due to the doubtful calibration measurement conditions: no in-situ wind data, not guaranteed ice free conditions.

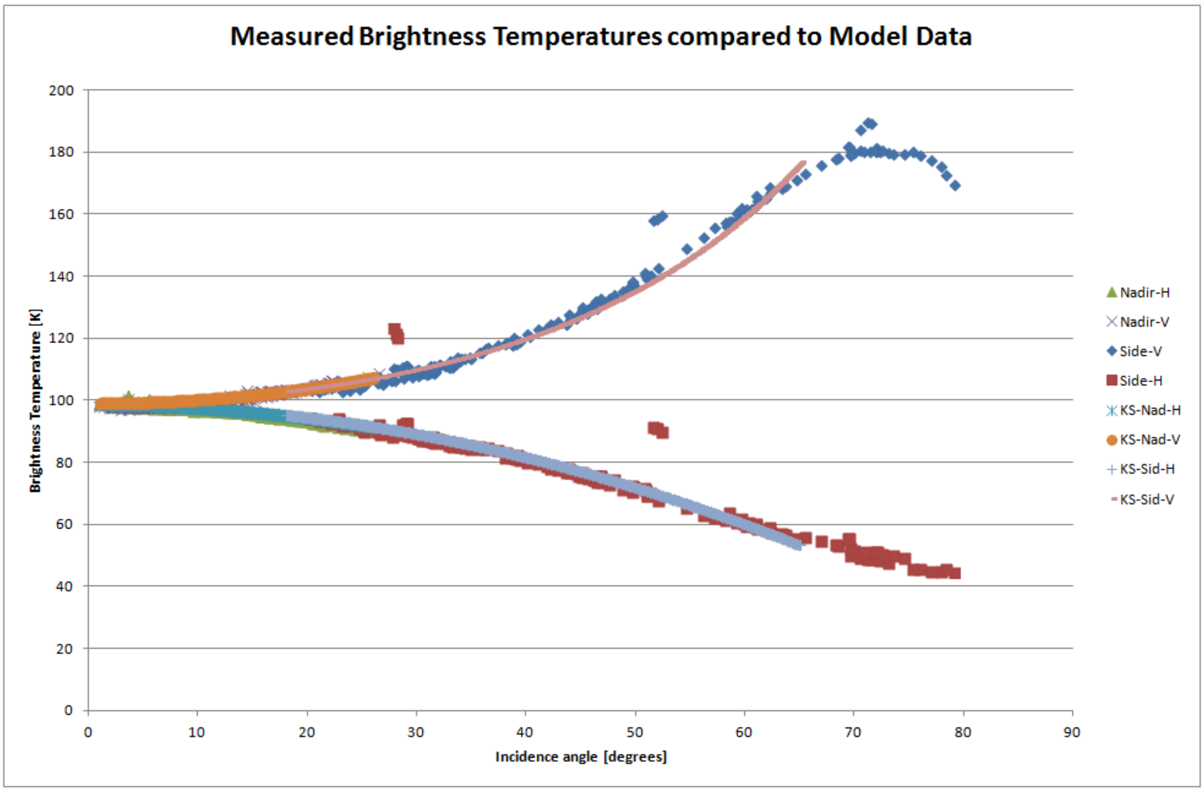


Figure 3.6.2: Model data and measured data for wing wags over the ocean. Data corrected for multiplicative error

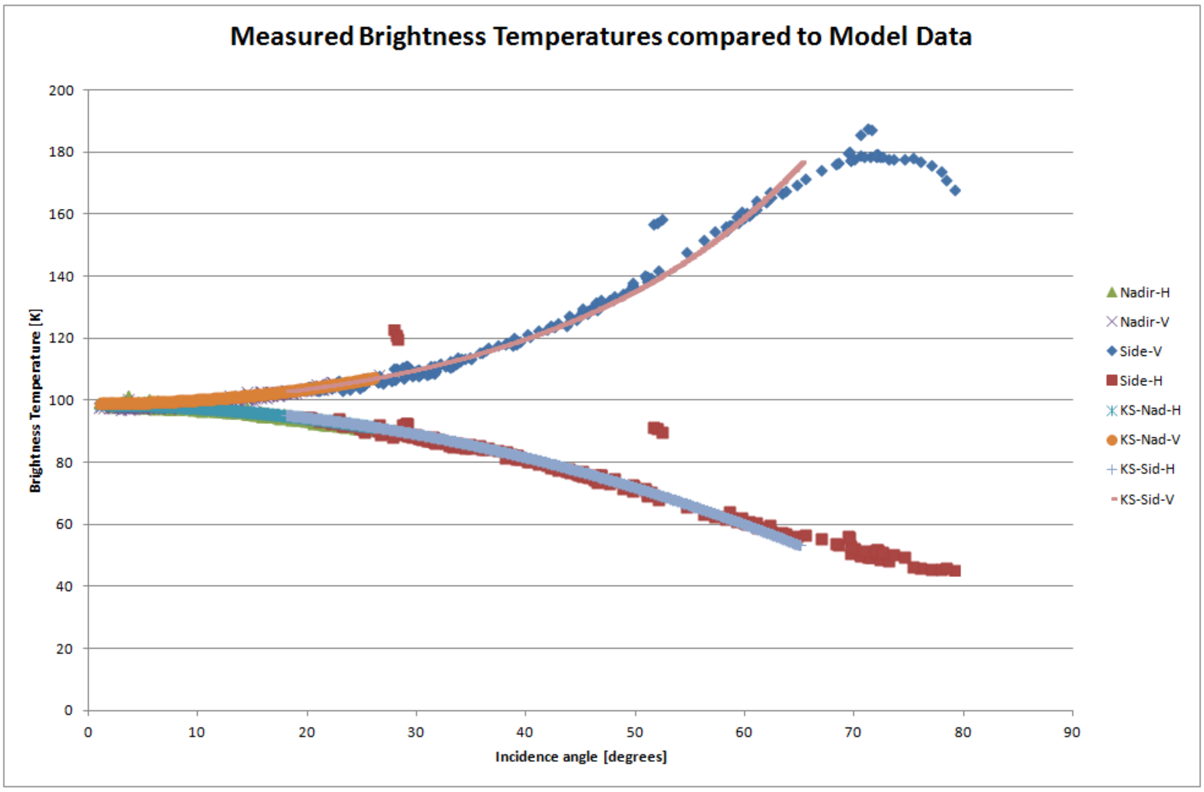


Figure 3.6.3: Model data and measured data for wing wags over the ocean. Data corrected for additive error.

Due to the above mentioned offsets, it is decided to use the sets of wing wags, performed over the target area ice to improve the estimates of a possible additive offset. A total of five sets were measured, however only three are considered. One of the discarded sets is measured in an area with large brightness temperature gradients, and the other has the antenna pointing partially towards the Sun. One of the data sets to be used is seen in Figure 3.6.4 along with fourth order polynomials to fit the curves.

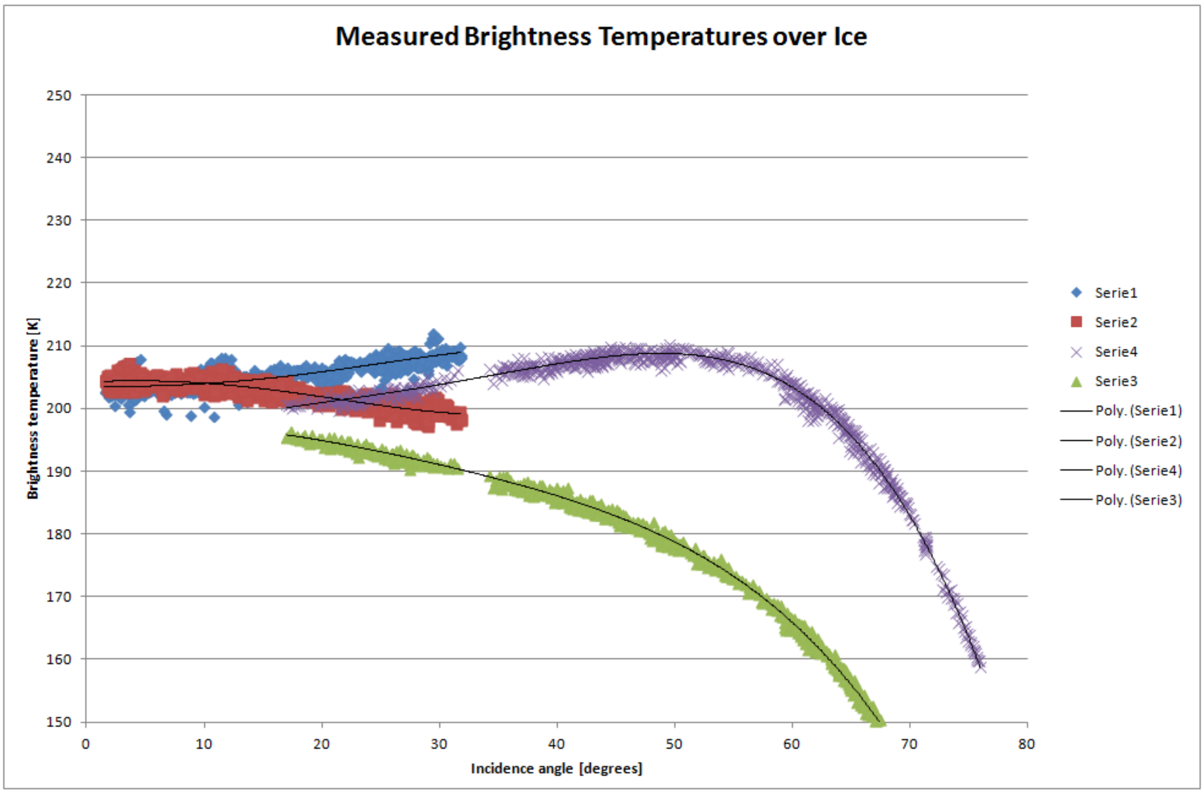


Figure 3.6.4: Measured data for wing wags over the target area. 4th order polynomial estimated for each curve section.

The offsets are obvious again, however for this target area there is no knowledge about the expected absolute level. Hence an absolute calibration cannot be made, but the curves can be adjusted to overlap correctly between the horns and to converge for the two channels at nadir. These criteria yield three offset values and leaves one degree of freedom. As the side looking horn(horn B), H-polarization channel had the lowest offset over the ocean, it is chosen as the reference channel, having a zero offset. Applying the same offset estimation to the other two data sets gives very consistent results, and average values are seen in Table 3.6.2.

| Channel | Offset |
|---|---|
| Horn A, H-Pol | 7.13 K |
| Horn A, V-Pol | 5.80 K |
| Horn B, H-Pol | 0.00 K (reference) |
| Horn B, V-Pol | 1.27 K |

*Table 3.6.2: Offsets found from wing wags over ice.*

Apart from the absolute level, relative offset are in very good consistence with the offsets in table 3 column 2, found over the ocean, and for the processing of the campaign data, it is chosen to apply the three relative offsets from Table 3.6.2 to the whole data set. After this correction, the wing wag, presented in Figure 3.6.4, appears as shown in Figure 3.6.5. It is not satisfactory, that the reason for the offsets could not be identified, but it is important to note, that offsets are very consistent, and that they do not influence on the relative accuracy of the data for each individual channel. The largest concern is the absolute level, which cannot be determined to the level of 1 K, which has been the target for earlier campaigns. In short: the lack of a well trusted, external calibration target near the campaign area – as was used on all previous SMOS related missions – makes absolute calibration difficult.

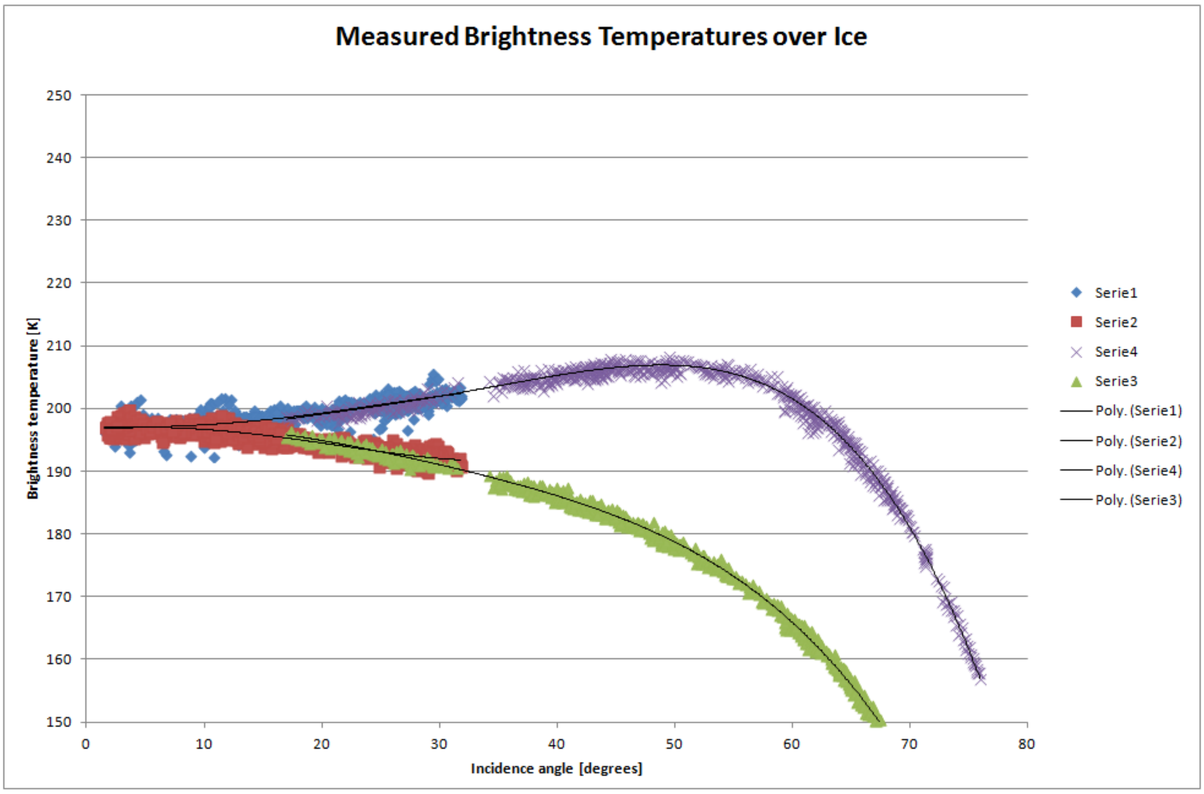


Figure 3.6.5: Measured data for wing wags over the target area. Data corrected for additive error. 4$^{th}$ order polynomial estimated for each curve section.

### 3.7 Additional data corrections, reference rotation and incidence angle

Knowing the actual rotation of the aircraft reference frame with respect to the Earth reference frame, Θ, the influence on the measured data can be calculated. Using the definitions of the true Stokes parameters, $I=T_V+T_H$, and $Q=T_V-T_H$, the actually measured parameters, $T_B$', are given by equation 4. Inversion of the matrix can be used to remove the effect, and this correction has been applied to all data from the campaign. Hence the final data set can be considered free from this rotation effect.

$$\overline{T_B}'=\begin{bmatrix} I' \\ Q' \\ U' \\ V' \end{bmatrix}=\begin{bmatrix} I \\ Q*\cos(2\theta)+U\sin(2\theta) \\ -Q*\sin(2\theta)+U\cos(2\theta) \\ V \end{bmatrix}=\begin{bmatrix} 1 & 0 & 0 & 0 \\ 0 & \cos(2\theta) & \sin(2\theta) & 0 \\ 0 & -\sin(2\theta) & \cos(2\theta) & 0 \\ 0 & 0 & 0 & 1 \end{bmatrix}\begin{bmatrix} I \\ Q \\ U \\ V \end{bmatrix} \tag{4}$$

For scientific evaluation of data, variations of the actual incidence angle over the target area, caused by natural roll and pitch variations, may be a significant noise source, and a potential error source in the case, where whole tracks are influenced by specific wind conditions. However, using the wing wag data, discussed above, it is possible to make a good rejection of this effect. As shown in Figure 3.6.5, each curve section has been fitted to a fourth order polynomial, and using these fits as a forward model, it is possible to calculate the expected $\Delta T_B$, caused by the incidence angle deviation from the desired incidence angle. Let $p_{BH}(\alpha)$ represent the model polynomial for the H-polarization of the side looking horn, and let 45 degrees be the nominal incidence angle for zero pitch and roll. The expected error signal, $\Delta T_B$, for the actual incidence angle, $\alpha_0$, is then found as $\Delta T_B = p_{BH}(\alpha) - p_{BH}(45 \text{ degrees})$, and the contribution can be subtracted from the actual measured data value. This correction method has been applied to all data from the campaign, and the final data set is delivered both corrected and uncorrected.

## 3.8 RFI Analysis and Mitigation

In the data set, analyzed in this report and delivered to the end users, data have been integrated to 1 s. Prior to temporal integration, the data set has been screened for RFI by evaluating kurtosis, polarimetric, and brightness temperatures anomalies as summarized in the steps listed below:

- Kurtosis ratios have been estimated for all data samples acquired when observing the antennas of the EMIRAD 2 system. These have subsequently been compared to the kurtosis ratios derived from the data samples recorded during observations of the internal calibration loads of the system – the latter set of data samples is known to be free from RFI. All antenna-related data samples exhibiting kurtosis ratios deviating more than ± 4 standard deviations from the mean of the clean kurtosis ratios have been flagged as RFI contaminated.

- Elevated values of the 3rd and 4th Stokes parameters have been shown to be a powerful indicator of RFI, hence all data samples with 3rd or 4th Stokes parameters greater than ±10 K have been marked as contaminated by RFI as well. The threshold of ±10K has been established during analyses of data from previous EMIRAD 2 campaigns as providing a reasonable level of RFI detection capability whilst keeping the number of false alarms at a minimum.
- Finally, all occurrences of unnaturally elevated brightness temperatures have been marked as affected by RFI. In the present data set, all brightness temperatures above 320 K have been characterized as unnaturally elevated.

All data samples flagged by any combination of the three steps above have been removed from the data set. This, however, does not guarantee that *all* data samples still contained within the cleaned data set are indeed free from RFI: special cases might go un-noticed by the detection methods used.

In addition to anomalies related to RFI, the horizontal channel of the side-looking antenna has been observed to exhibit elevated brightness temperatures from time to time. This is due to a mechanical problem with one of the microwave switches of the radiometer system. These elevated levels are easily detectable, and have been removed from the data set. While being unrelated to RFI, this has for practical reasons been carried out in conjunction with the RFI screening procedure.

Global statistics shows that some 3.7% of the data from the nadir horn was flagged and about 1.4 % from the side looking horn. When subtracting the mean value of the cleaned data from the mean value of the full, not-cleaned data, the following is noticed:

- Very little difference for the side looking horn. Although RFI is detected, it generally is of quite low intensity.
- For the nadir horn, the situation is more diverse: in many data files the difference is again very small, but is a few cases it is significant. As an example, in the first file from the first day (17'th of January), 3.8 % of the data are flagged, the mean of the full data set is 207.6 K while the mean of the cleaned data set is 205.0 K – i.e. a difference, hence contribution from RFI, of 2.6 K.

In short: there is indeed RFI of significance in Antarctica, but it can be mitigated, and the loss of data does not influence final data quality (radiometric sensitivity).

After the RFI detection and mitigation described above was done, visual inspection of data showed that some samples were affected by low level RFI. These samples were removed using median filtering.

### 3.9 Wag Data on DOMEX-3 Data

The wing wag data as discussed in the previous section are well suited for comparison with DOMEX-3 data as functions of incidence angle. Figure 3.9.1 shows data provided by Giovanni with the DOMECair data plotted on the same figure. However, before doing that some considerations are necessary. From the 2D imagery shown in Chapter 5 it is obvious that there is a significant difference in the brightness temperature level in the wing wag area compared with the Concordia area. Close inspection of the data behind the 2D images reveals a 2.5 K difference. Gridline 5 passes through Concordia, and also close to the wing wag area. Inspection of the line 5 profile indicates a 2 K difference. Finally, comparing 40° DOMEX data with line 5 side looking data near Concordia confirms the 2 K bias. However, a conclusion pointing to a 2 K bias must be made with utmost caution: due to the non-homogeneous brightness temperature scene – as will be discussed in the following chapters – it must be realized that the low resolution 2D image tends to smear brightness temperature differences, and the high resolution profile shows a rapid brightness temperature fluctuation, such that the comparison of point measurements are very difficult.

However, the decision has been taken to add 2K to the DOMECair data before plotting them on the DOMEX data in Figure 3.9.1.

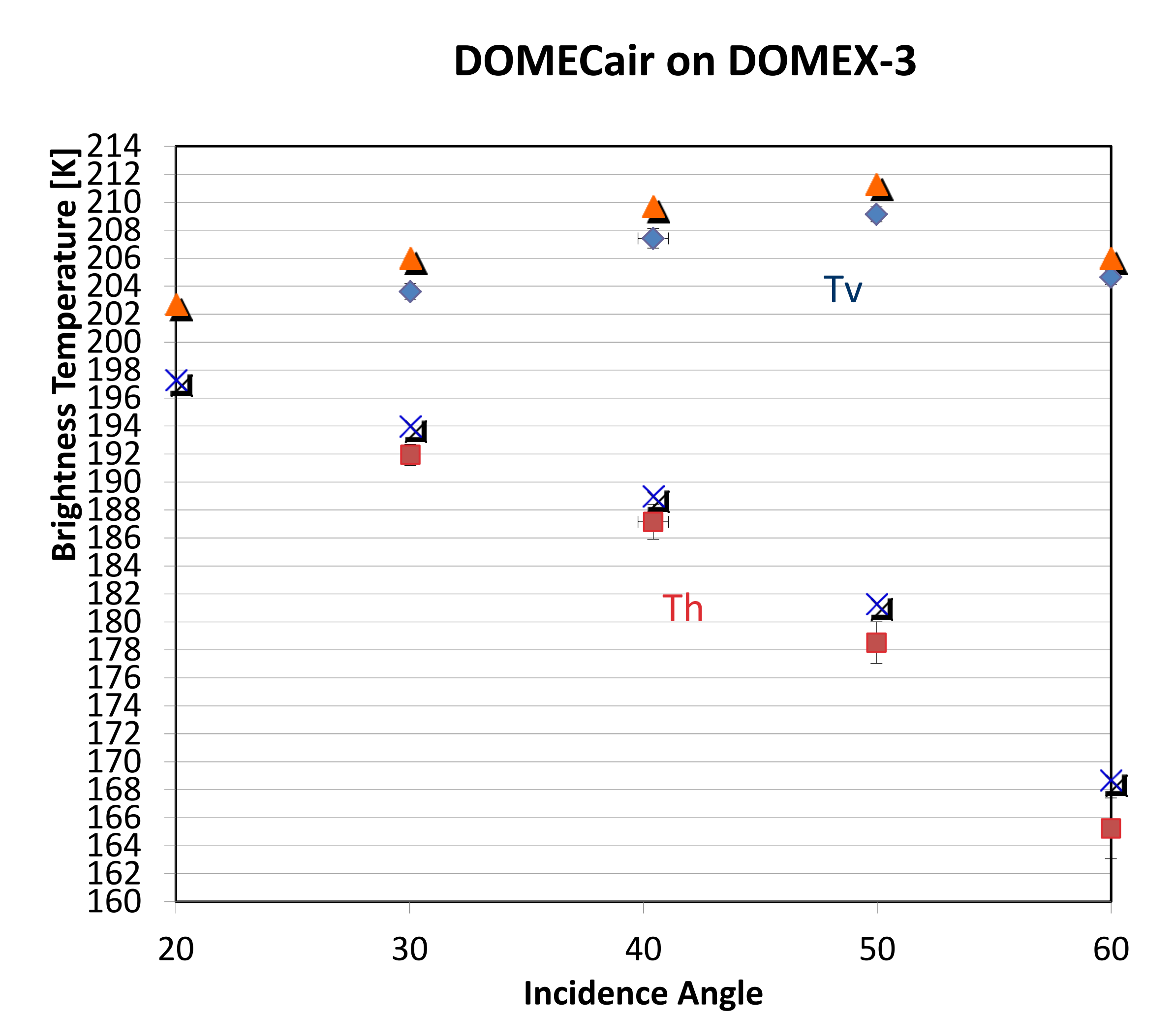


Figure 3.9.1: Brightness temperature as functions of incidence angle (diamond and square: DOMEX, triangle and cross: DOMECair)

It is seen that the 2 sets of curves in general tracks nicely – but with a 2K bias. One might be tempted to conclude that the 2 K should not have been added to the DTU data, resulting in an almost perfect match! But inspection of the data as discussed above does not seem to justify such a conclusion.

However, the comparison is quite satisfactory: we are comparing data from two different instruments each having their individual absolute calibration challenges. It is especially difficult to establish the absolute calibration of the EMIRAD instrument during the campaign, as a sky view is not possible, and also regularly passing a lake with known temperature and wind conditions (as is routinely done in soil moisture campaigns) is also not possible.

## 3.10 Circle Flights

For certain scientific needs it is desired to observe a single foot print from many different directions and incidence angles, and for this purpose circle flight patterns were performed twice during the campaign. Performing a circle flight pattern allows observation from all points on a circle, covering the full 360 degrees range, and through variation of attitude, various incidence angles may be covered. The purpose of the actual circle flights in this campaign is primarily to understand the influence on the measured brightness temperature from the Sun, which is a strong point target, and it shall be evaluated, for which angles relative to the Sun the contribution can be neglected in the interpretation of the scientific survey flights. Furthermore it shall be investigated, if the Galactic background radiation influences on the measurements, and if non-downwelling dependent azimuth signatures, i.e. systematic direction dependent variations in the target emission, are present.

During the circle flight planning some compromises must be made. Important to the measurement is a stable attitude, and typically this is not possible on a perfect circle track in the presence of wind, as the aircraft will compensate the wind force through small attitude adjustments. Without attitude variation, the circle center will drift slowly along a line, determined by the wind vector. Assuming a homogeneous target surface, the drift will not be a problem, as the foot print shift will not cause a systematic error, and for the Antarctic campaign, this choice was made. The actual aircraft antenna horn installation allows two incidence angles to be measured at the same time: nadir and 45 degrees for zero roll and pitch. With a typical roll of 10 degrees for a fair circle radius, incidence angles of 10 degrees and 35 degrees will be covered for positive roll (clockwise circles), while 10 degrees and 55 degrees will be covered for negative roll (counterclockwise circles). The side looking horn at negative roll as well as the nadir looking horn for both positive and negative roll will not be able to cover a fixed foot print, as the foot print ground track will always draw a circle outside the aircraft ground track (assuming the aircraft acceleration vector will always point to the side of the roll, which is practically the case for any aircraft). Still assuming a homogeneous target, this is not considered a problem.

The influence from the Sun is an important scientific objective, but at the same time the Sun is so strong, that it might mask out other effects. Ideally two different types of circle flight patterns should be carried out: with the Sun above the horizon, and with the Sun below the horizon. Unfortunately this is not possible during the campaign, as the Sun at latitude 75 South is always above the horizon during the duration of the campaign. Instead two flights are made at different times of day; one AM with the Sun approximately at +25 degrees relative to Earth North (i.e. North-East) and at an elevation angle of 34 degrees (incidence angle equal to 56 degrees), and one PM with the sun at -100 degrees (i.e. West) and at an elevation angle of 19 degrees (incidence angle equal to 71 degrees).

The Galactic background radiation is found from the Sky map, shown in the left panes of Figure 3.10.1.The radiation consists of two components, the line emission (top pane) and the continuum radiation (bottom pane), and the total down welling radiation is found as the sum of the two contributions. For any practical antenna, the radiation pattern will cover a relatively wide angular space in the Sky map, and hence the map should be convoluted by the antenna pattern to get the actual contribution, seen by the radiometer. This is done for the large, side looking antenna (horn B) in the two right panes. The actual co-ordinate in the Sky map is a function of the position (latitude, longitude), the look direction, the incidence angle, the reflection mechanism at the ice surface, and the time of day. Assuming a simple flat surface reflection described by geometrical optics, the co-ordinate can be directly derived from the actual navigation parameters and the time of day. Unfortunately the look direction to the Galactic center will change during the day, almost following the change of the direction to the Sun, as both primarily depend on the Earth rotation. The Galactic background will shift approximately 1 degree per day due to the Earth motion around the Sun, but this change is too small during the campaign, and hence the possibility of separating the effect of the two sources is reduced.

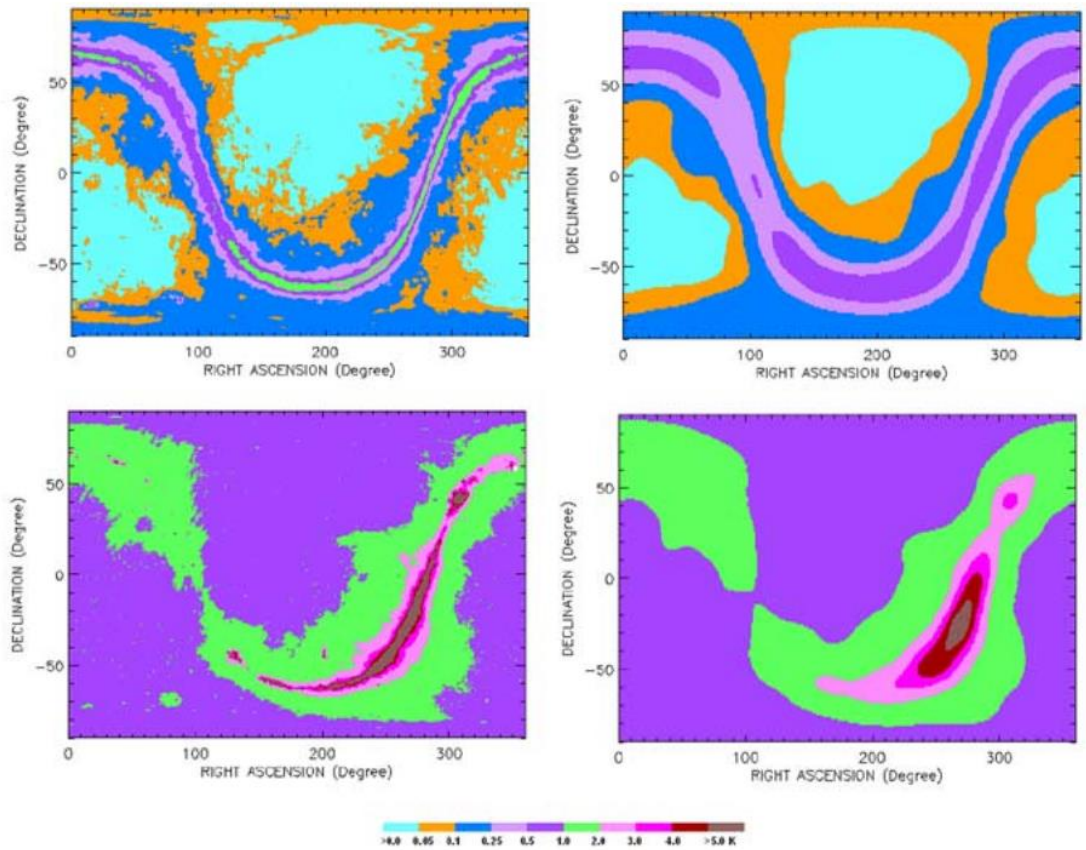


Figure 3.10.1: Map of the Galactic background. Top panes show the hydrogen emission line at 1.42 GHz and bottom panes show continuum emission. Left column shows the original high resolution map, and the right column shows the map after convolution with the antenna radiation pattern for horn B.

Data from the circle flights are calibrated using the standard calibration, described earlier in this report. The only processing difference, compared to other scientific flights is, that post-integration is not done to a fixed time interval (1 s for other data). But instead samples are integrated within angular bins. One bin covers 2 degrees of look direction, and hence the first bin covers all observations made in directions from 0 degrees to 2 degrees relative to Earth North, the next from 2 degrees to 4 degrees etc. The bin width of 2 degrees has been chosen to obtain a temporal integration close to 1 s, which gives a sensitivity, $\Delta T_{circle}$, close to the $\Delta T_{survey}$, valid for the other scientific flight tracks. To further reduce random noise and to evaluate each incidence angle as one observation, samples within each angular bin are averaged to yield one sample. Hence a complete azimuth signature for one specific incidence angle consists of 180 data points. Another important difference from the processing of the survey flight data is, that the correction for small attitude driven incidence angle variations during the flight has been normalized to 10 degrees for horn A (usually nadir) and to

35 degrees and 55 degrees for horn B (usually 45 degrees) for the clockwise and counterclockwise circles, respectively. Be aware, however, that the correction only removes the ice radiation, and hence it does not correct for antenna gain variations in direction of the Sun, when the incidence angle changes!

Covering three different incidence angles for two flights yields a total of 6 azimuth signatures. Each signature is presented as traditional $T_V$ and $T_H$ observations, but also the four true Stokes parameters, (I, Q, U, V), are shown, i.e. six signatures for each incidence angle. Figures 3.10.2-3.10.19 (placed at the end of this paragraph) show all the results, and each incidence angle is presented in three panes, covering ($T_V$,$T_H$), (I,Q) , and (U,V), respectively. All figures show the look direction relative to Earth North on the horizontal axis and observed Brightness on the vertical axis. For each signature the azimuth direction of the Sun is shown through a vertical, yellow bar. Furthermore the downwelling Galactic background contribution is calculated using the skymap, and results for each azimuth signature are shown in the Figures 3.10.20-3.10.25 (placed at the end of this paragraph). The diffuse behavior of some data points, especially close to gradients, is caused by the small shift in time between subsequent circles. With a total of typical 10 circles per azimuth signature, data sampling takes around one hour, causing the Sky to shift approximately 15 degrees relative to Earth. For each azimuth signature in the Figures 3.10.2-3.10.19, the maximum of the galactic contribution is shown, using a vertical blue bar. For all signatures it is noticed, that the sample to sample variation is typically relatively small, in the order of 100 mK - 200 mK for most signatures (apart from a few outliers, most likely caused by RFI).

Considering first the signatures with incidence angle equal to 55 degrees, i.e. Figures 3.10.2-3.10.7, it is clearly seen, that there is a strong contribution around the sun position. The contribution is far larger in the horizontal polarization than in the vertical, which is as expected according to surface reflection coefficients at the surface (same mechanism, which causes the brightness temperature to be lower in the horizontal polarization than in the vertical). 6-8 K is observed in $T_H$, while $T_V$ response is less than 1 K for both cases. The width of the main Sun signature is approximately 80 degrees, which is very well in line with the 87 degree wide -25 dB beam width of the side looking antenna. The stronger response in $T_H$ for the AM flight is consistent with the higher elevation of the sun. While the Sun position (and hence also the reflected beam from the surface) equals an incidence angle equal to 56 degrees at AM, it has shifted to 71 degrees for the PM situation. This is 16 degrees off the antenna bore sight, and according to the antenna radiation pattern, the gain has dropped approximately 2 dB at this point. The AM situation must be considered a worst-case situation with the Sun almost at antenna bore sight. The behavior of both $T_V$ and $T_H$ in the angular area from 45 degrees to some 135 degrees for the AM signature is not as expected, being elevated up to 1 K. There is no instrumental explanation for this observation, and results might indicate a more complex reflection mechanism at the surface, scattering the Sun radiation to a wider angular area, or a possible underlying azimuth dependent emission. The same behavior is noticed for the PM flight, however on the left side of the Sun instead. None of the elevated angular ranges coincide with the Galactic center, according to Figure 3.10.20 and 3.10.21 (placed at the end of this paragraph).

The response of the 1st and 2nd Stokes parameters is as expected, with $Q=T_V-T_H$ having a minimum in the direction of the Sun. $I= T_V-T_H$ clearly emphasizes the elevated signature some 60-90 degrees off the Sun position. The response of the 3rd Stokes parameter, U, is mainly caused by the antenna artifacts, described in the calibration chapter. Observing with an incidence angle equal to 55 degrees causes an offset of ±2.5 K due to cross polarization. Likewise the strong negative gradient of the 3rd Stokes parameter around the direction to the Sun is caused by cross polar signals, having opposite sign on the two sides of antenna bore sight. These artifacts are clearly identified in both the AM and the PM signature. Apart from the artificial signatures, an underlying signature seems to be present. This signature seems to have a maximum around 180 degrees and a minimum close to 45 degrees. A similar response is seen in the 4th Stokes parameter, and it is clear, that the signature is not shifted from AM to PM, i.e. the signature is neither related to the Sun nor the Galactic background. The scientific origin of the signature cannot be identified from the actual data set, but there is a clear indication, that the target area may not be completely homogeneous.

The signatures, obtained at 35 degrees incidence angles, are seen in the Figures 3.10.8-3.10.13. $T_H$ and $T_V$ still show a significant contribution from the Sun, but reduced in magnitude compared to the 55 degree incidence angle situation. Again results are very well consistent with the antenna radiation pattern, as the Sun elevation results in a Sun positions within the pattern, which is slightly more than 20 degrees off bore sight for AM and about 35 off bore sight for PM. Comparing the PM situation to the worst case scenario (55 degrees, AM), the response should be reduced by 16 dB, according to the antenna pattern. This should yield a signature of approximately 200 mK at H-Pol and less than 50 mK at V-Pol. However, observed Sun signatures for the 35 degrees incidence angle are in the vicinity of 500 mK for both polarizations, which strongly indicate a surface reflection, which is more complex than simple flat surface geometrical optics. The signature still extends to approximately ±40 degrees relative to the Sun, and these two results are important to notice in the scientific interpretation of survey data. The unexplained elevation of the level close to the Sun signature in the angular interval from 45 degrees to 180 degrees – especially for $T_V$ AM – which was seen for 55 degrees incidence angle, seems to repeat in the 35 degrees measurements, and again the elevated curve section seems to appear to the left of the Sun for the PM case.

The 3rd and 4th Stokes parameters still show the antenna artifact signatures around the Sun position, but also with much smaller magnitude, due to the Sun position relative to antenna bore sight. Important is to notice the azimuth signature for both AM and PM, and comparing to the similar figures for 55 degrees incidence angles, the signatures are almost identical! Again the underlying signature do not follow neither the Sun nor the Galaxy, and a clear signature with one or two local maxima for the 3rd Stokes parameter and two local maxima for the 4th Stokes parameter are identified, both with magnitudes in the vicinity of 500 mK!

The last set of circle signatures cover the measurements at 10 degrees incidence angle, and they are found in the Figures 3.10.14-3.10.19. For $T_H$ and $T_V$ it still seems possible to identify the sun position for the AM case, but not in the PM case. It should be noticed, that this signature is obtained, using horn A instead of horn B, which means, that the antenna radiation pattern is slightly wider. For the AM case, the Sun is 46 degrees from bore sight, where the antenna gain should be about -18 dB. This should yield a Sun signature of about 100 mK, but the actual measured response is closer to 300 mK. Again this indicates a reflection mechanism at the ice surface, which is more complex than simple flat surface reflection, which causes the Sun radiation to be scattered to a slightly larger angular interval. For the PM case, having the Sun at 60 degrees off bore sight, there is no detectable signature, and this is very well in line with the antenna pattern being below -25 dB for all angles above 53 degrees. The important result here is, that although some scattering of the radiation occurs, it does not extend beyond 60 degrees off bore sight with a detectable magnitude. For the 3rd and 4th Stokes parameters no signature is present at 10 degrees incidence angle, neither for the AM or the PM case. There is no scientific explanation for the signature to be present at higher incidence angles, and zero for low incidence angles, but there are no instrumental or antenna issues to explain the behavior.

In conclusion to all circle signatures it is important to notice, that the Sun is far the most important concern! The Sun appears very clearly in all signatures, and a worst case of 8 K contribution is found, when looking directly to the reflected Sun at H-Pol. The magnitude decreases as expected close to antenna bore sight, but at larger angles from bore sight, the decrease rate is not quite as high as expected, which indicate some scattering of the radiation in the order of 200-300 mK close to the -20 dB limit of the antenna radiation pattern, where 80 mK would be expected. However, the scattering seems to affect only observations close to the -20 dB limit, and going extra 10 degrees off bore sight removes the contribution completely.

The Galactic background adds a downwelling contribution up to approximately 6 K at worst case. For the actual measurements – and especially those with high Galactic contribution - the Galactic center is located relative close to the Sun position, however, and in general no Galactic signature was identified in the present data set. Some azimuth signatures were identified; especially for the 3rd and 4th Stokes parameters at higher incidence angles. The signatures were obviously not connected to neither the Sun nor the Galaxy, and for the time being, there is no clear indication about their origin. The Figures 3.10.26-3.10.29 (placed at the end of this paragraph) show zoomed plots into the survey maps at the position of the two circle flights, illustrating the interpolated brightness temperature for each of the four channels (horn A and B, V-Pol and H-Pol), and overlaid by the actual flight tracks. All four plots obviously indicate, that the target area is not completely homogeneous throughout the area of interest, and it is not at all unlikely, that some features may be present at the surface or slightly below. Looking at the flight tracks, it should be remembered, that observations for 10 degrees and 35 degrees incidence angle are taken at the outside of the ground track circle of the aircraft. This makes samples from the signatures originate from geographical positions, which are located several kilometers from each other.

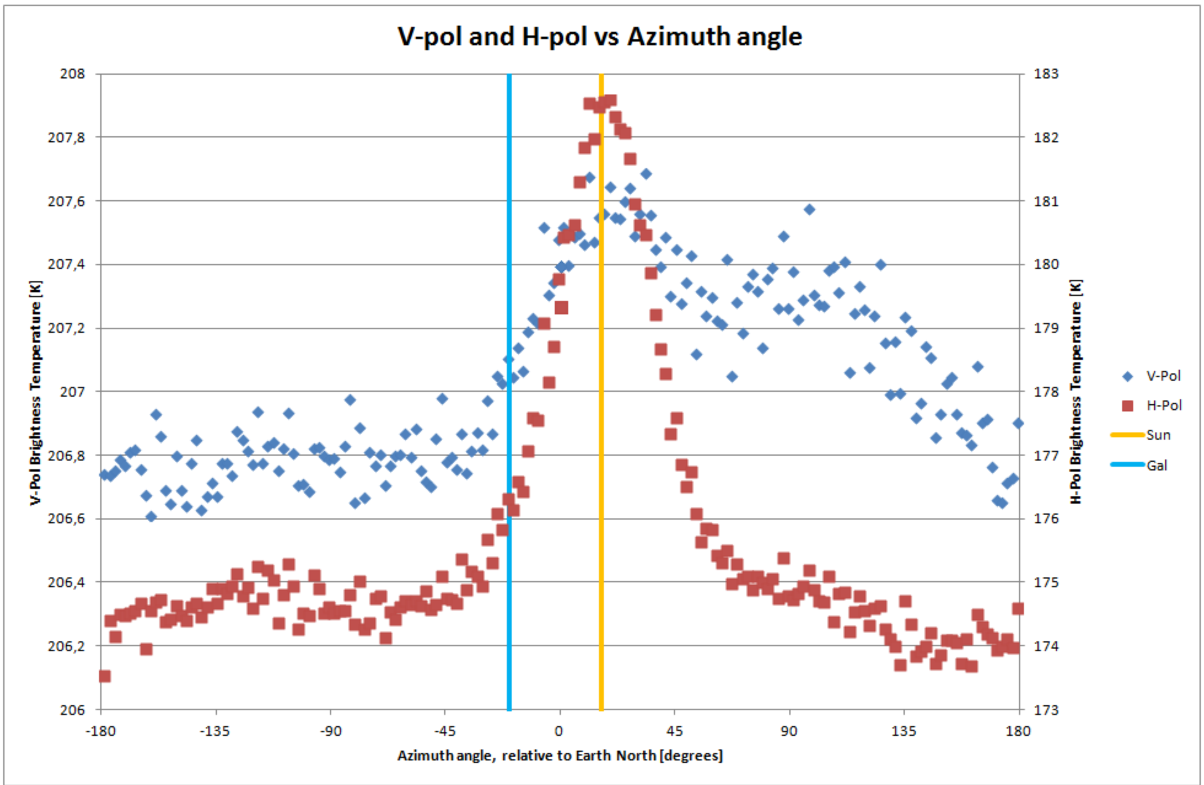


Figure 3.10.2: Azimuth signature for AM circle flight at 55 degrees incidence angle. $T_V$ and $T_H$ as a function of look direction relative to Earth North.

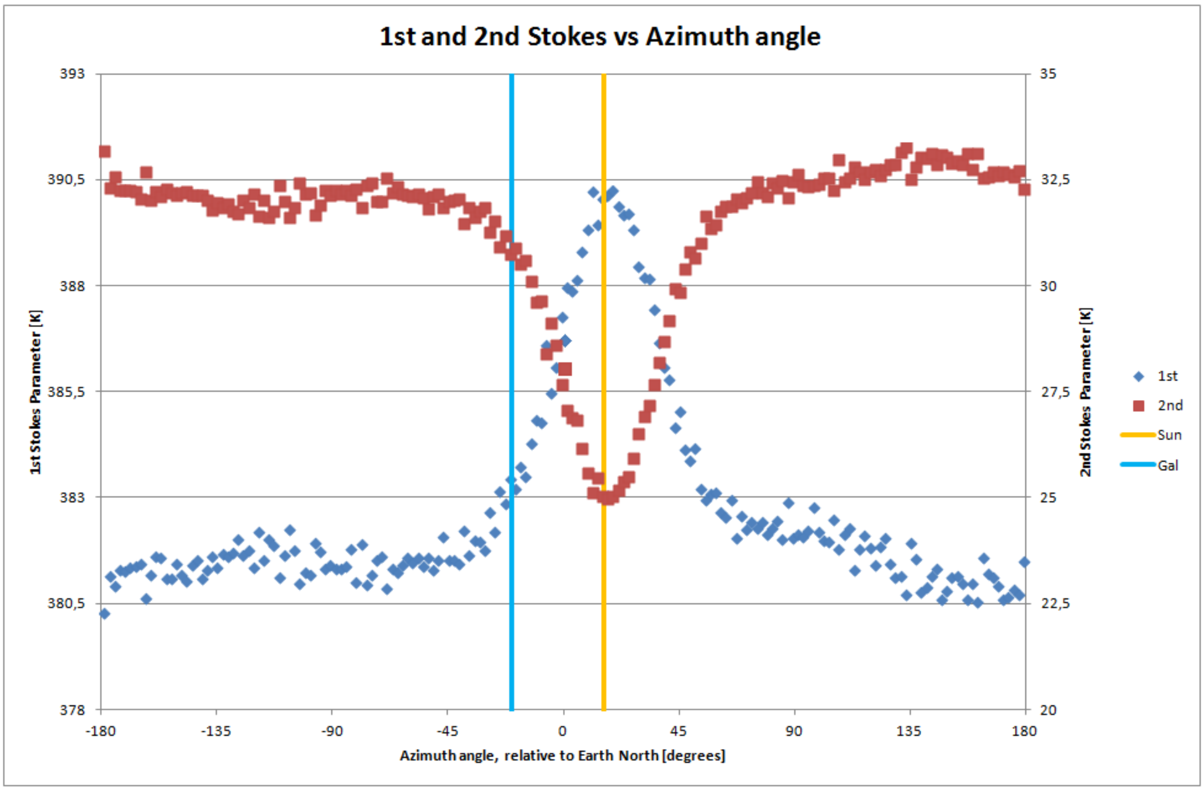


Figure 3.10.3: Azimuth signature for AM circle flight at 55 degrees incidence angle. 1st and 2nd true Stokes parameters as a function of look direction relative to Earth North.

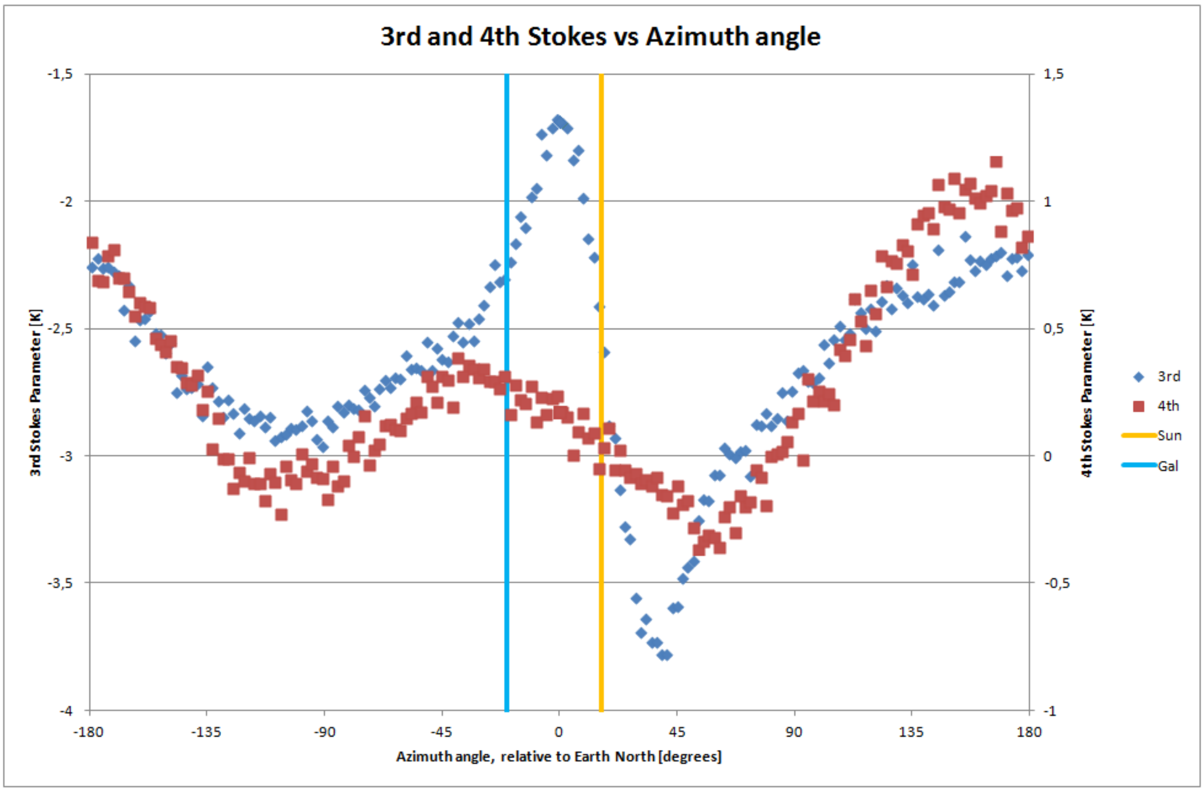


Figure 3.10.4: Azimuth signature for AM circle flight at 55 degrees incidence angle. 3rd and 4th Stokes parameters as a function of look direction relative to Earth North.

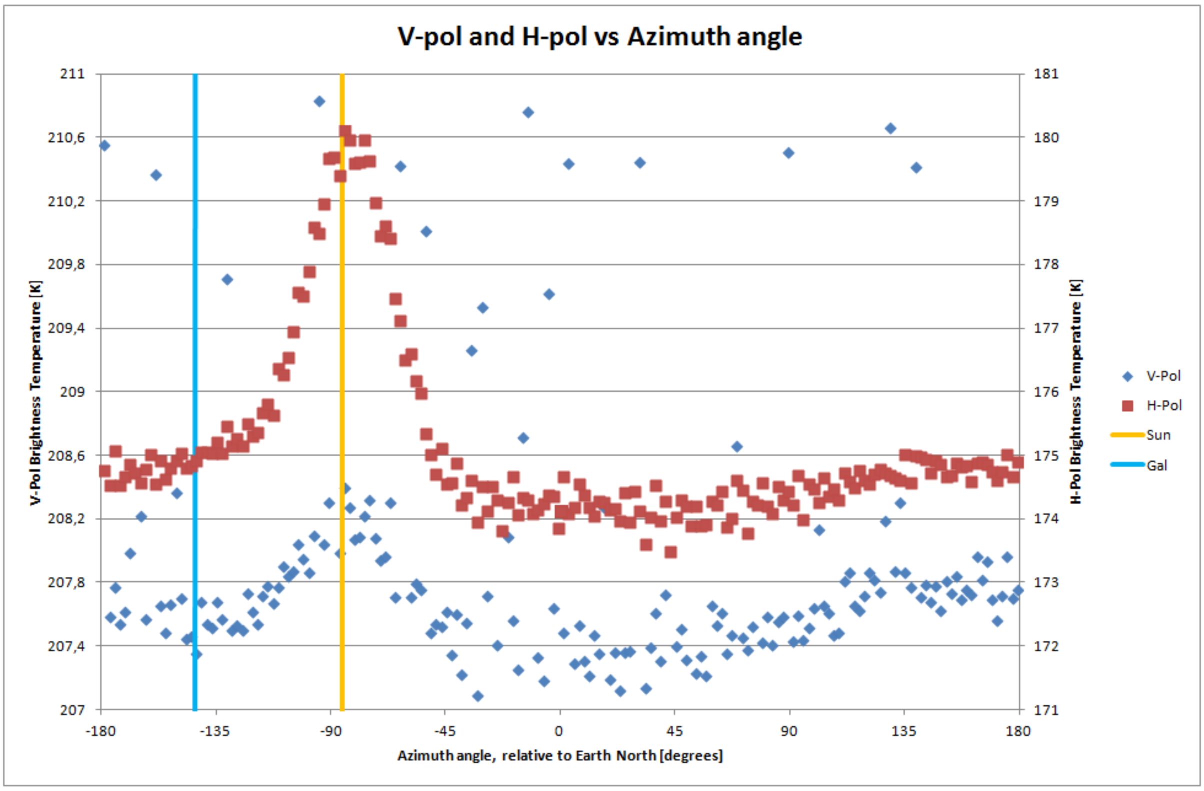


Figure 3.10.5: Azimuth signature for PM circle flight at 55 degrees incidence angle. $T_V$ and $T_H$ as a function of look direction relative to Earth North.

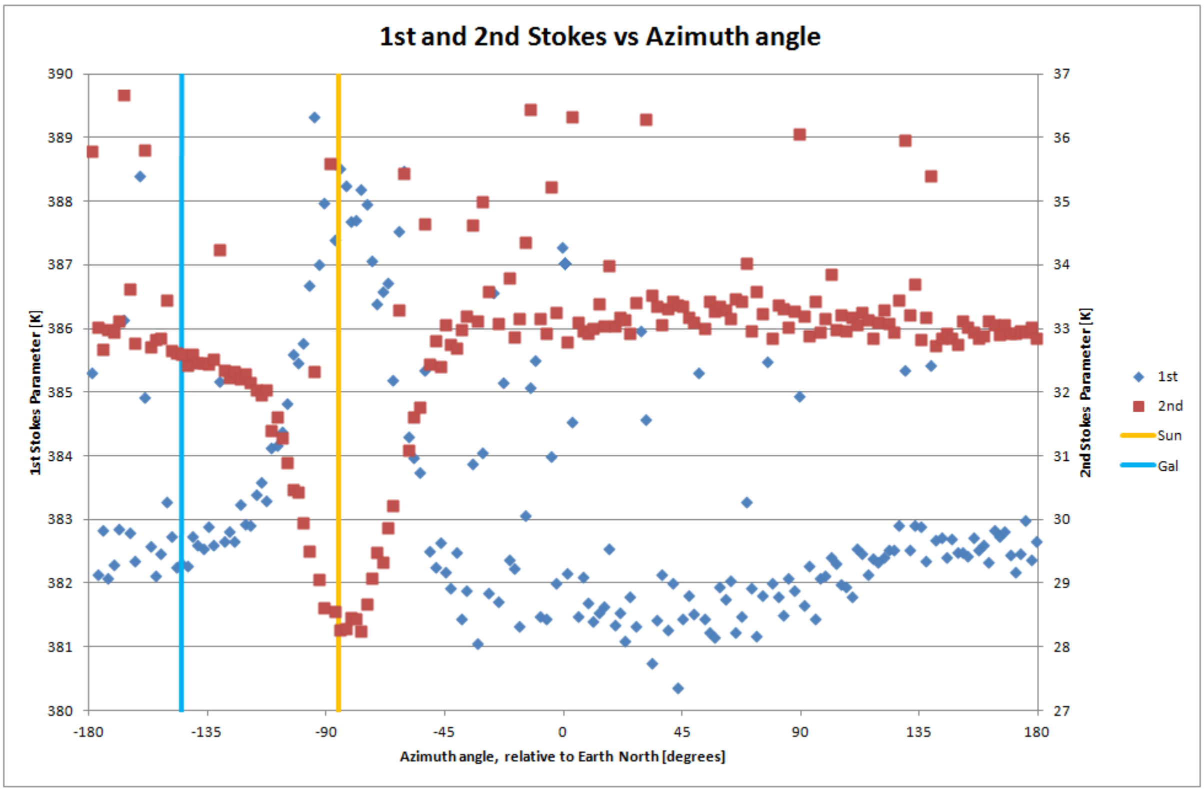


Figure 3.10.6: Azimuth signature for PM circle flight at 55 degrees incidence angle. 1st and 2nd true Stokes parameters as a function of look direction relative to Earth North.

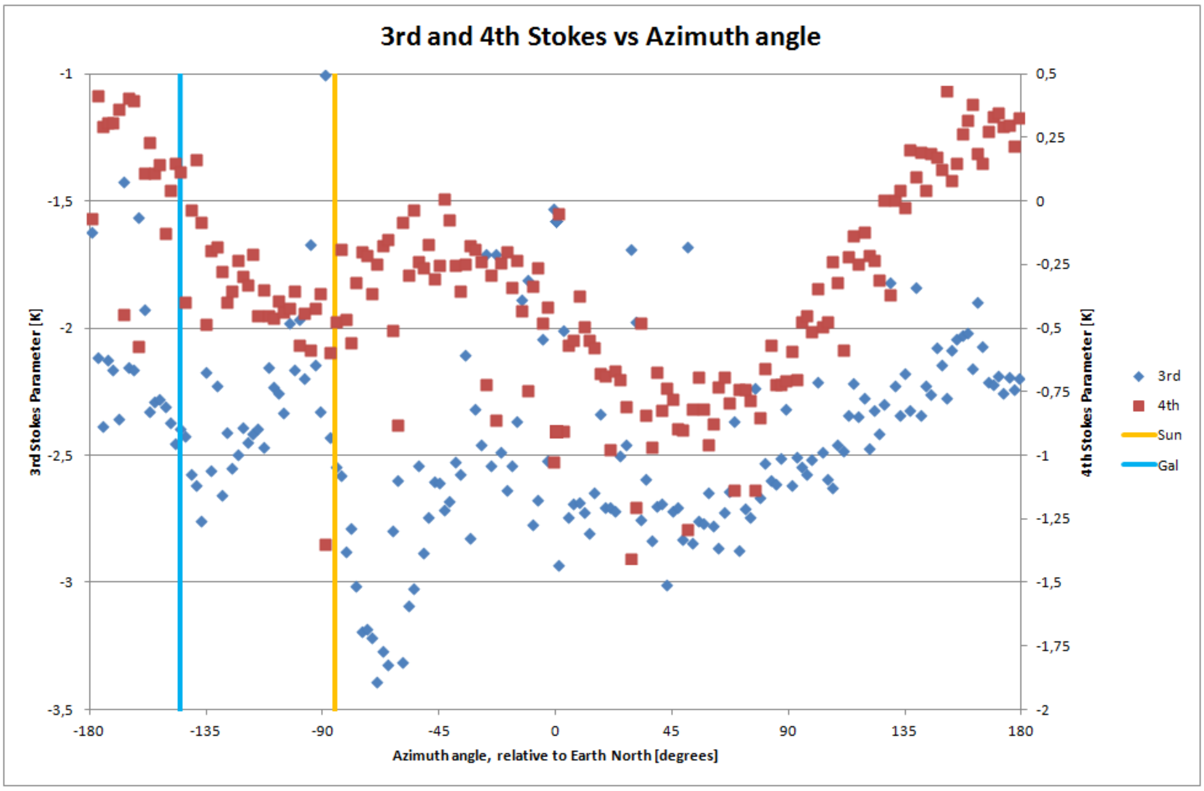


Figure 3.10.7: Azimuth signature for PM circle flight at 55 degrees incidence angle. 3rd and 4th Stokes parameters as a function of look direction relative to Earth North.

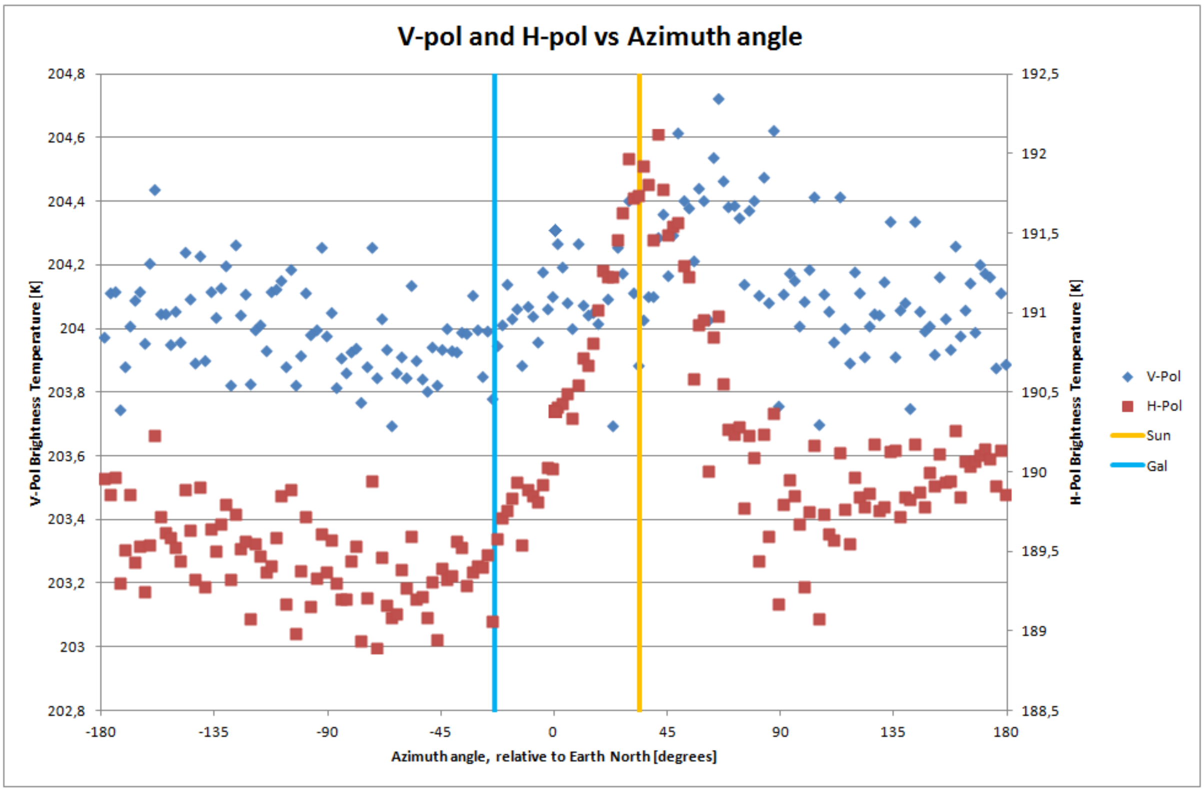


Figure 3.10.8: Azimuth signature for AM circle flight at 35 degrees incidence angle. $T_V$ and $T_H$ as a function of look direction relative to Earth North.

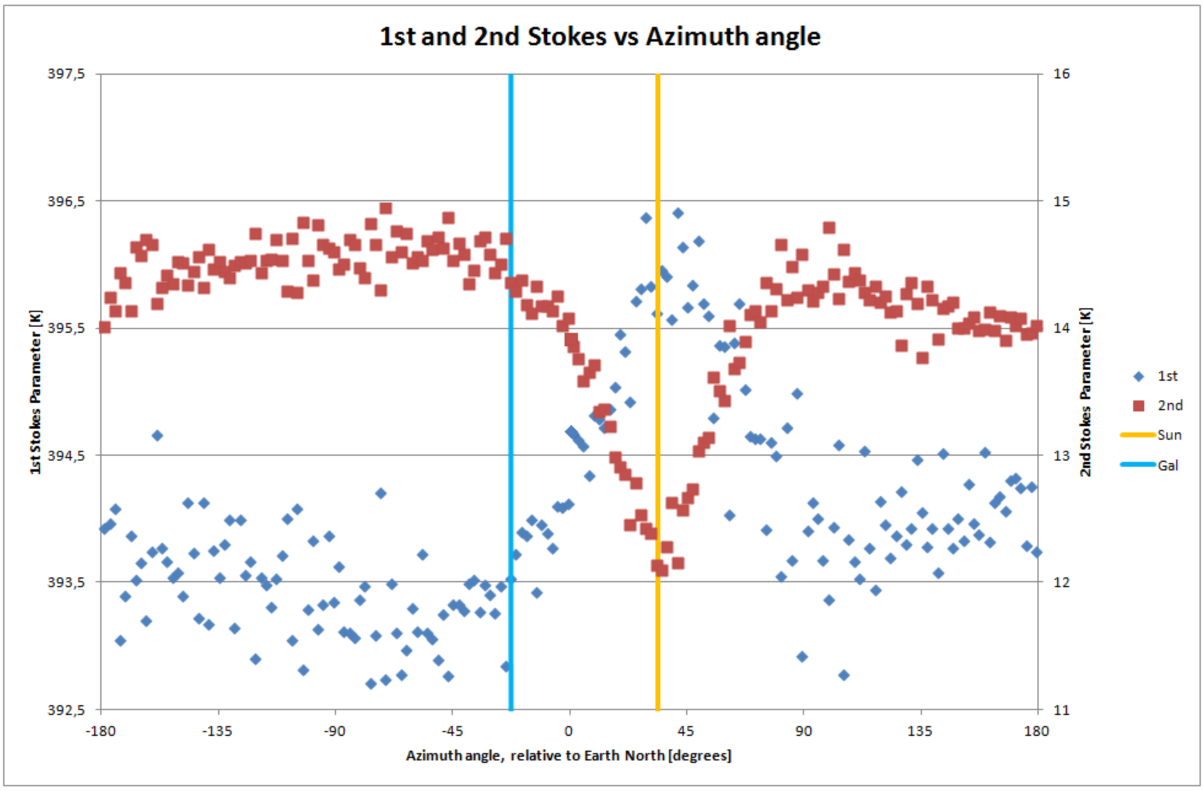


Figure 3.10.9: Azimuth signature for AM circle flight at 35 degrees incidence angle. 1st and 2nd true Stokes parameters as a function of look direction relative to Earth North.

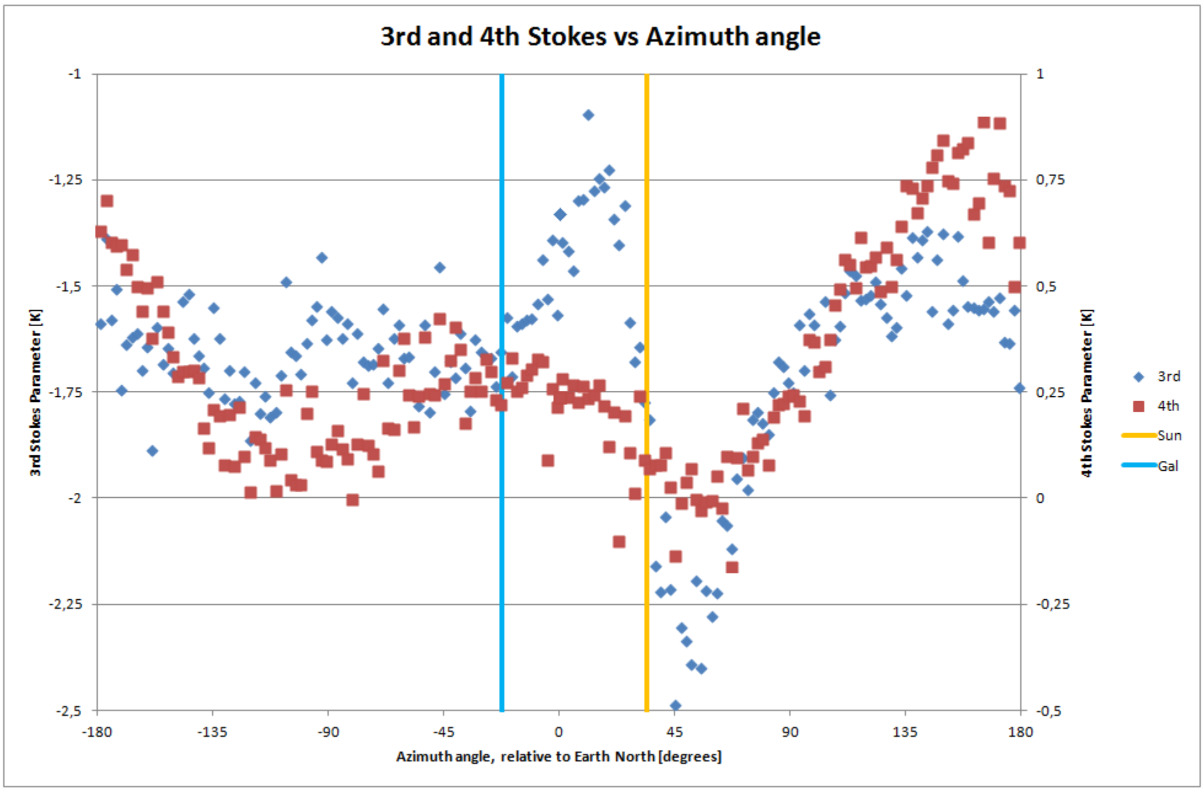


Figure 3.10.10: Azimuth signature for AM circle flight at 35 degrees incidence angle. 3rd and 4th Stokes parameters as a function of look direction relative to Earth North.

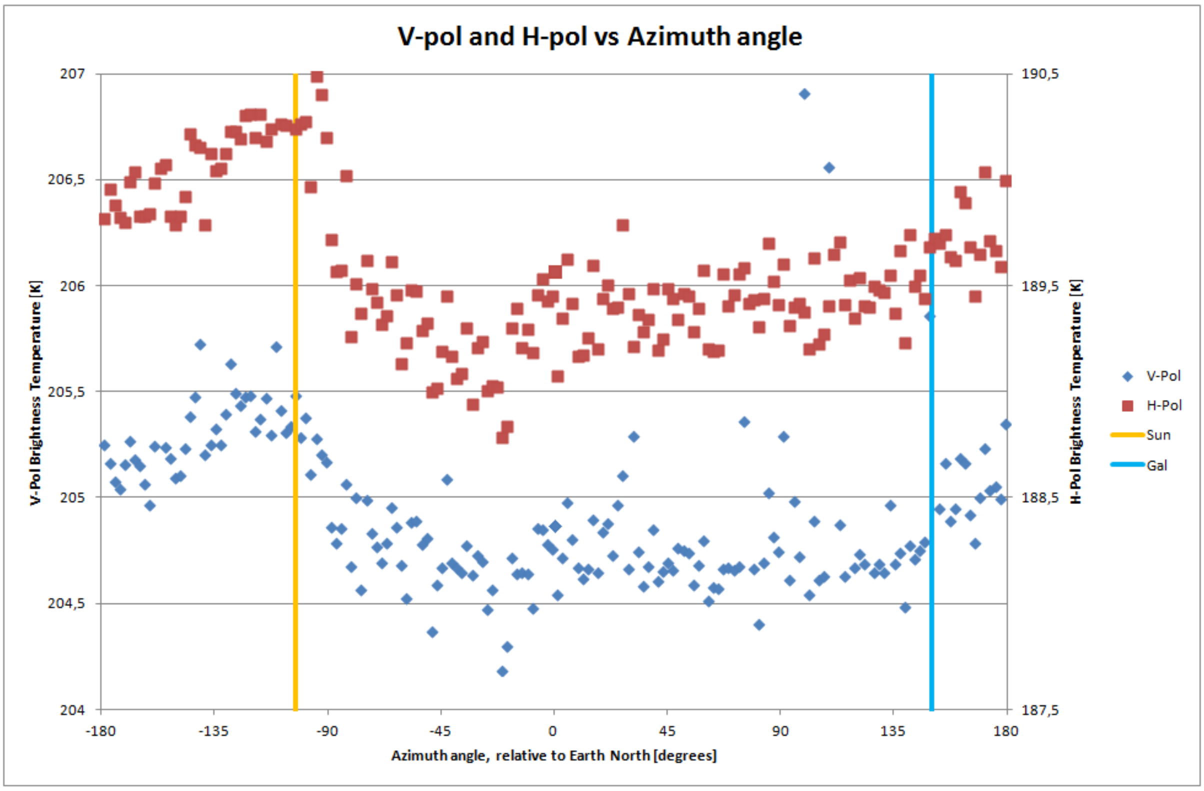


Figure 3.10.11: Azimuth signature for PM circle flight at 35 degrees incidence angle. $T_V$ and $T_H$ as a function of look direction relative to Earth North.

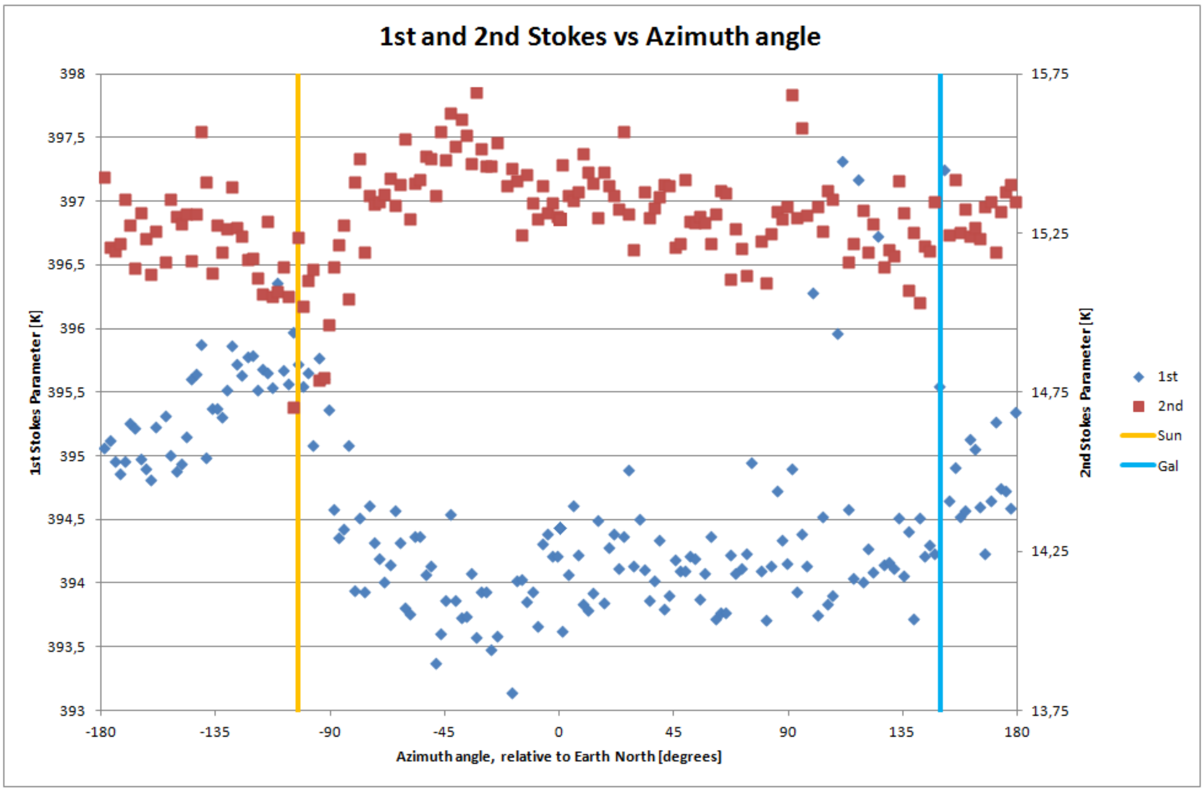


Figure 3.10.12: Azimuth signature for PM circle flight at 35 degrees incidence angle. 1st and 2nd true Stokes parameters as a function of look direction relative to Earth North.

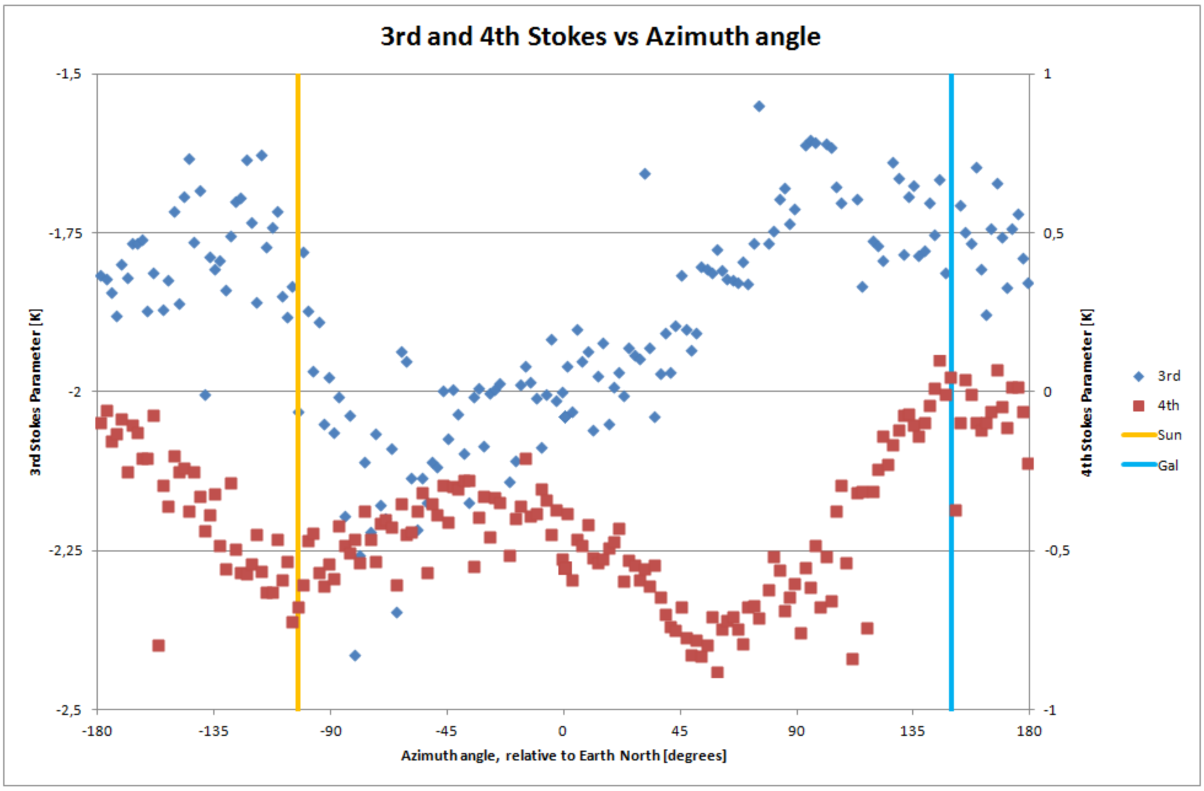


Figure 3.10.13: Azimuth signature for PM circle flight at 35 degrees incidence angle. 3rd and 4th Stokes parameters as a function of look direction relative to Earth North.

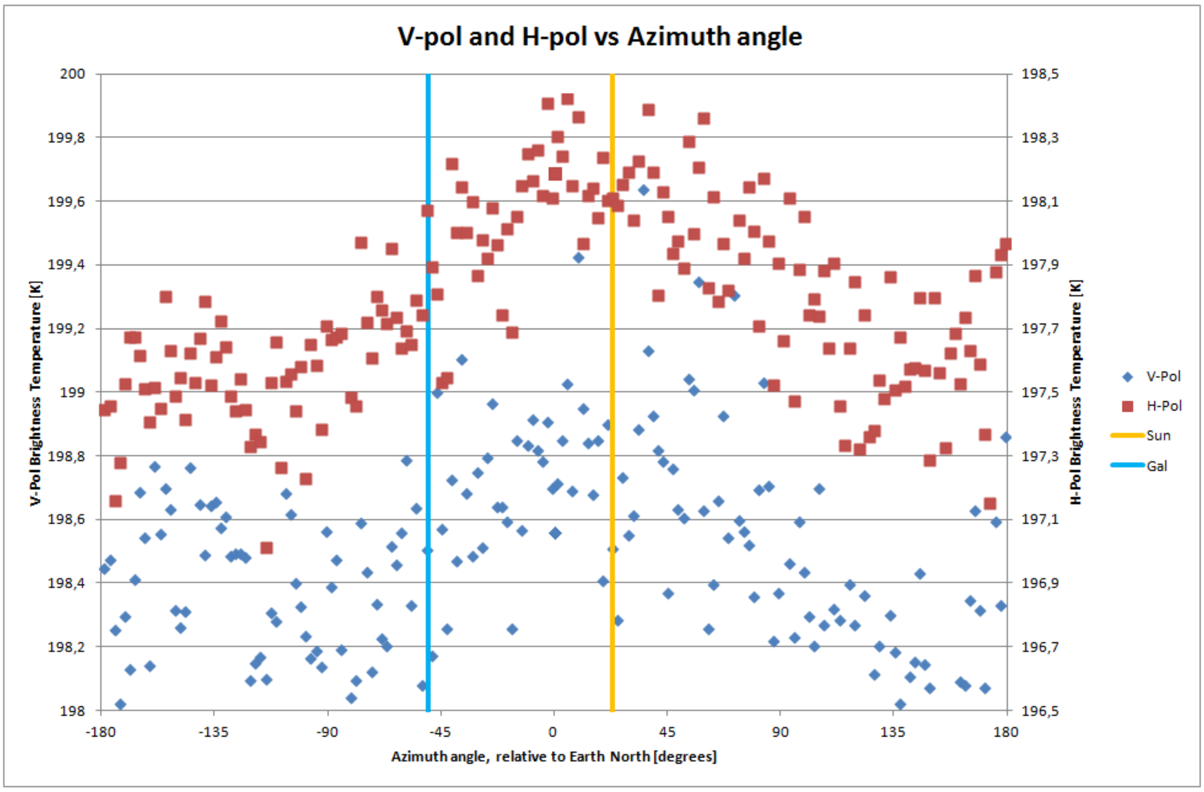


Figure 3.10.14: Azimuth signature for AM circle flight at 10 degrees incidence angle. $T_V$ and $T_H$ as a function of look direction relative to Earth North.

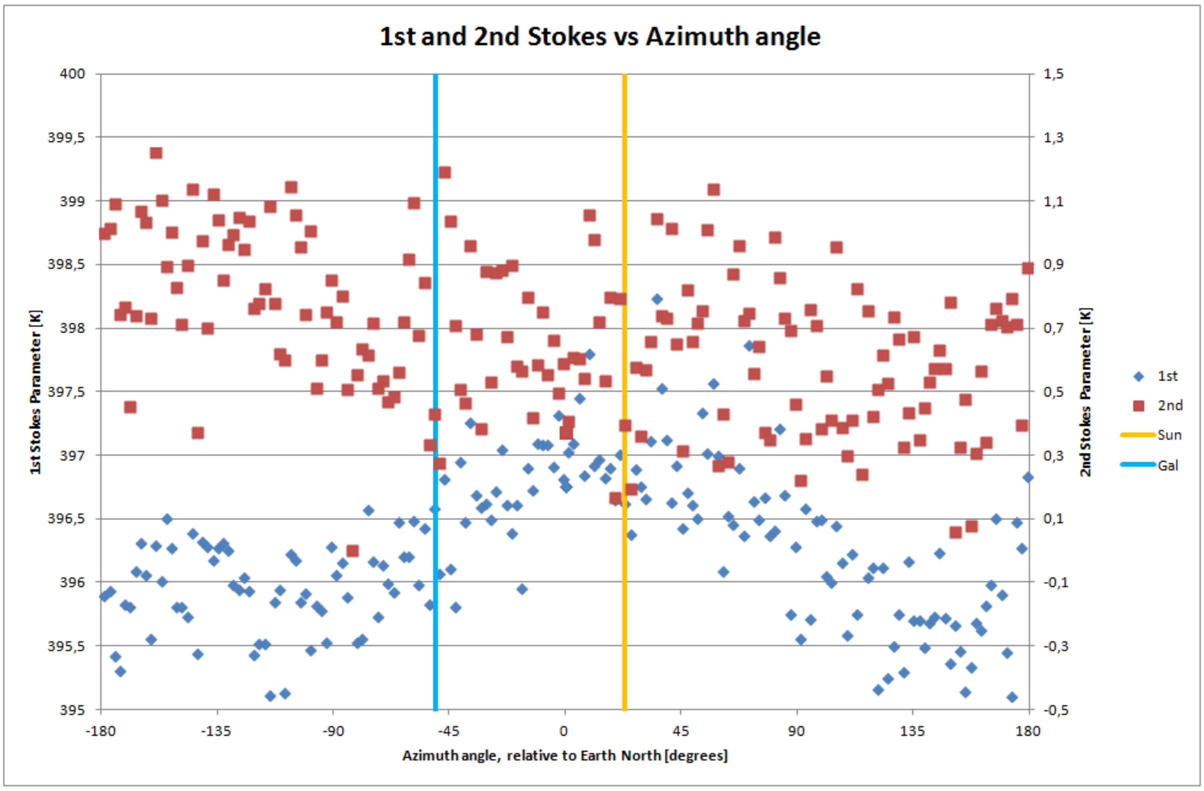


Figure 3.10.15: Azimuth signature for AM circle flight at 10 degrees incidence angle. 1st and 2nd true Stokes parameters as a function of look direction relative to Earth North.

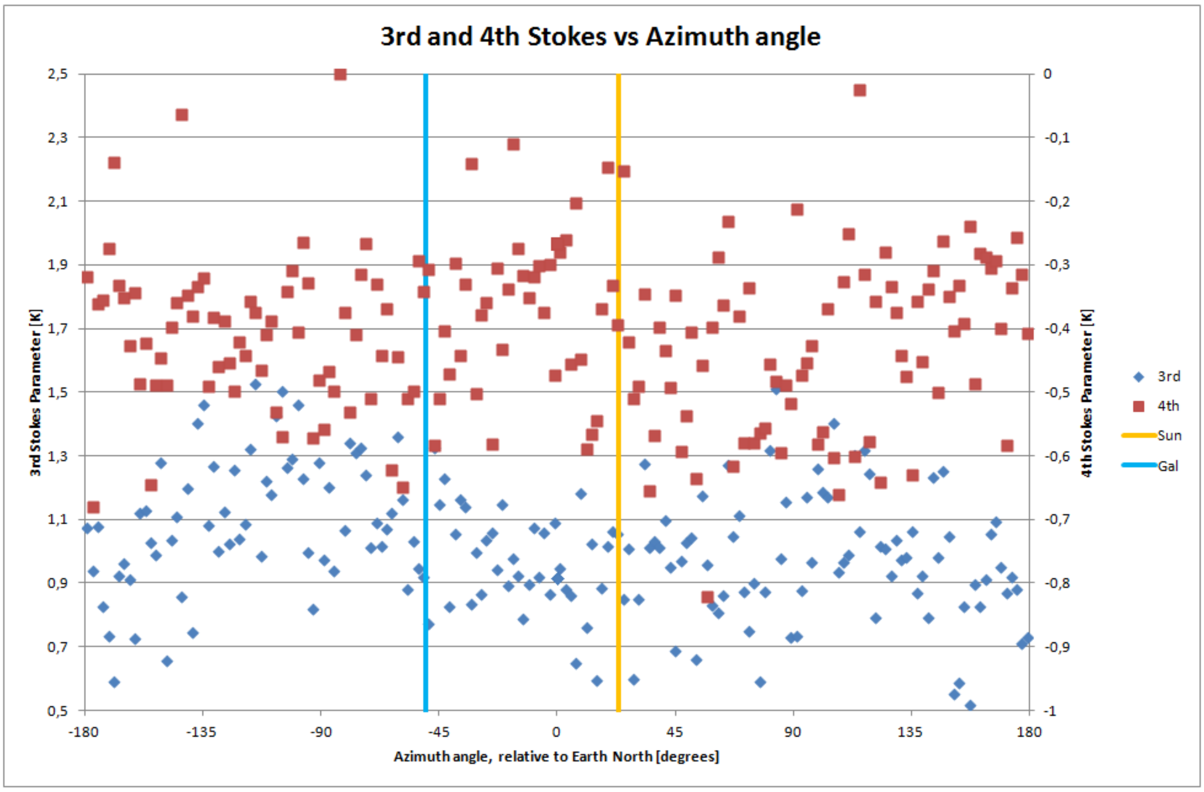


Figure 3.10.16: Azimuth signature for AM circle flight at 10 degrees incidence angle. 3rd and 4th Stokes parameters as a function of look direction relative to Earth North.

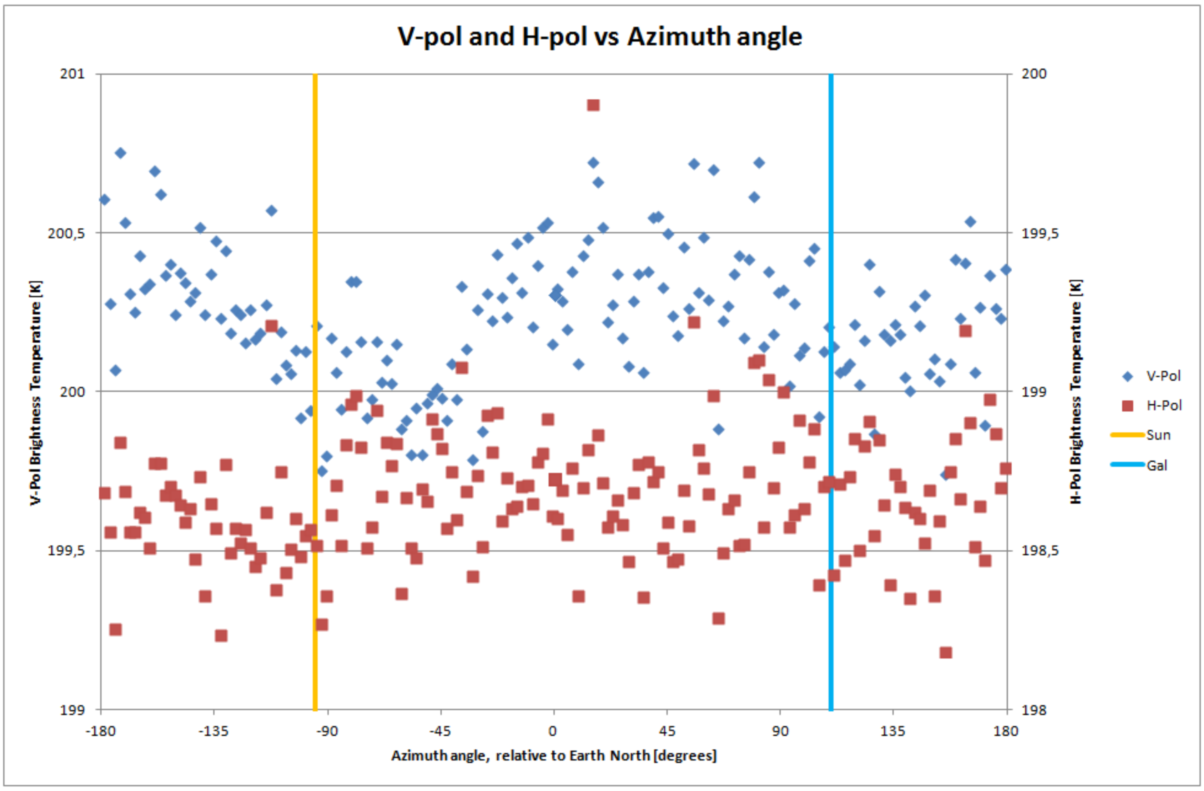


Figure 3.10.17: Azimuth signature for PM circle flight at 10 degrees incidence angle. $T_V$ and $T_H$ as a function of look direction relative to Earth North.

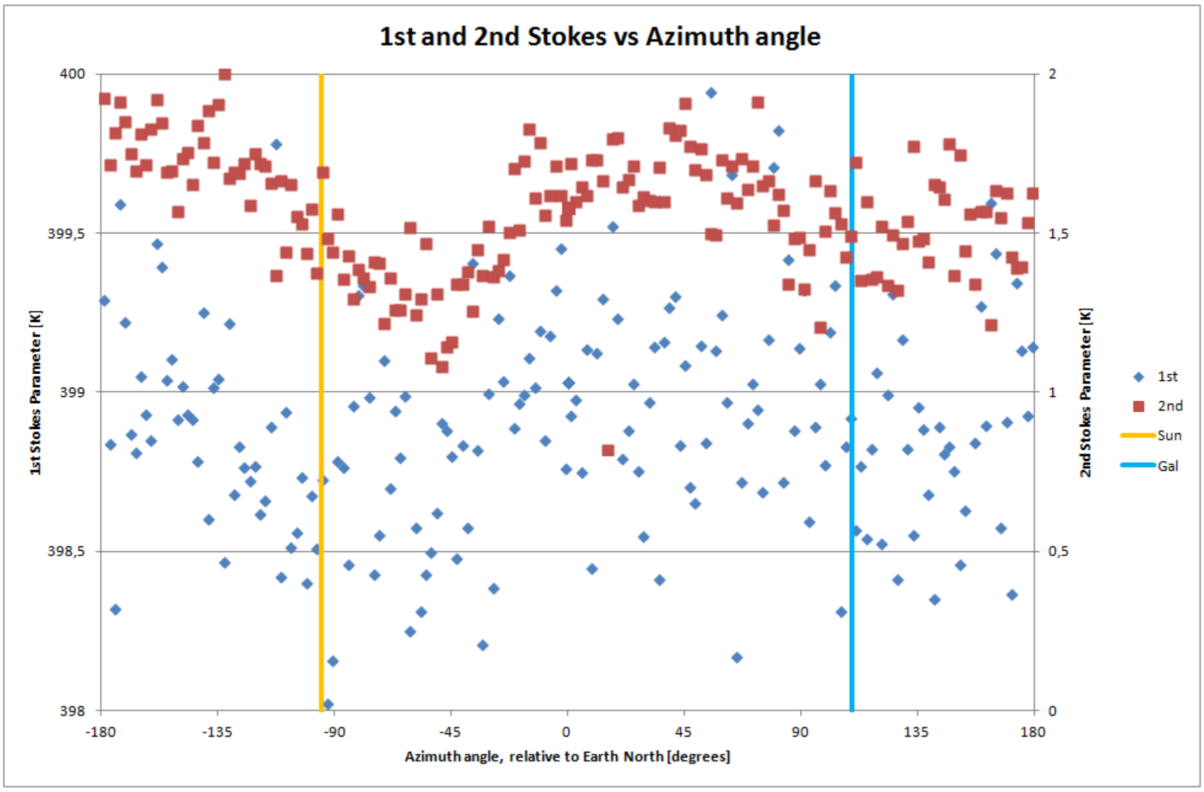


Figure 3.10.18: Azimuth signature for PM circle flight at 10 degrees incidence angle. 1st and 2nd true Stokes parameters as a function of look direction relative to Earth North.

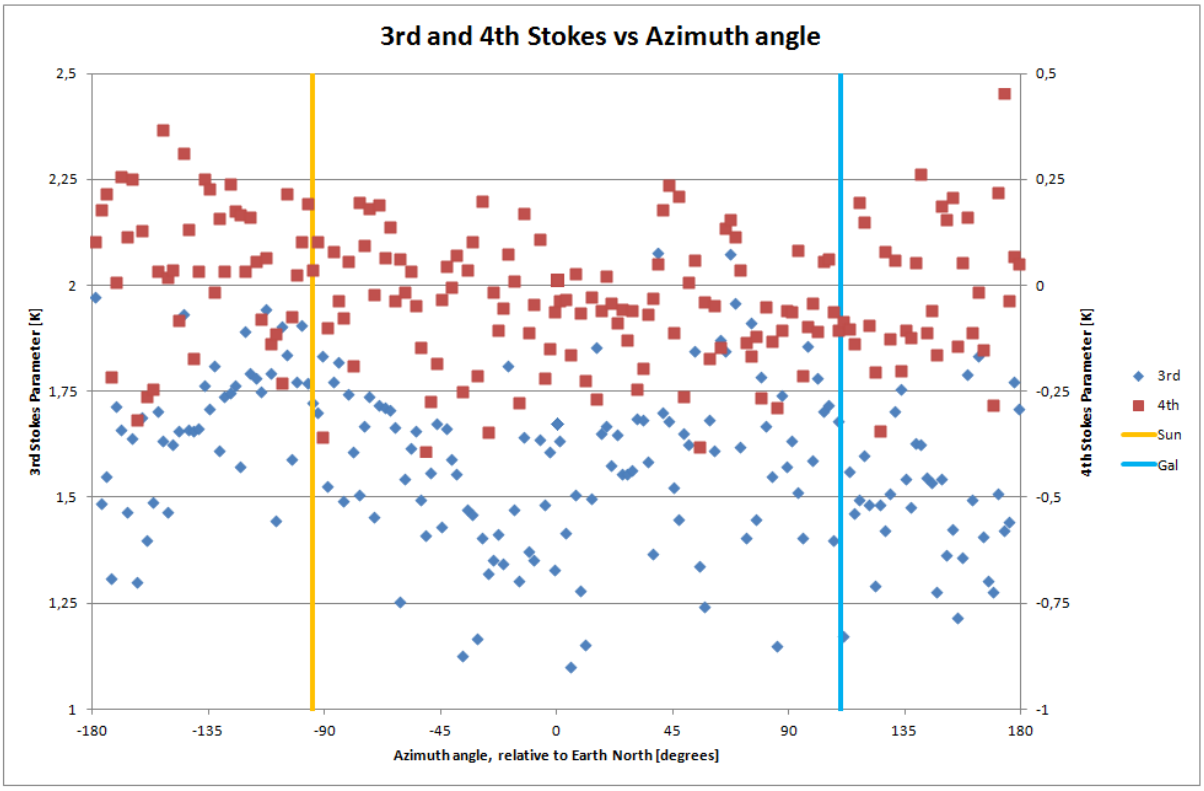


Figure 3.10.19: Azimuth signature for PM circle flight at 10 degrees incidence angle. 3rd and 4th Stokes parameters as a function of look direction relative to Earth North.

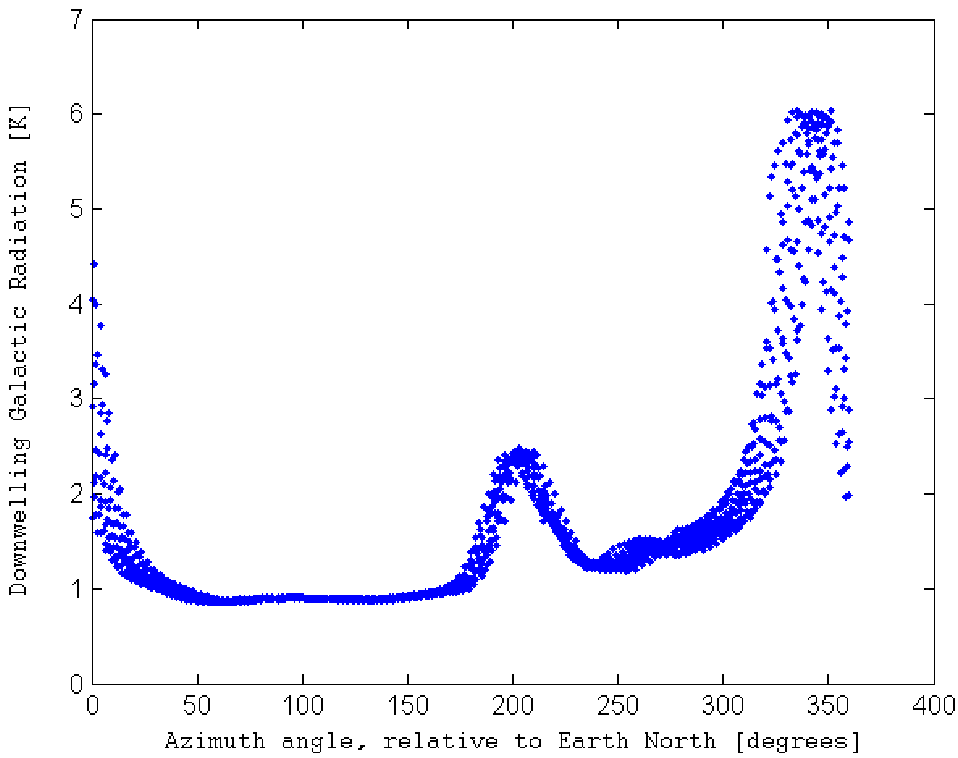


Figure 3.10.20: Downwelling Galactic background radiation corresponding to the AM circle flight at 55 degrees incidence angle.

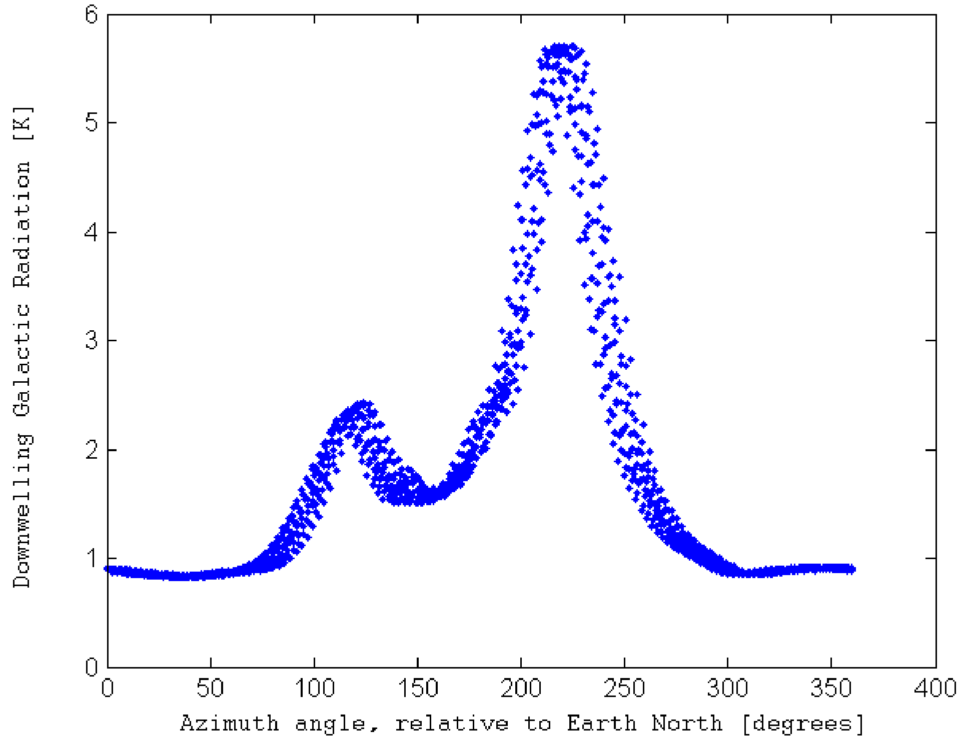


Figure 3.10.21: Downwelling Galactic background radiation corresponding to the PM circle flight at 55 degrees incidence angle.

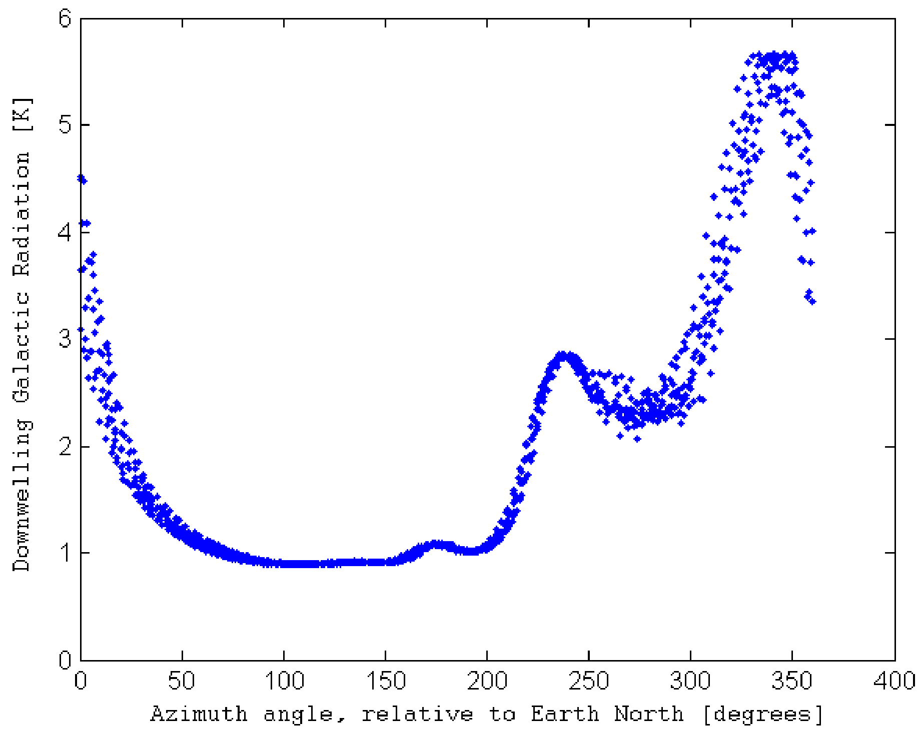


Figure 3.10.22: Downwelling Galactic background radiation corresponding to the AM circle flight at 35 degrees incidence angle.

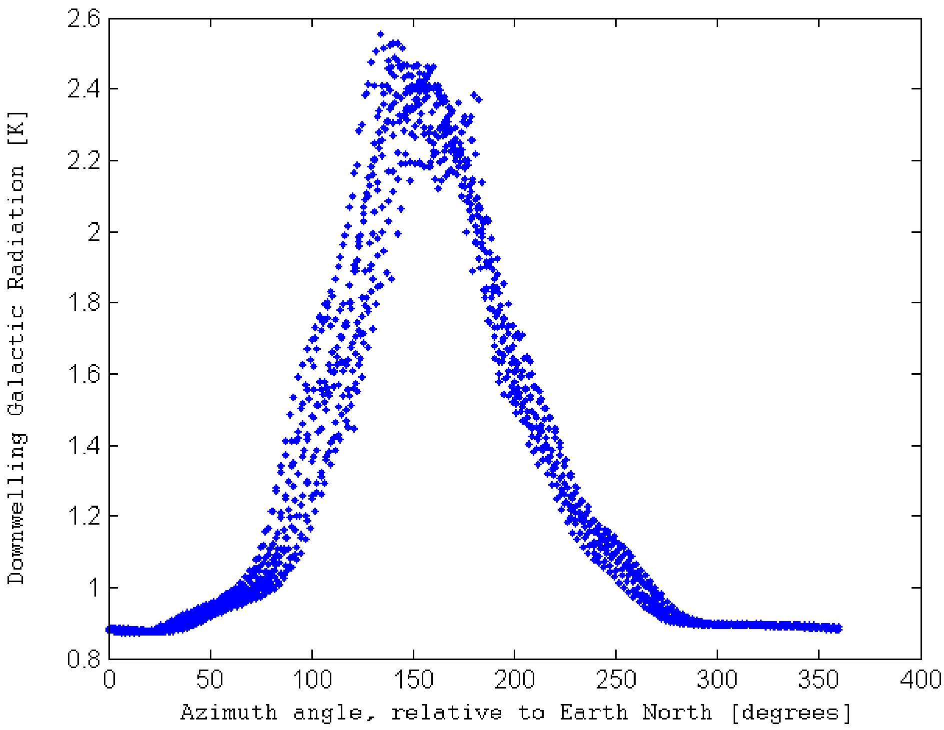


Figure 3.10.23: Downwelling Galactic background radiation corresponding to the PM circle flight at 35 degrees incidence angle.

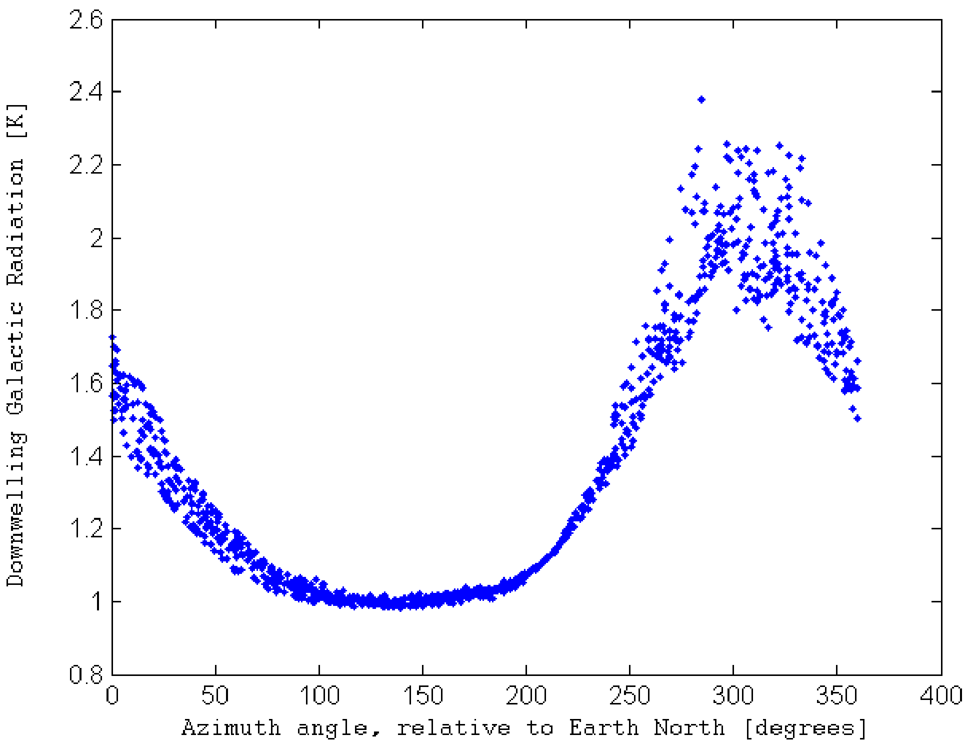


Figure 3.10.24: Downwelling Galactic background radiation corresponding to the AM circle flight at 10 degrees incidence angle.

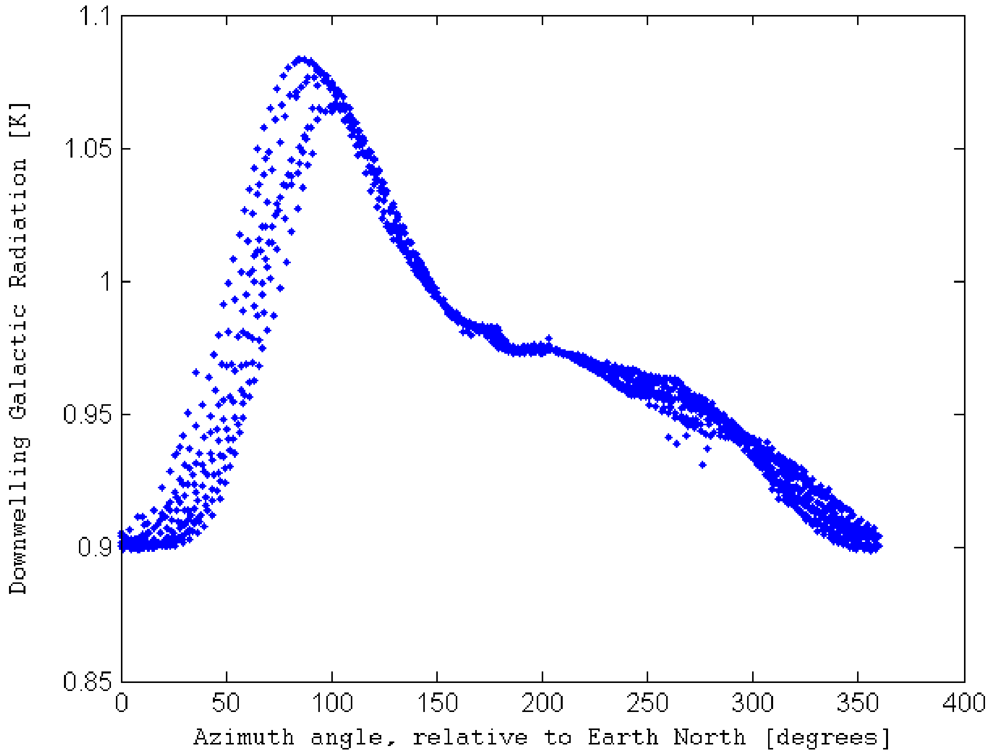


Figure 3.10.25: Downwelling Galactic background radiation corresponding to the PM circle flight at 10 degrees incidence angle.

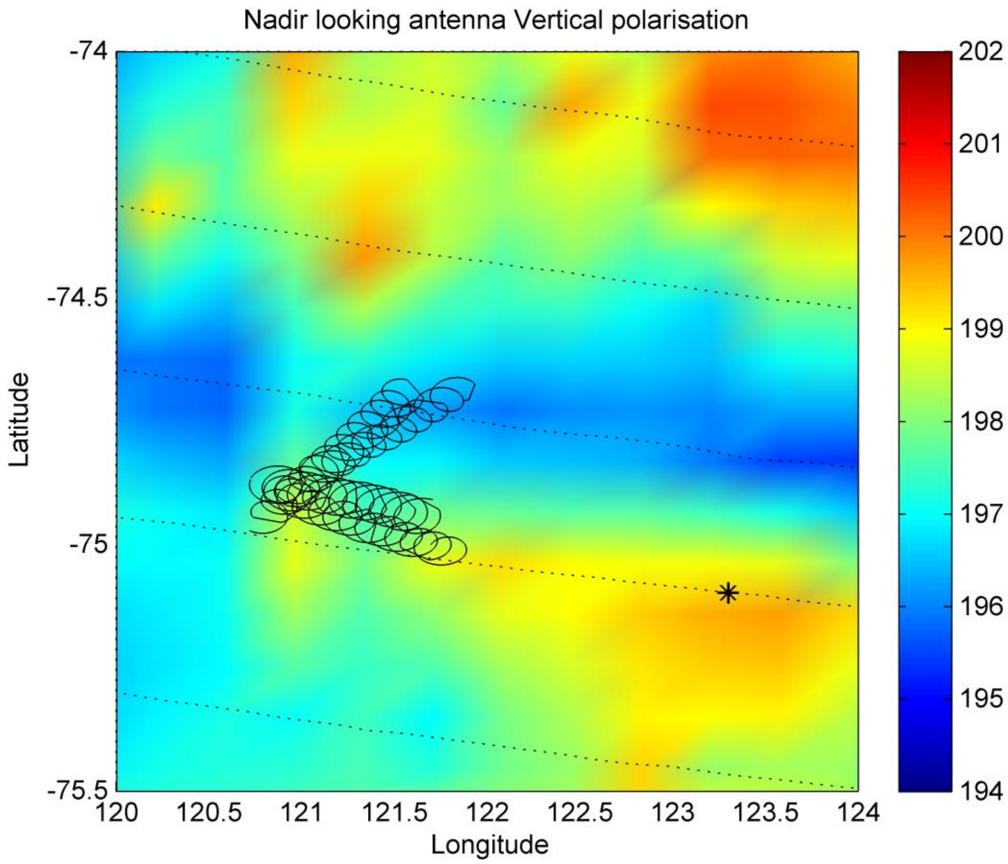


Figure 3.10.26: Zoomed plot of the interpolated survey map into the position of the circle flights. Map colors show data from near nadir channel, V-Pol.

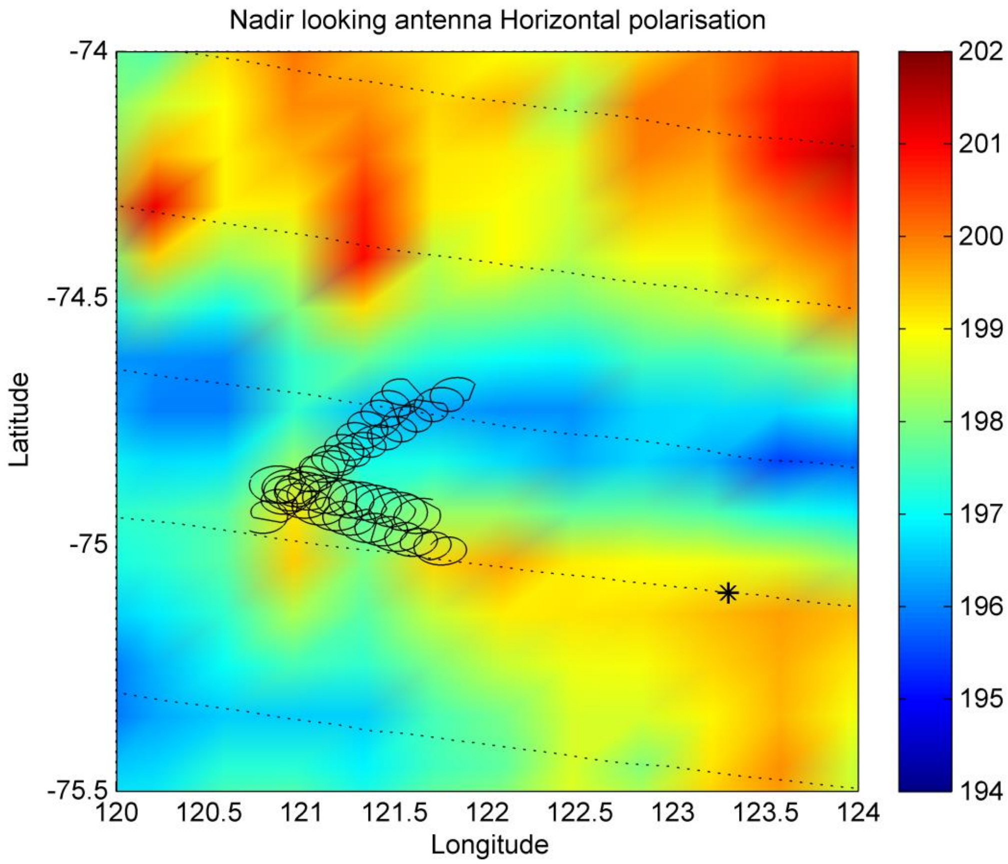


Figure 3.10.27: Zoomed plot of the interpolated survey map into the position of the circle flights. Map colors show data from near nadir channel, H-Pol.

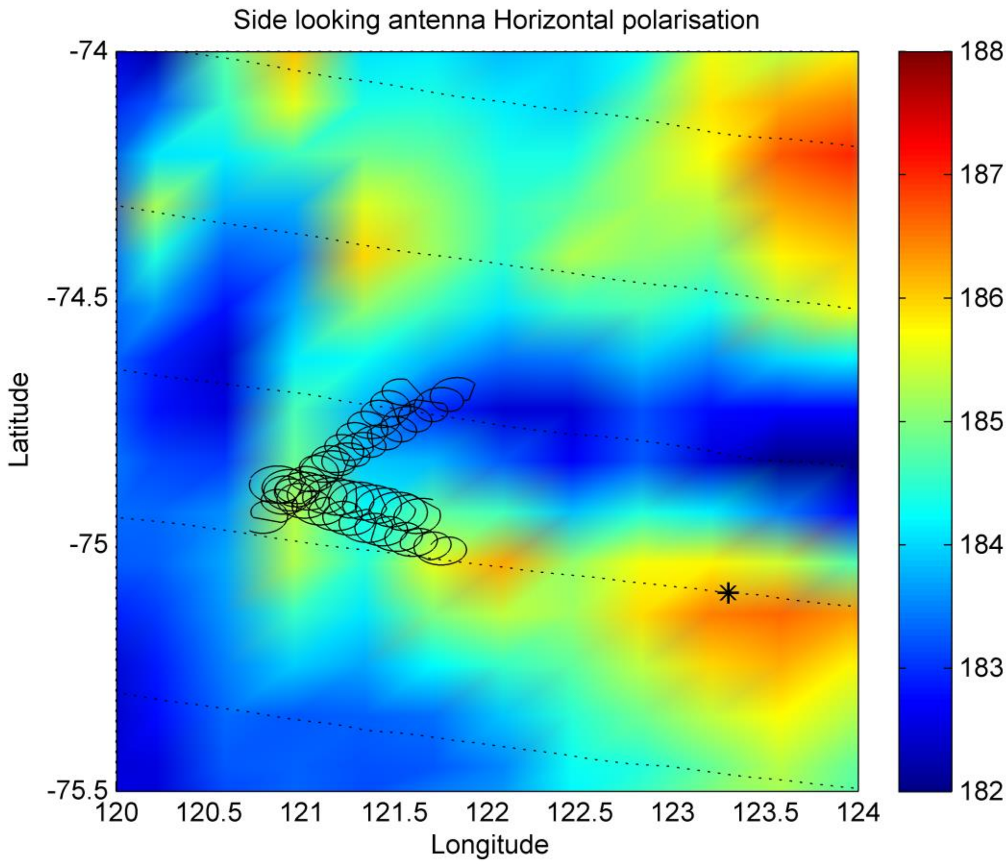


Figure 3.10.28: Zoomed plot of the interpolated survey map into the position of the circle flights. Map colors show data from 45 degrees incidence angle channel, V-Pol.

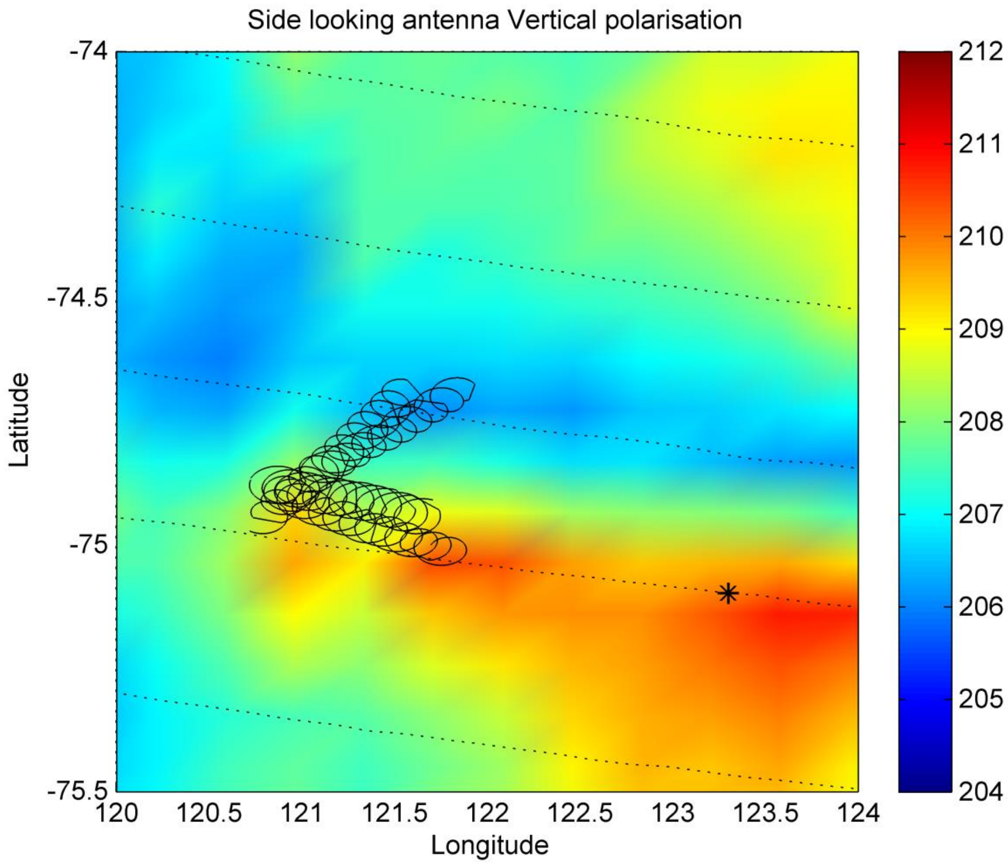


Figure 3.10.29: Zoomed plot of the interpolated survey map into the position of the circle flights. Map colors show data from 45 degrees incidence angle channel, H-Pol.

# 4. BRIGHTNESS TEMPERATURE DATA ON FLIGHT PATTERNS

A good way of giving an overview of the data is to plot brightness temperature data on the flight tracks, which is done on Figure 4.1 for the side looking antenna and in Figure 4.2 for the nadir looking antenna.

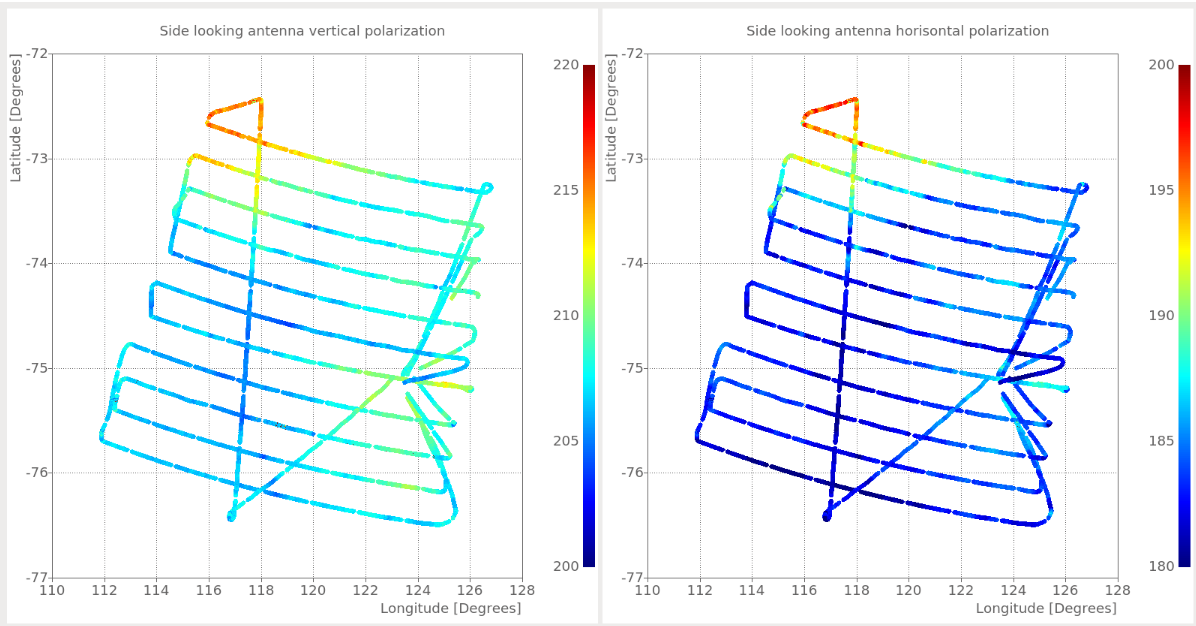


Figure 4.1: Side looking $T_{BV}$ and $T_{BH}$ data plotted on flight tracks

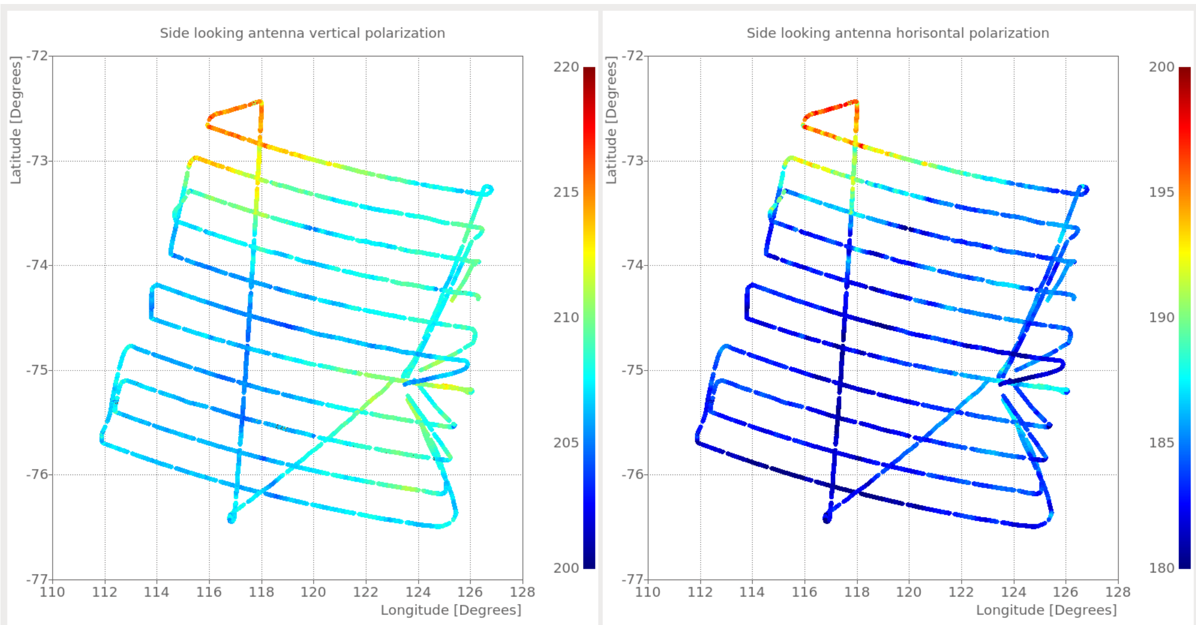


Figure 4.2: Nadir $T_{BV}$ and $T_{BH}$ data plotted on flight tracks

It is seen that the flight tracks fits well with the original plan as shown in Figure 2.1.

Survey line 1 is at the bottom of the figure whiles line 11 is at the top. Survey line 5 passes through Concordia. The tie line crosses the 11 survey lines from south to north.

The dynamic range of brightness temperatures in each plot is approaching 20 K, so it is immediately clear that the Dome C area does not present us with a uniform, homogeneous brightness temperature map. Especially the northern part of the plots reveals a significant increase in brightness temperature, which of course was already known from SMOS imagery. But also obvious is large smaller scales variation along the lines. Much more about this in following chapters.

The highly varying brightness temperature on the flights in and out of Concordia most likely reflects low altitude. Especially the nadir looking antenna may see larger contributions originating from reflections from the aircraft at low altitude.

# 5. INTERPOLATED 2D IMAGERY

This chapter provides interpolated 2D imagery for the entire survey area based on the survey lines 1 to 11 and the tie line. More detailed interpolated 2D imagery near Concordia base on the star flight lines is also provided. A zoom in on the 2D imagery covering the circle flight area was provided in Chapter 3.

## 5.1 Interpolated 2D Survey Data

The data set already shown in the previous chapter has been interpolated and smoothed in order to provide 2D imagery of the survey area, see Figures 5.1.1 – 5.1.3.

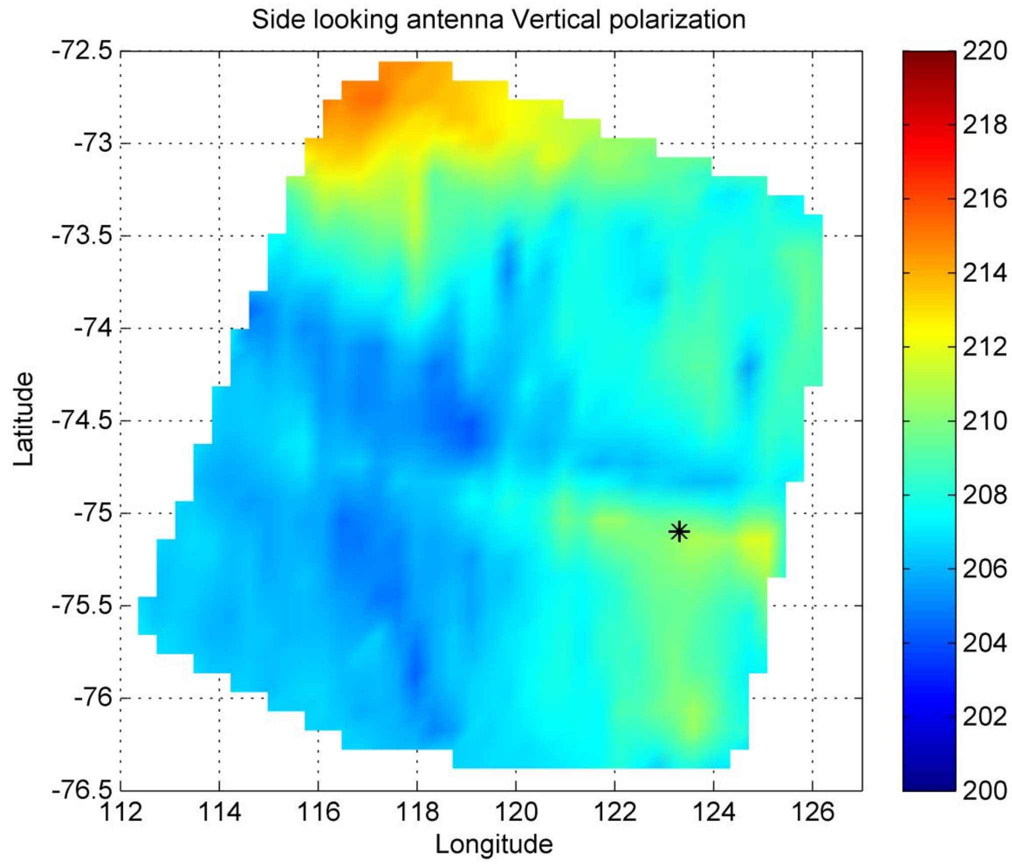


Figure 5.1.1: 2D data obtained by interpolating and smoothing survey and tie line data from the side looking antenna, vertical polarization. Concordia is marked by an asterisk.

The relatively large dynamic brightness temperature range as already noted in Chapter 4 is again easily seen. Especially the northern part of the images reveals a significant increase in brightness temperature. But also the area around Concordia shows elevated temperatures. It seems like Concordia actually is situated on a hilltop overlooking lowlands in most directions. This of course presents special challenges when comparing DOMEX data with DOMECair data.

Giovanni's low brightness temperature area (around 74.5 – 75 & 116 – 119) is clearly revealed. The circle flights were carried out just west of Concordia. Location and zoom are provided in Chapter 3 where they are used to assess calibration issues.

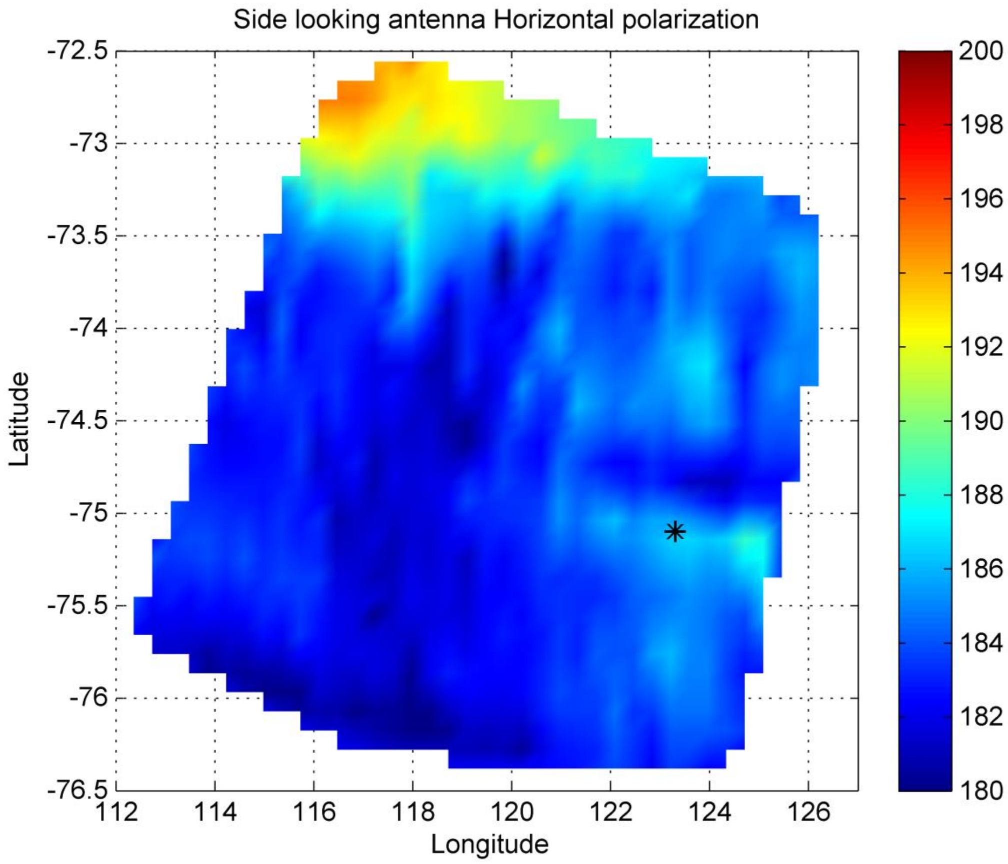


Figure 5.1.2: 2D data obtained by interpolating and smoothing survey and tie line data from the side looking antenna, horizontal polarization. Concordia is marked by an asterisk.

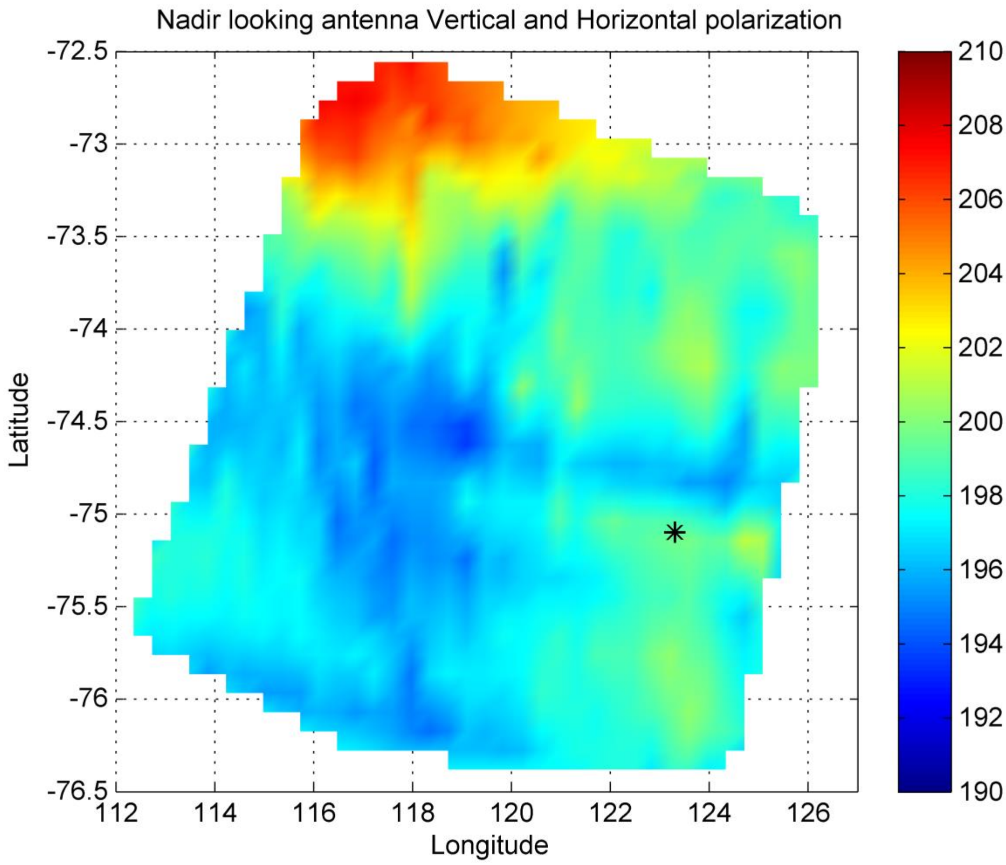


Figure 5.1.3: 2D data obtained by interpolating and smoothing survey and tie line data from the nadir looking antenna, averaging vertical and horizontal polarizations. Concordia is marked by an asterisk.

## 5.2 Interpolated 2D Concordia Data

The star flight lines across Concordia are denser that the survey lines and it is therefore possible to create a better 2D interpolation of the area around Concordia, see Figures 5.2.1 – 5.2.3.

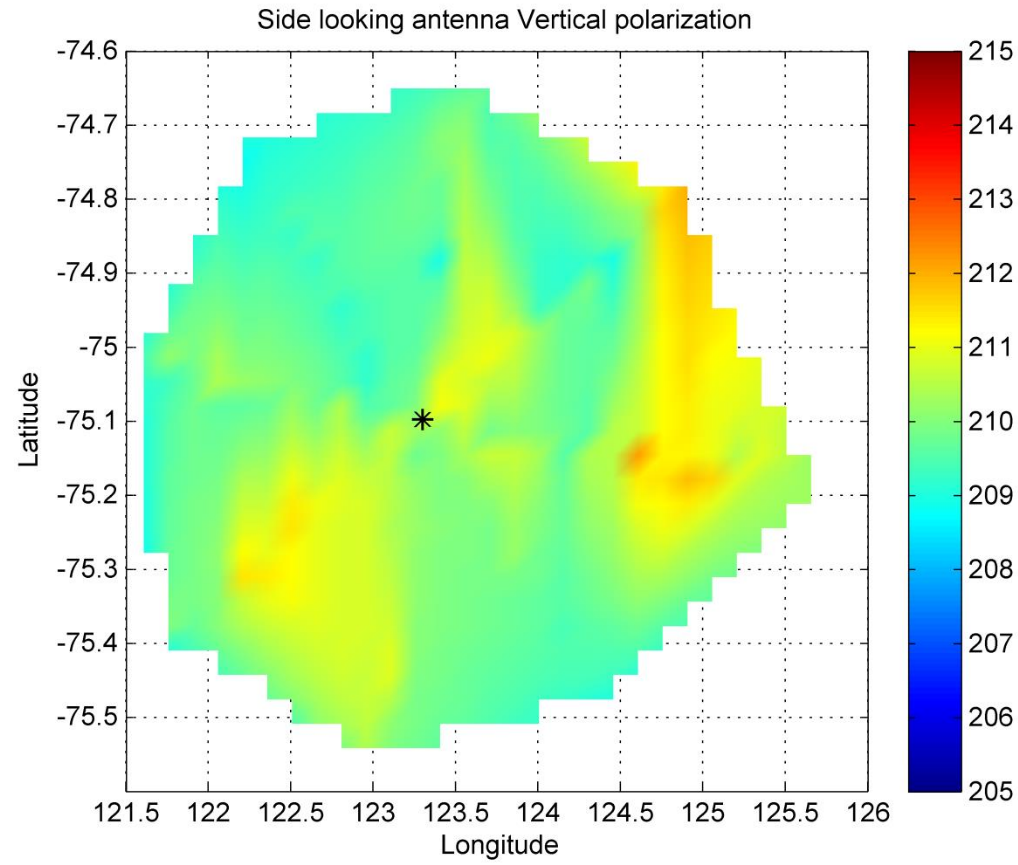


Figure 5.2.1: 2D data obtained by interpolating and smoothing star line data from the side looking antenna, vertical polarization. Concordia is marked by an asterisk.

Again it is seen that there is a surprisingly high variation in the brightness temperatures just around Concordia. Not only is Concordia placed on a larger brightness temperature plateau seen from the survey line interpolated 2D data, but just within a few kilometers a small saddle or ridge of several K is seen in the side looking data.

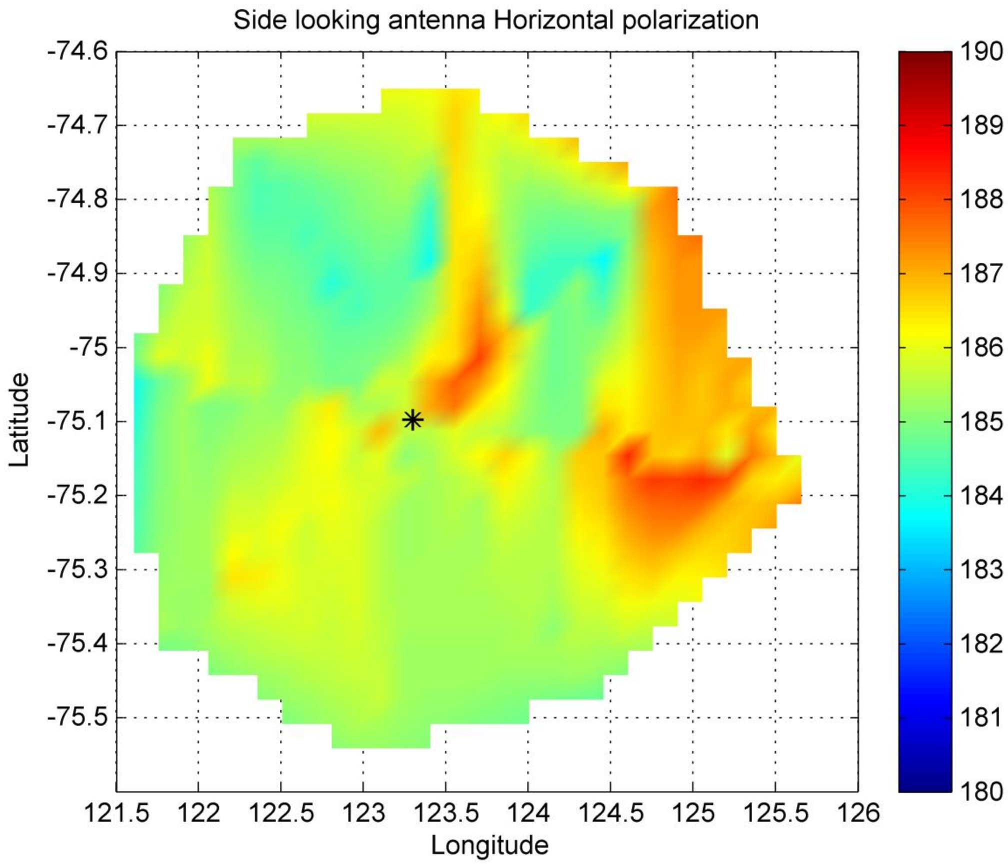


Figure 5.2.2: 2D data obtained by interpolating and smoothing star line data from the side looking antenna, horizontal polarization. Concordia is marked by an asterisk.

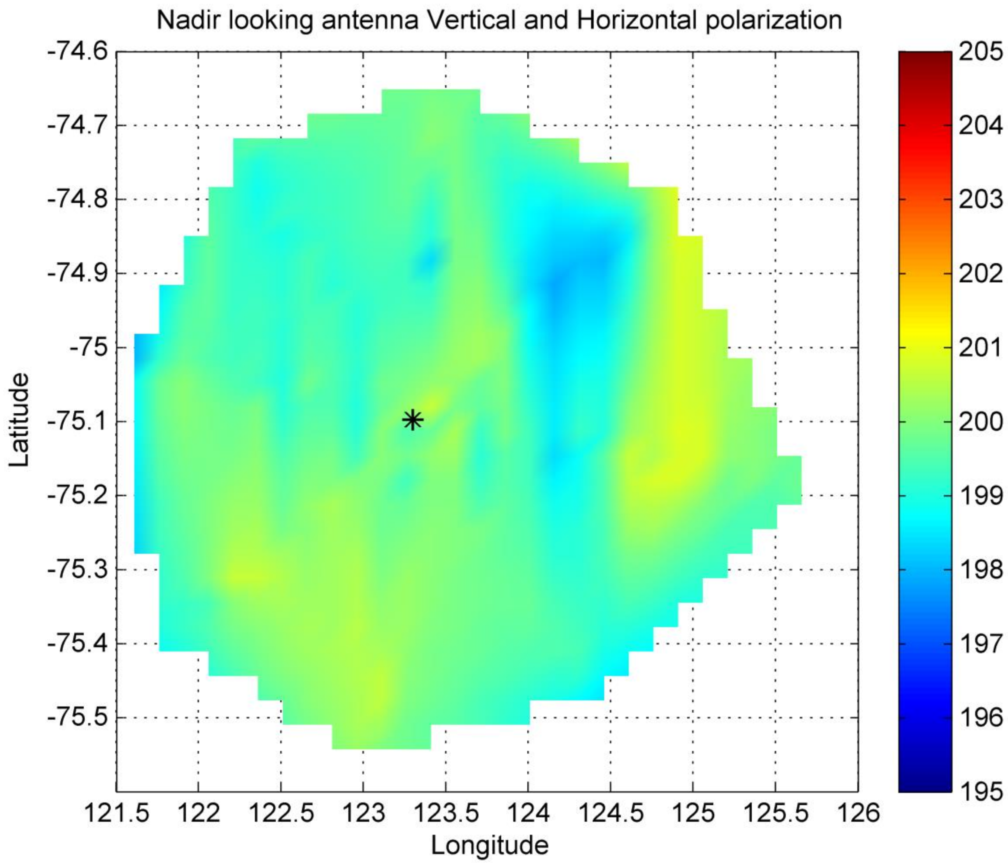


Figure 5.2.3: 2D data obtained by interpolating and smoothing star line data from the nadir looking antenna, averaging vertical and horizontal polarizations. Concordia is marked by an asterisk.

# 6. PROFILES

## 6.1 Presentation of Profiles

The profiles from the 11 survey lines and the tie line are shown in the Figures 6.1.1 to 6.1.24 on the following 24 pages. In order to ease comparison all survey line profiles has been scaled to display a distance of 375 km and a brightness temperature interval of 15 K. Only the tie line is longer and has a higher dynamic range. The full length and the 20 K brightness temperature interval displayed.

We observe a significant dynamic range even without taking the warm northern area into consideration. For example line 5, side looking V pol, Figure 6.1.10, displays values from 205 K to 213 K. Line 5, side looking H pol, Figure 6.1.10, shows within Giovannis triangle (ranging 60-130 km) a variation of 4.5 K over 6.5 km, i.e. a slope of almost 1 K / km!

We see Giovannis area with consistent, low brightness temperature values – but it is in fact not very homogeneous, especially in the east-west direction (see survey line 5, Figure 6.1.9 and 6.1.10), while it is somewhat better in the north-south direction (see tie line range 240 – 300 km, Figure 6.1.23 and 6.1.24). This observation is consistent with the pattern as seen in the 2D imagery in Chapter 5.

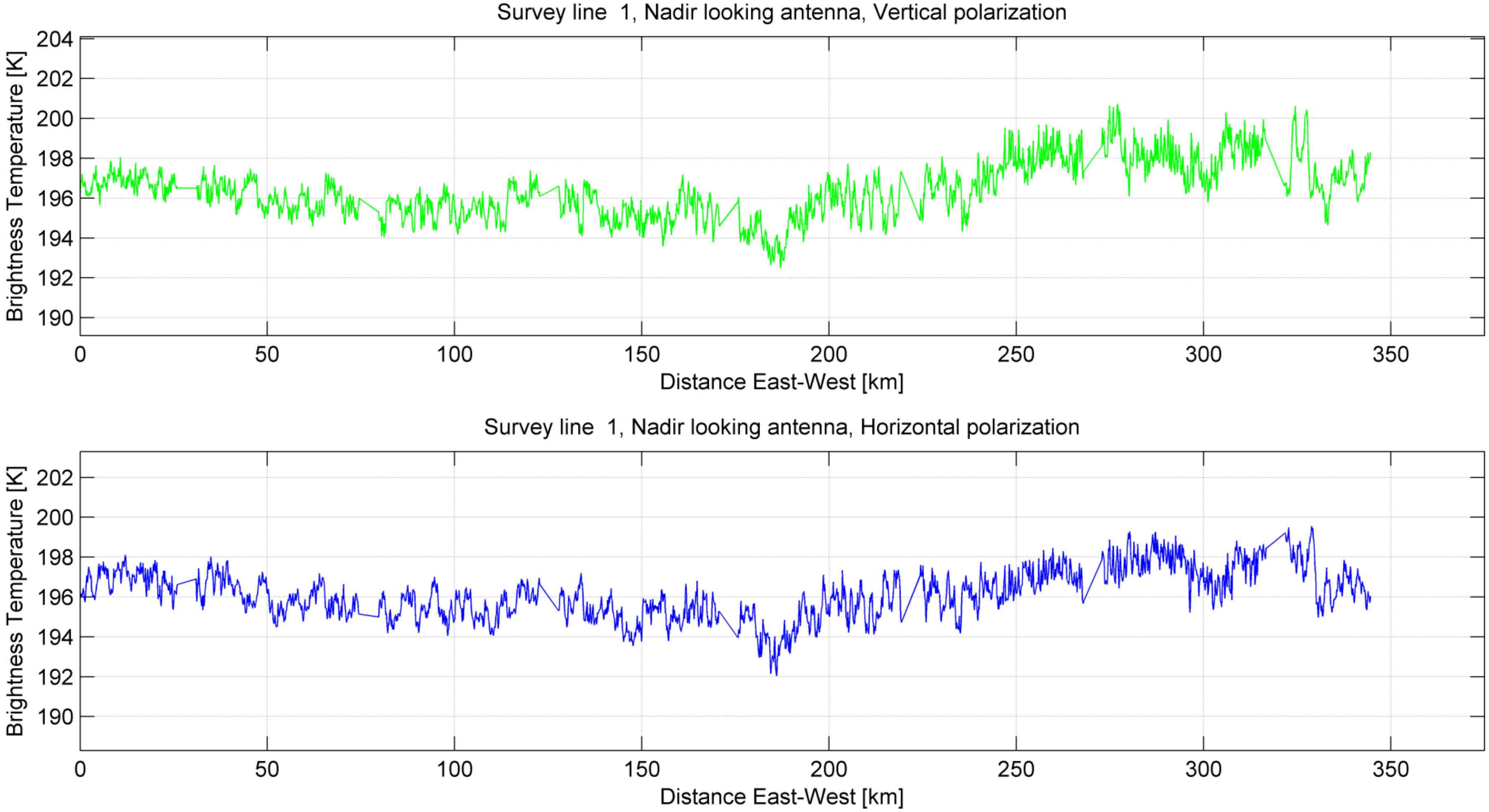


Figure 6.1.1: Survey line 1 profile: Nadir looking antenna.

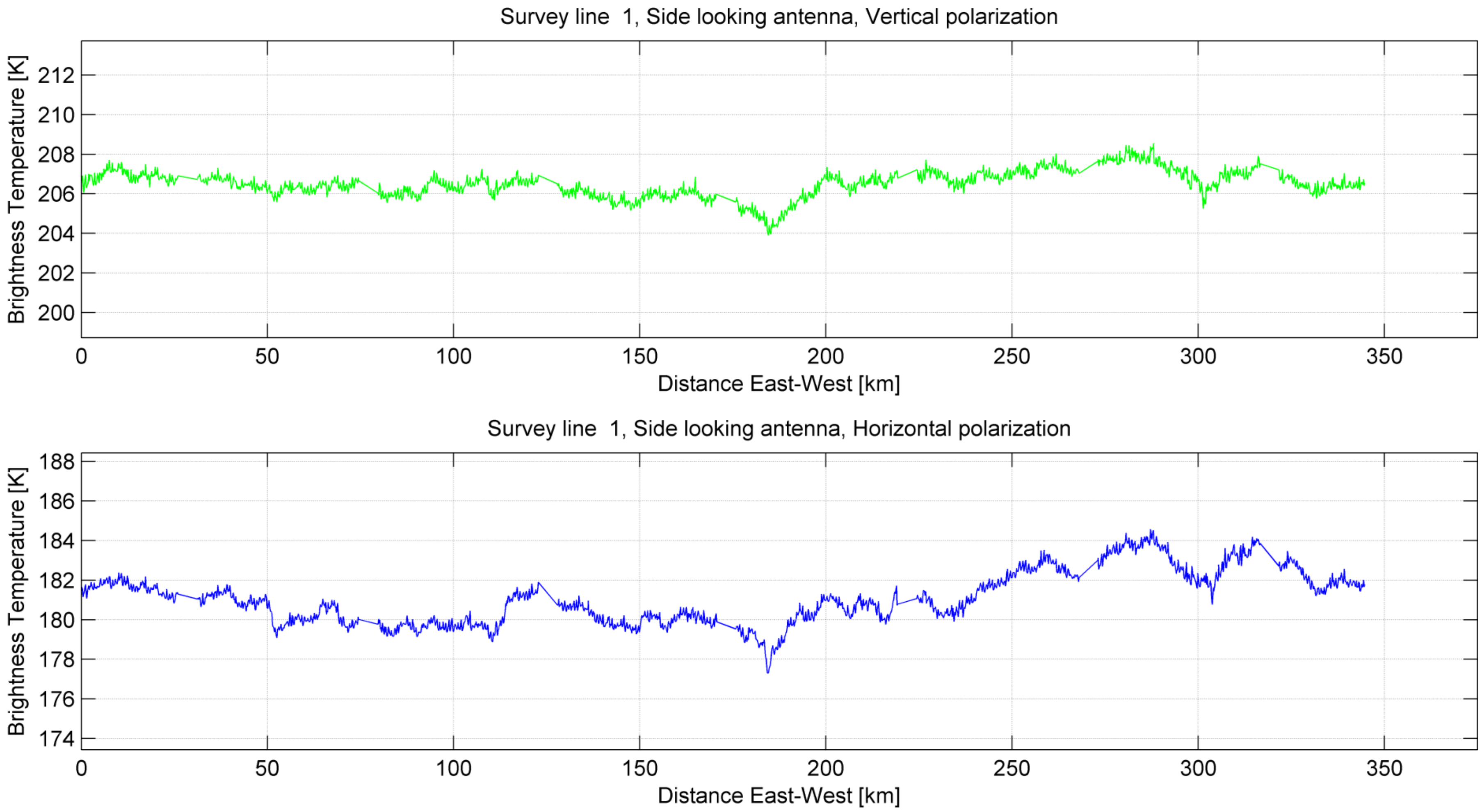


Figure 6.1.2: Survey line 1 profile, Side looking antenna.

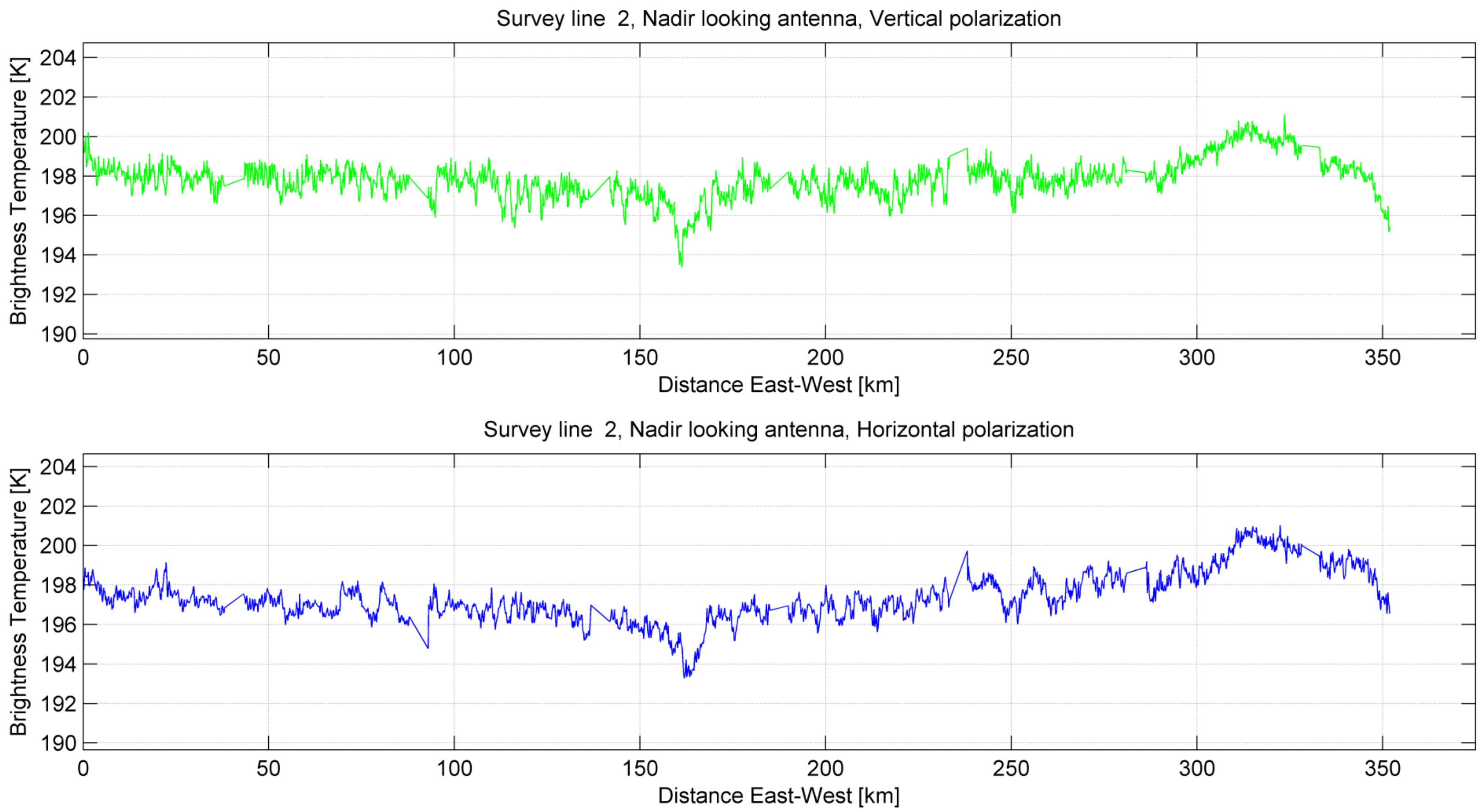


Figure 6.1.3: Survey line 2 profile, Nadir looking antenna.

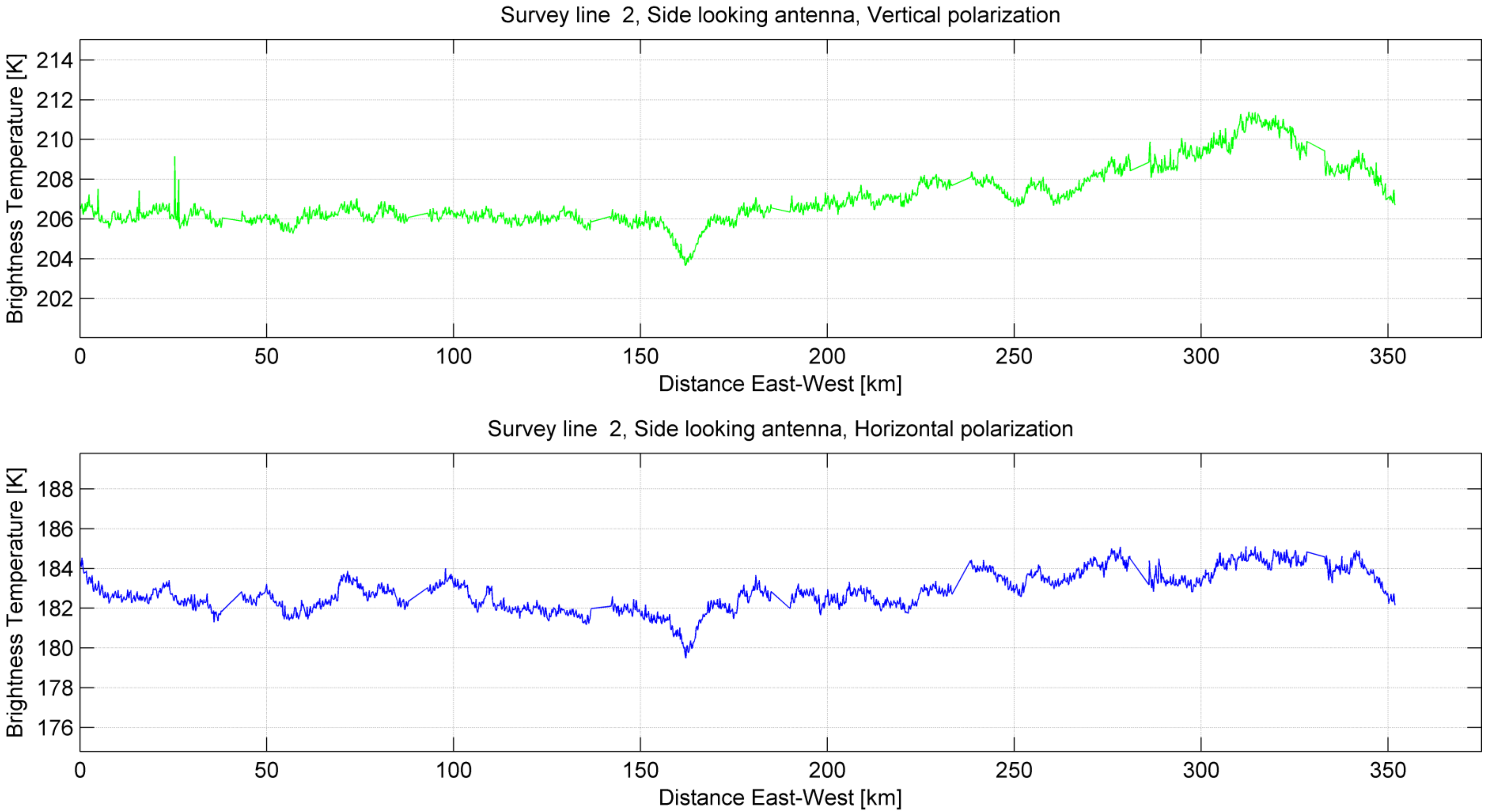


Figure 6.1.4: Survey line 2 profile: Side looking antenna.

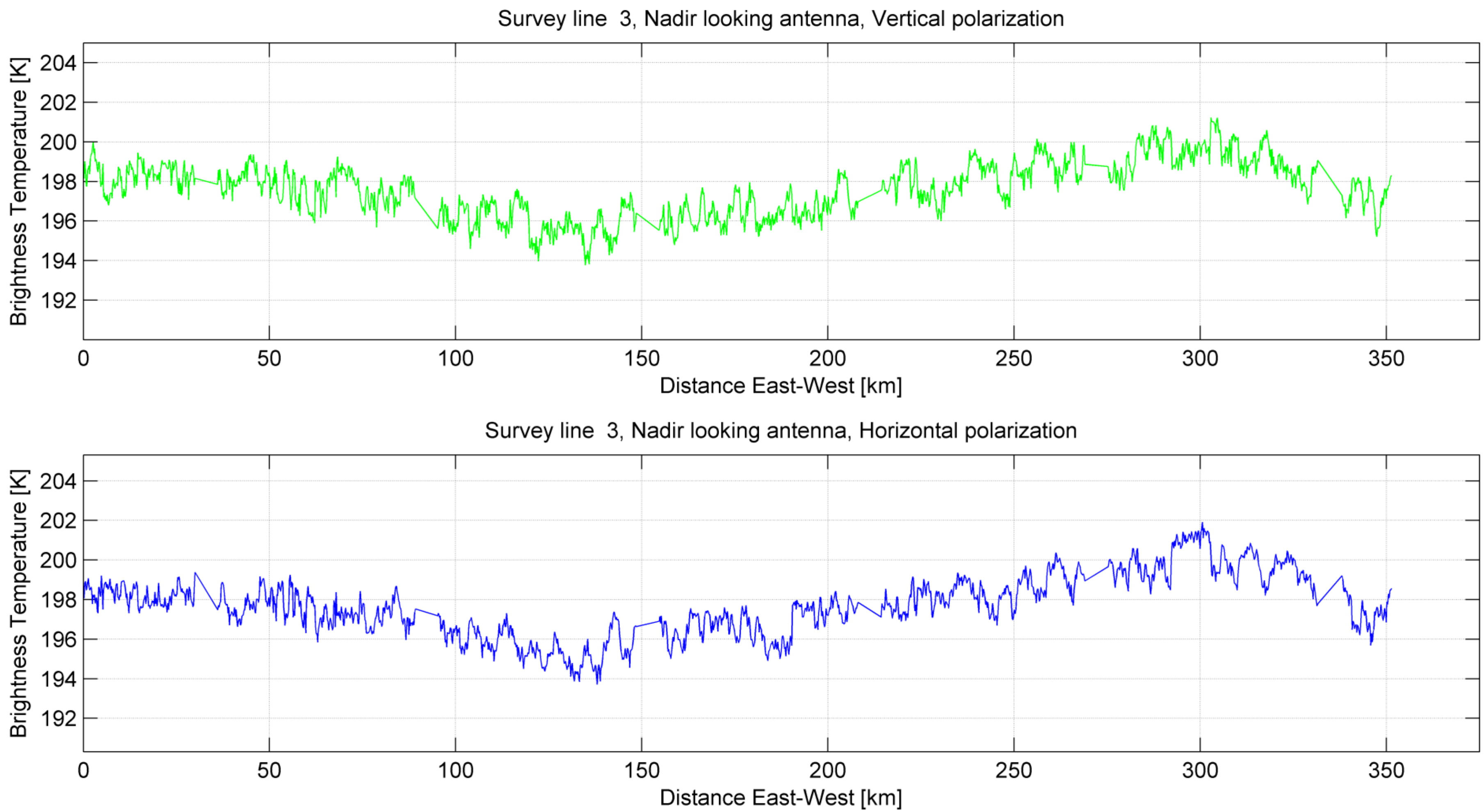


Figure 6.1.5: Survey line 3 profile: Nadir looking antenna.

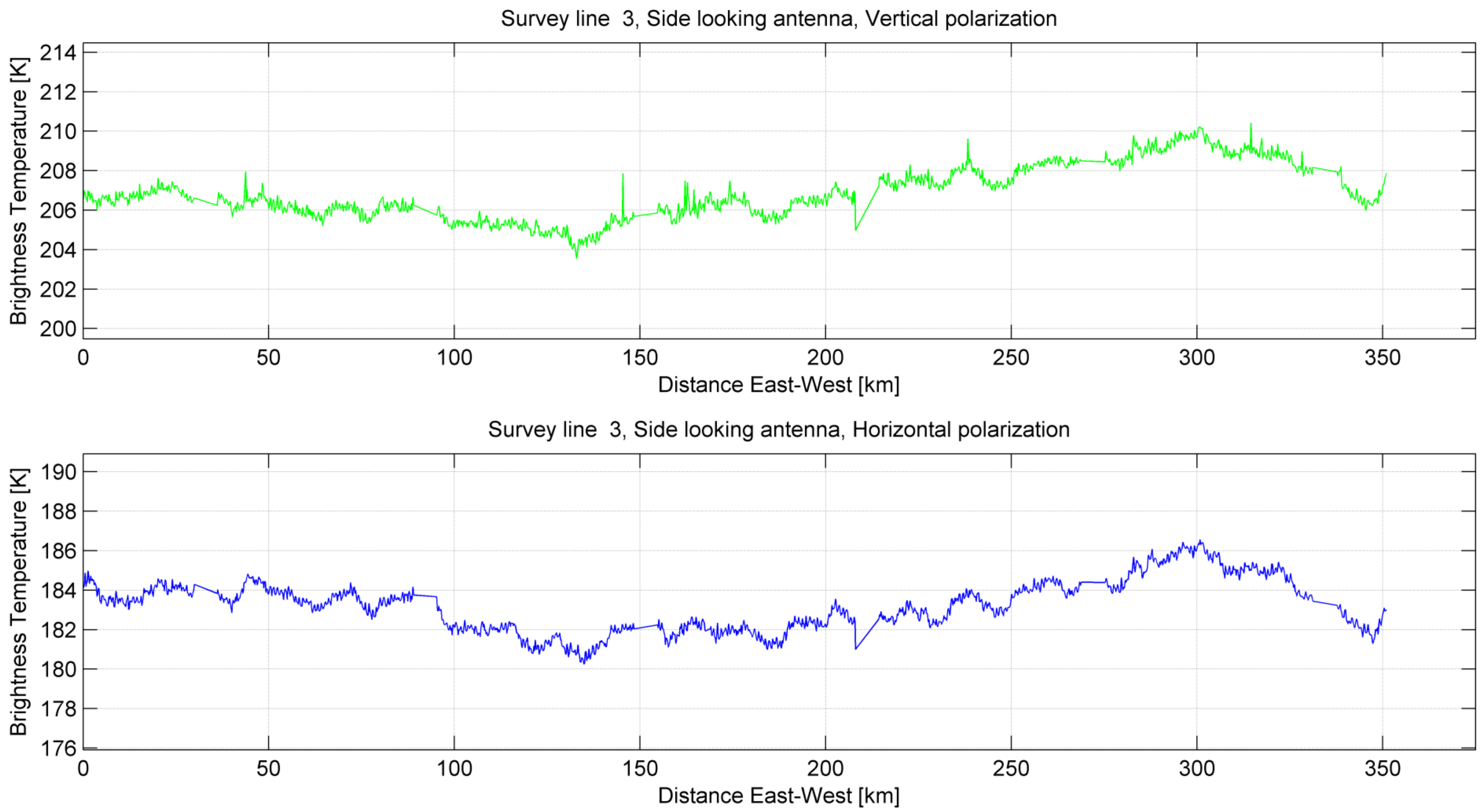


Figure 6.1.6: Survey line 3 profile: Side looking antenna.

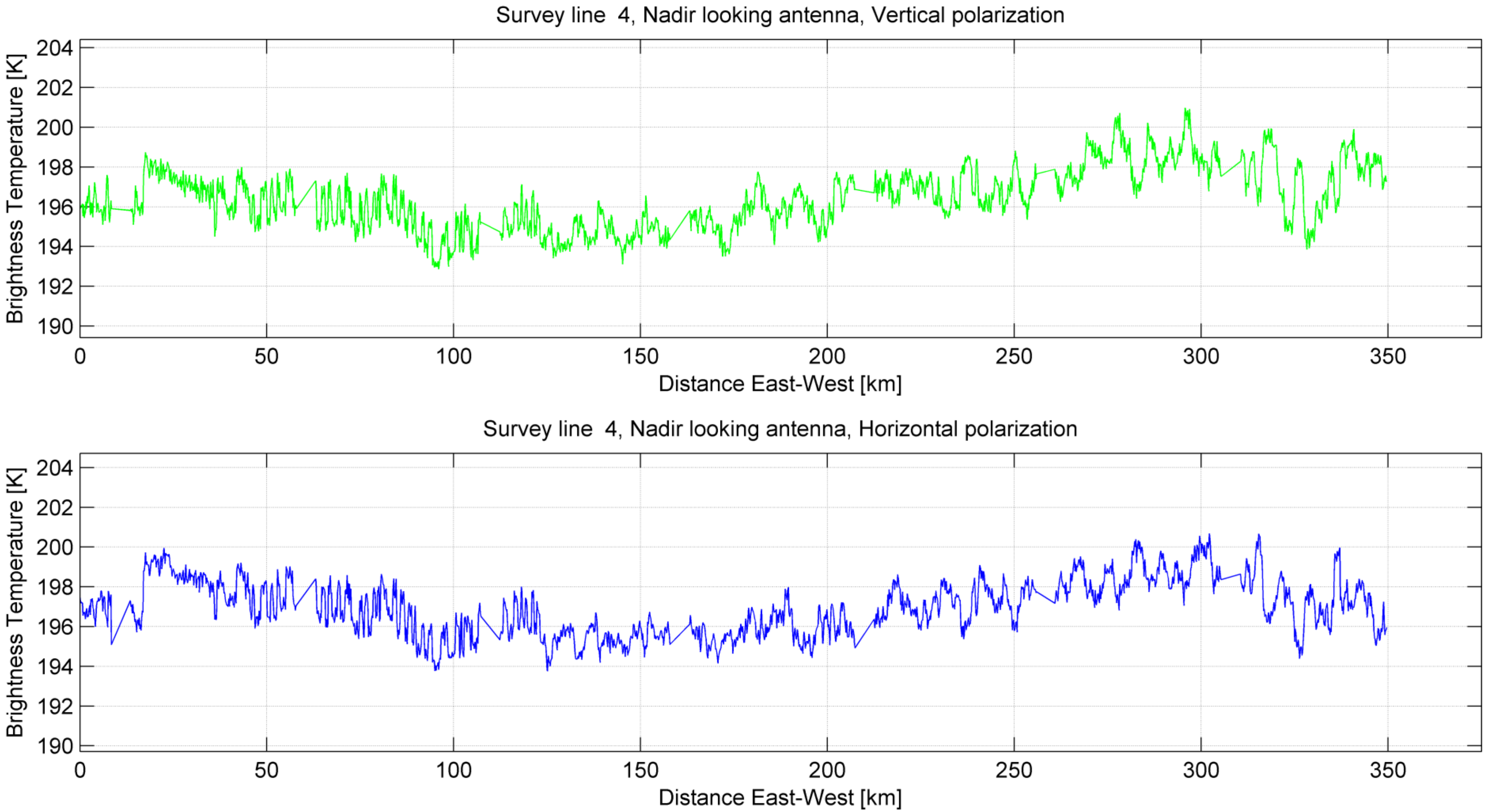


Figure 6.1.7: Survey line 4 profile: Nadir looking antenna.

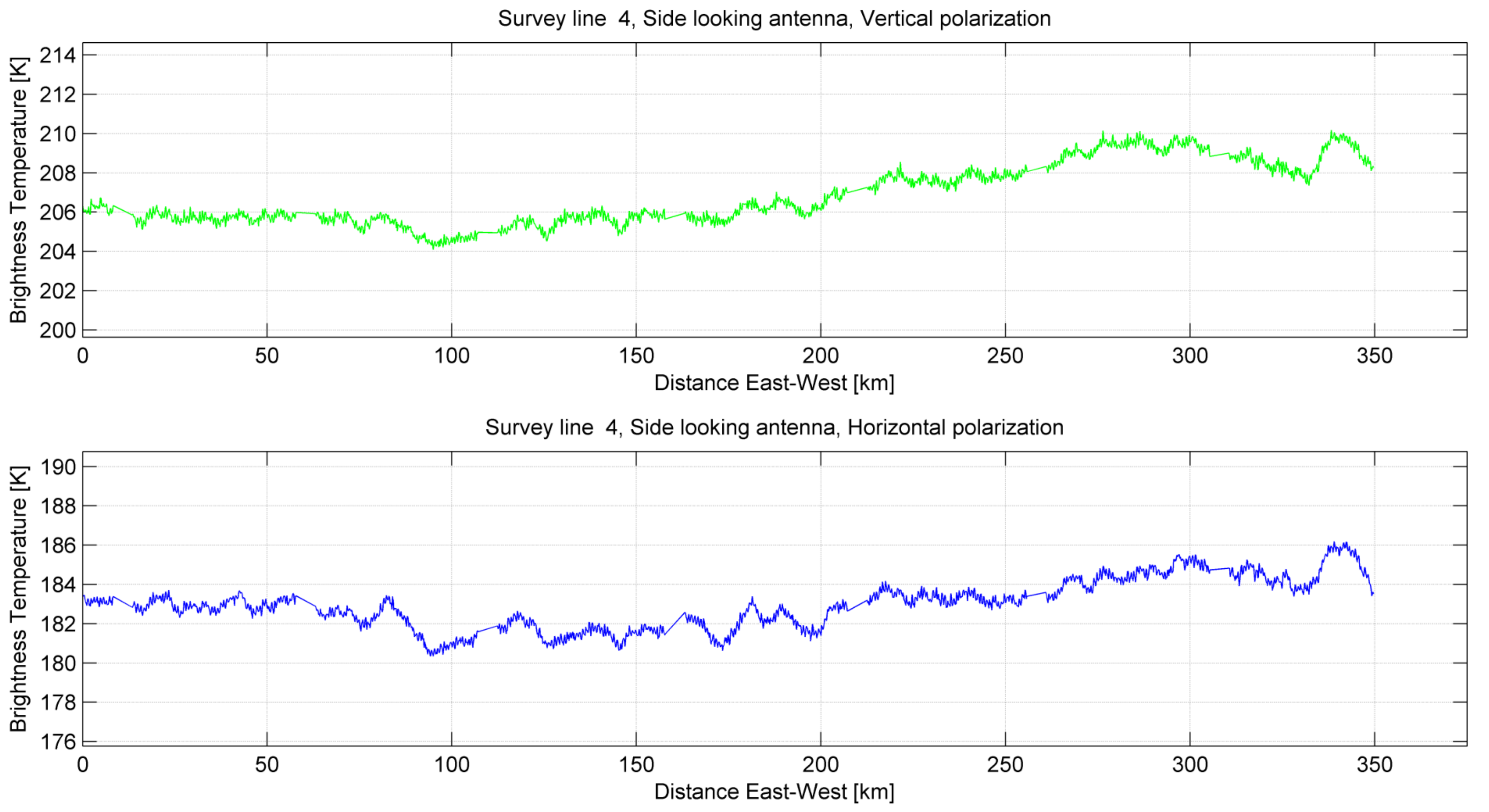


Figure 6.1.8: Survey line 4 profile: Side looking antenna.

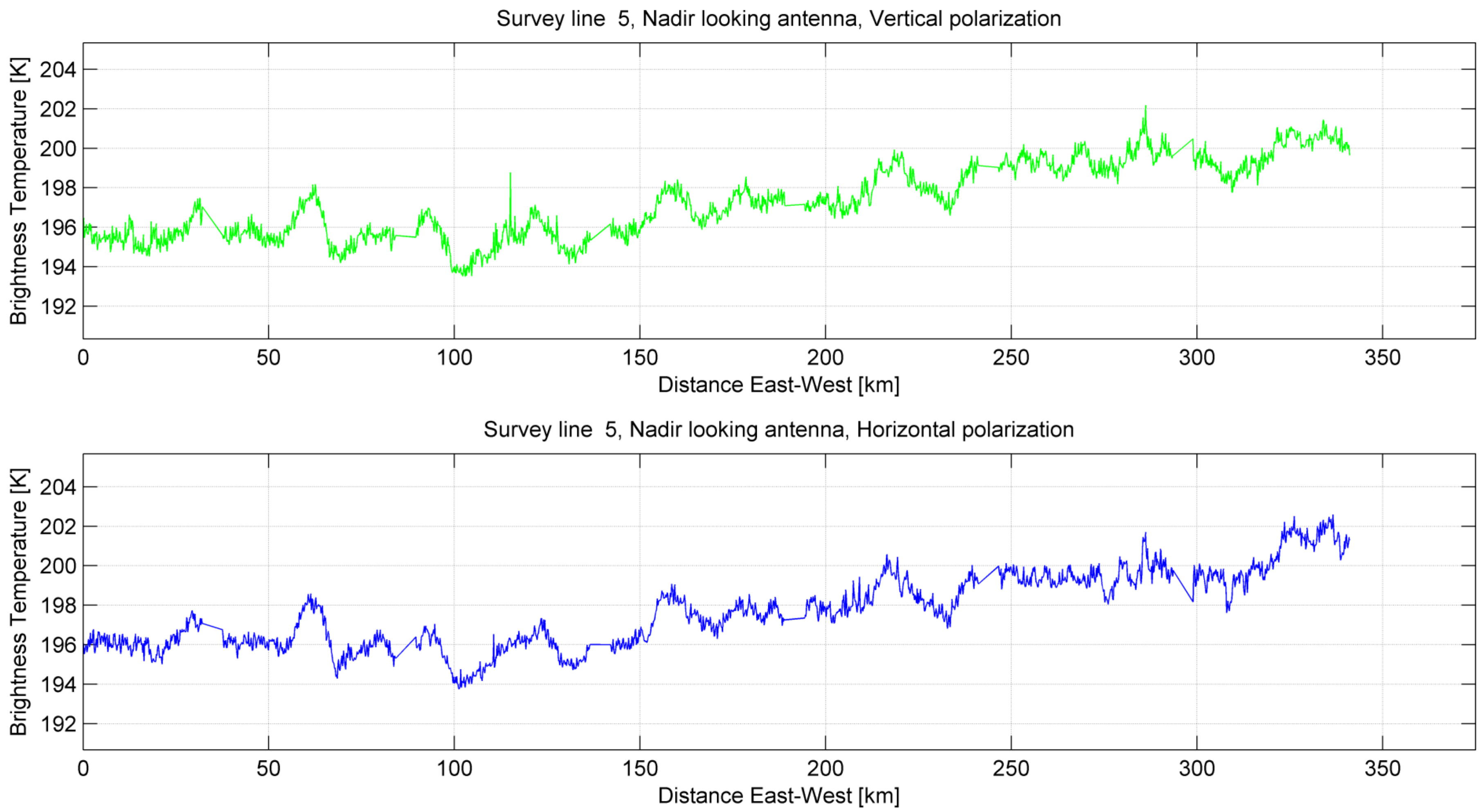


Figure 6.1.9: Survey line 5 profile: Nadir looking antenna.

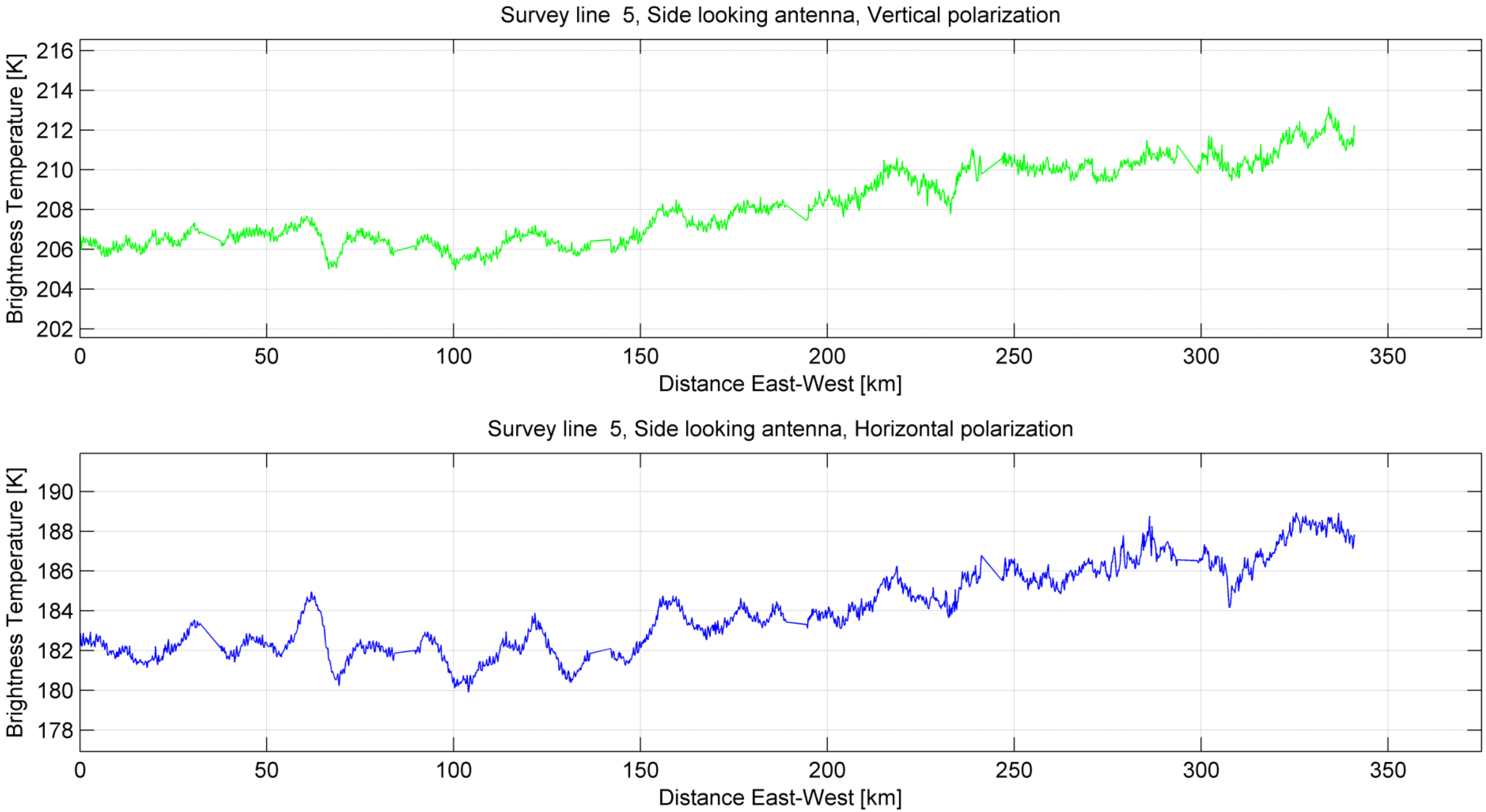


Figure 6.1.10: Survey line 5 profile: Side looking antenna.

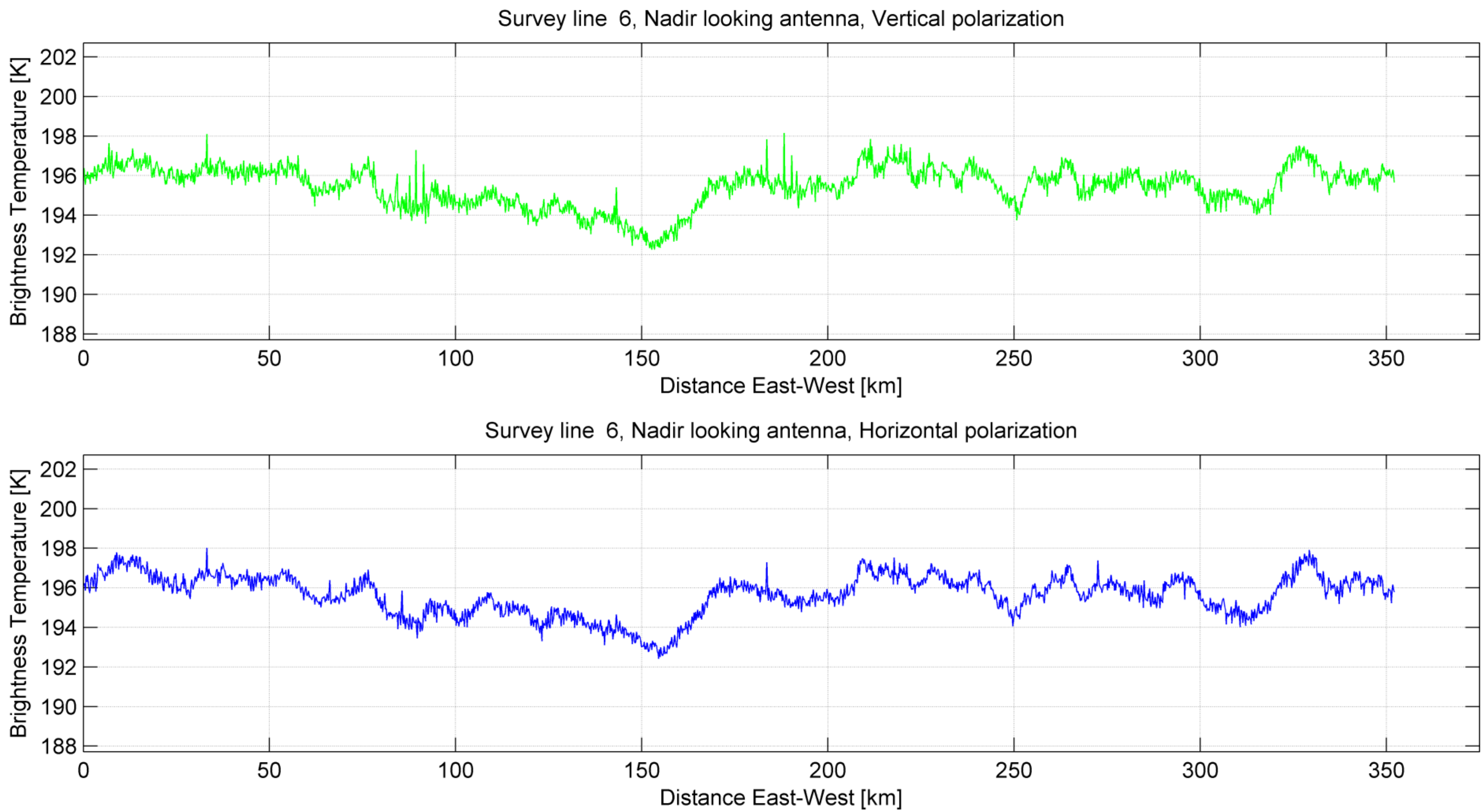


Figure 6.1.11: Survey line 6 profile: Nadir looking antenna.

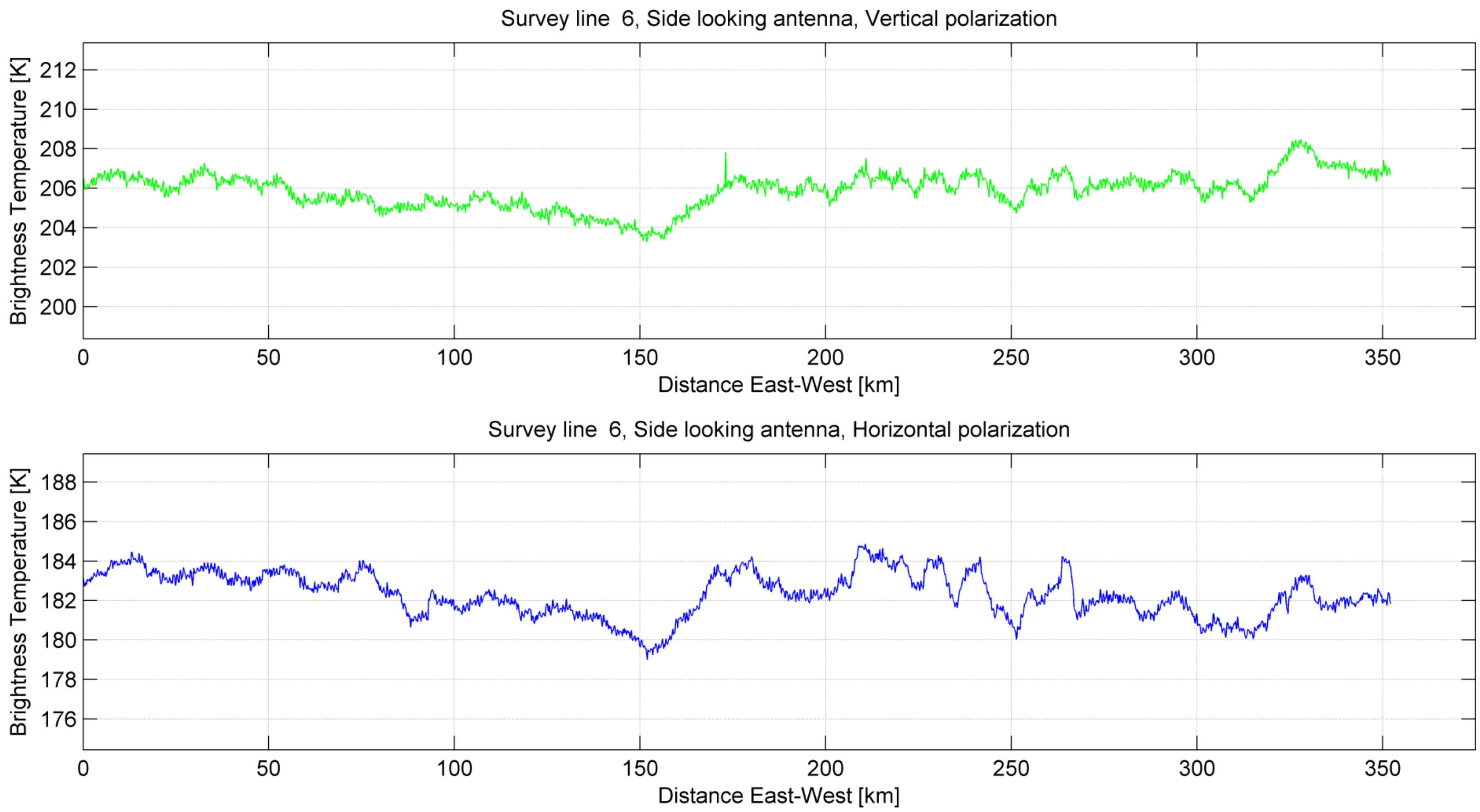


Figure 6.1.12: Survey line 6 profile: Side looking antenna.

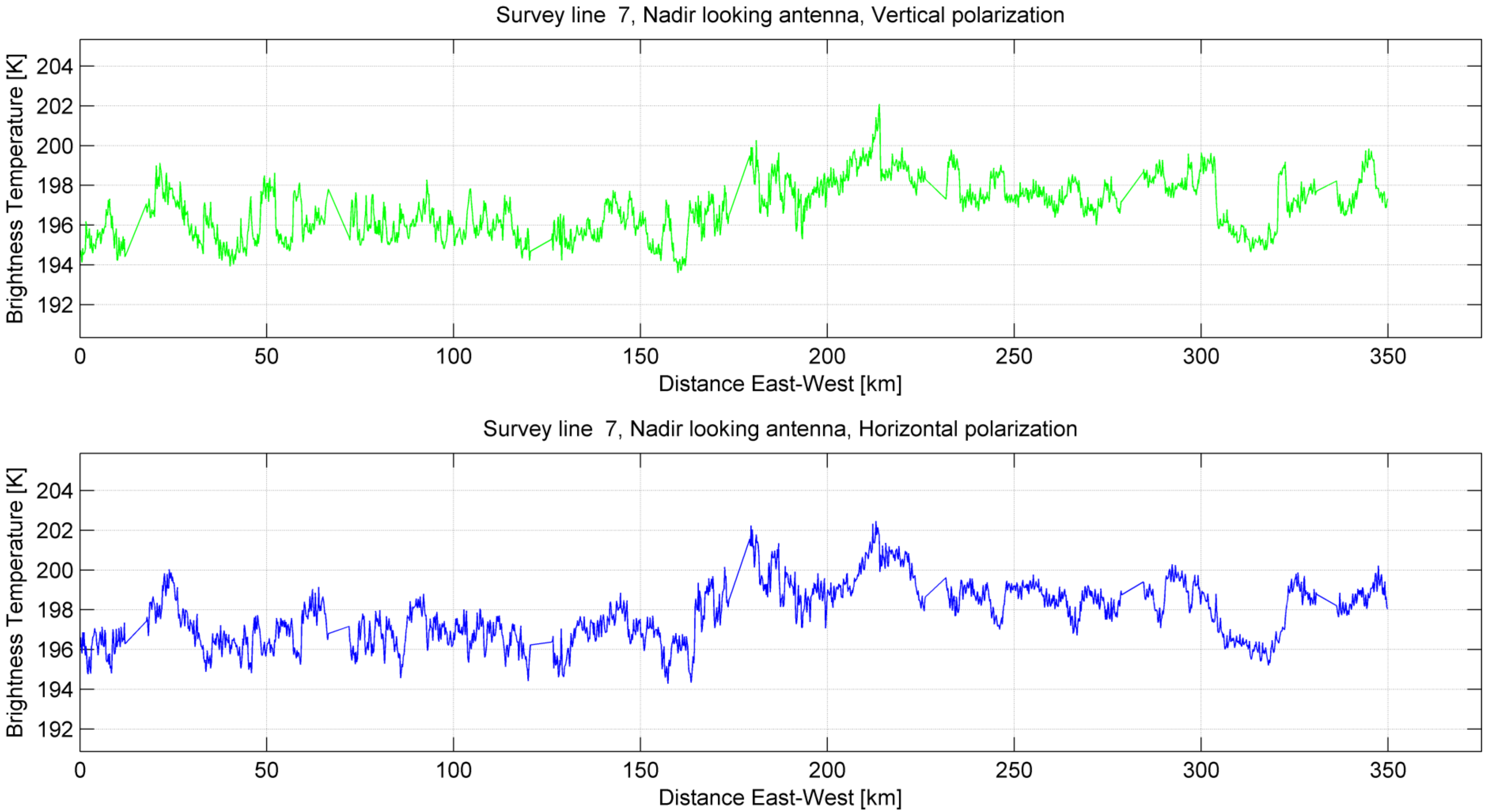


Figure 6.1.13: Survey line 7 profile: Nadir looking antenna.

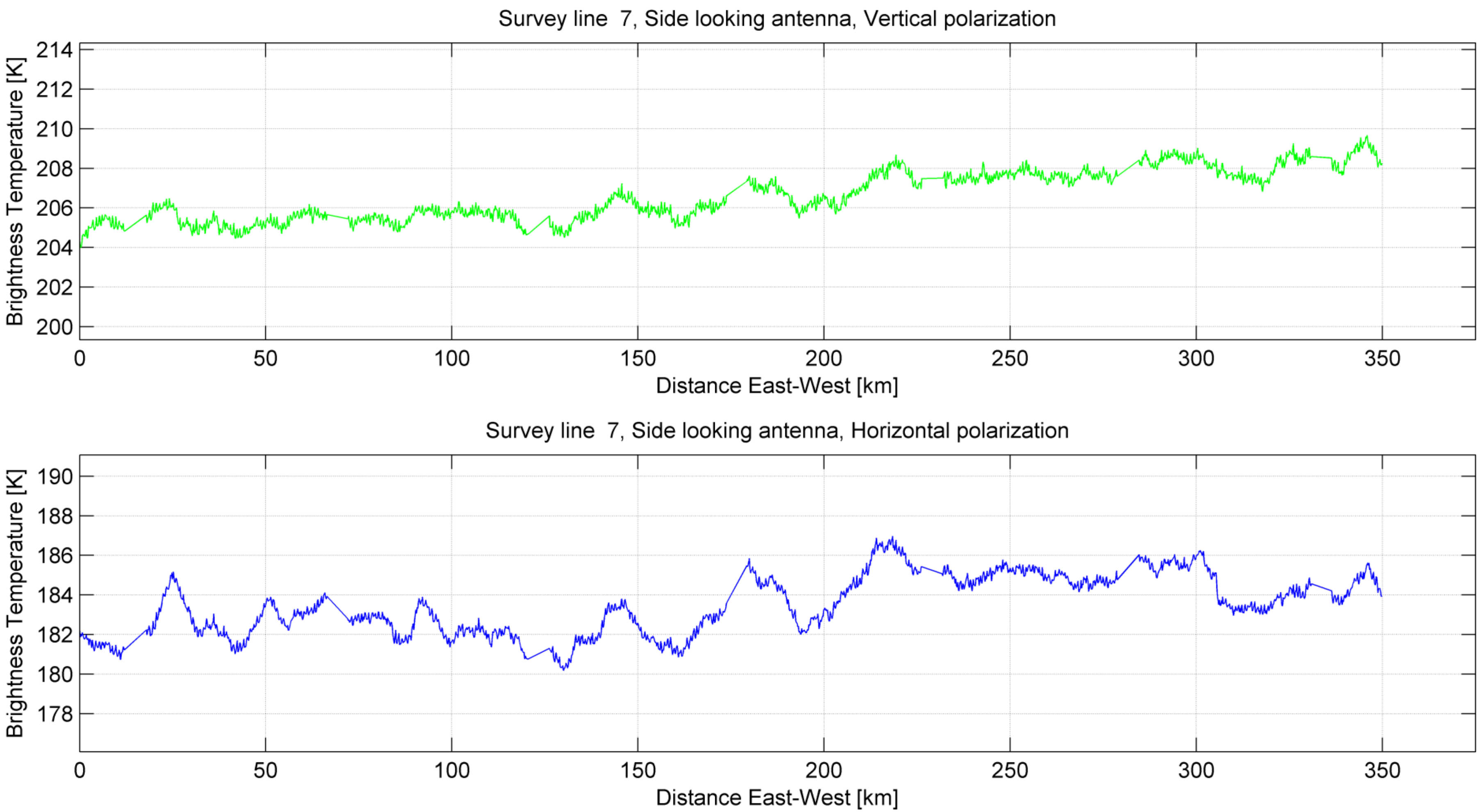


Figure 6.1.14: Survey line 7 profile: Side looking antenna.

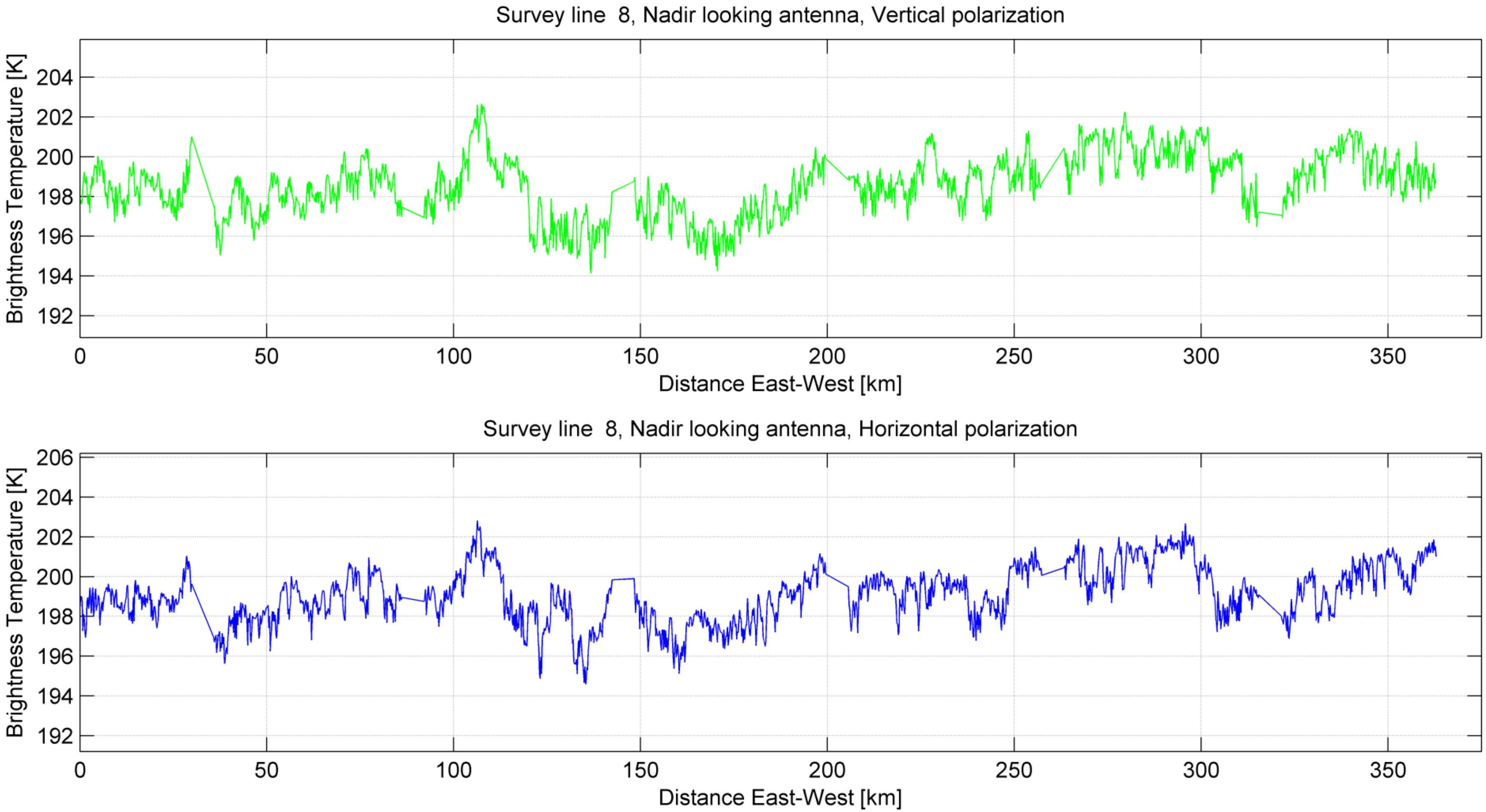


Figure 6.1.15: Survey line 8 profile: Nadir looking antenna.

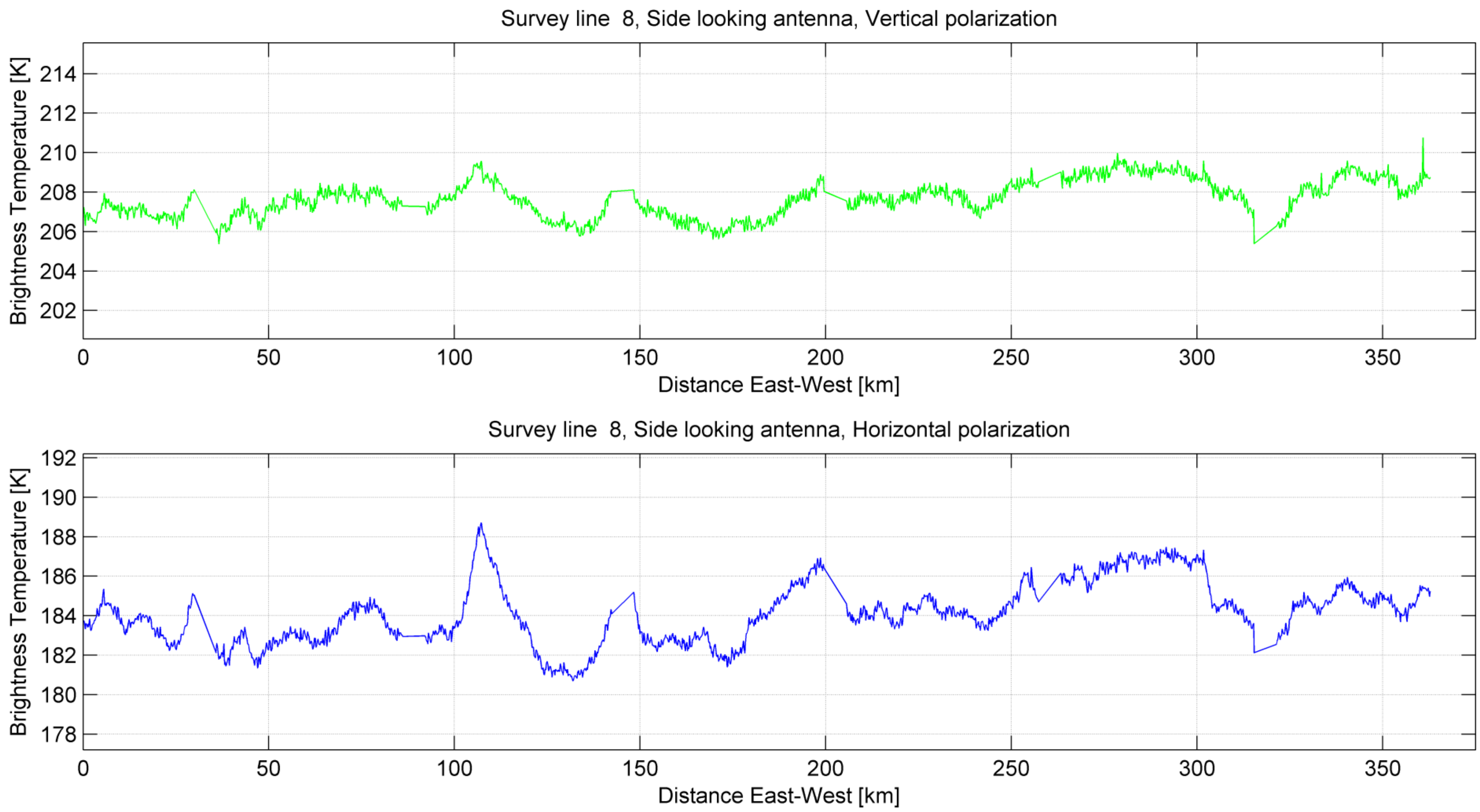


Figure 6.1.16: Survey line 8 profile: Side looking antenna.

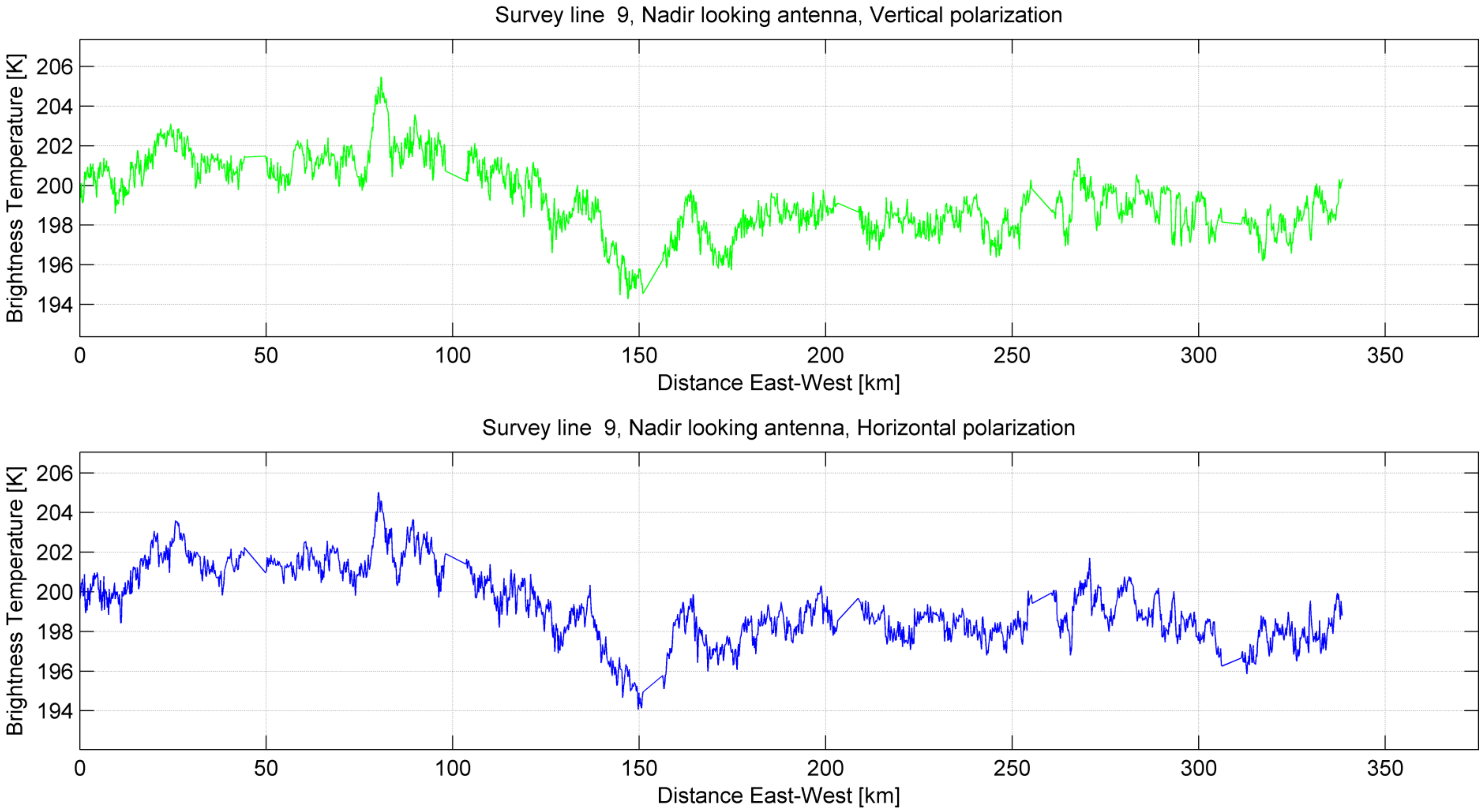


Figure 6.1.17: Survey line 9 profile: Nadir looking antenna.

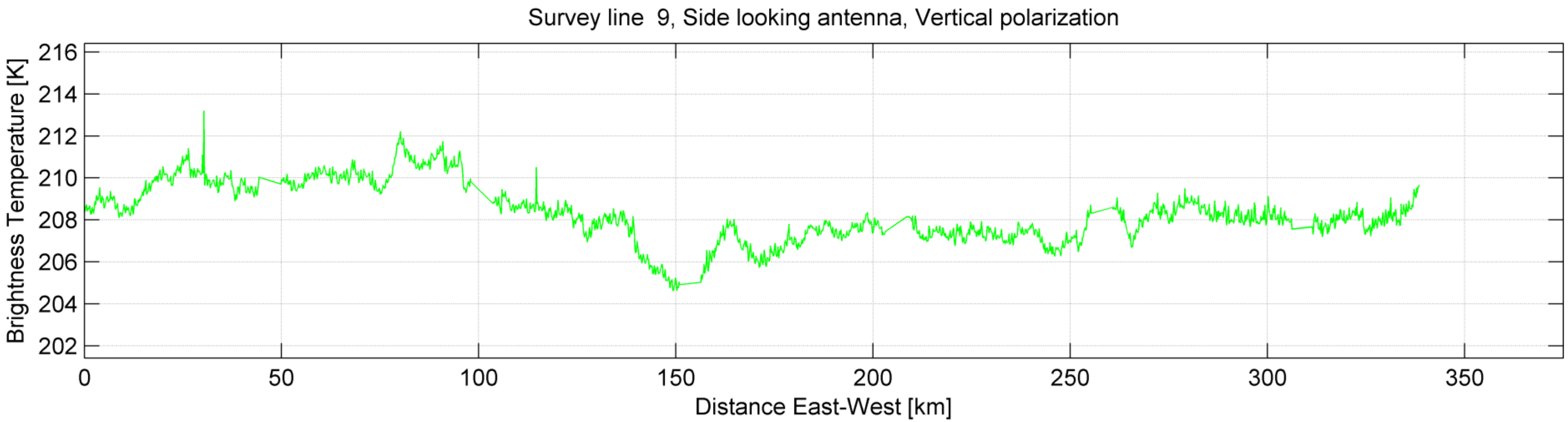


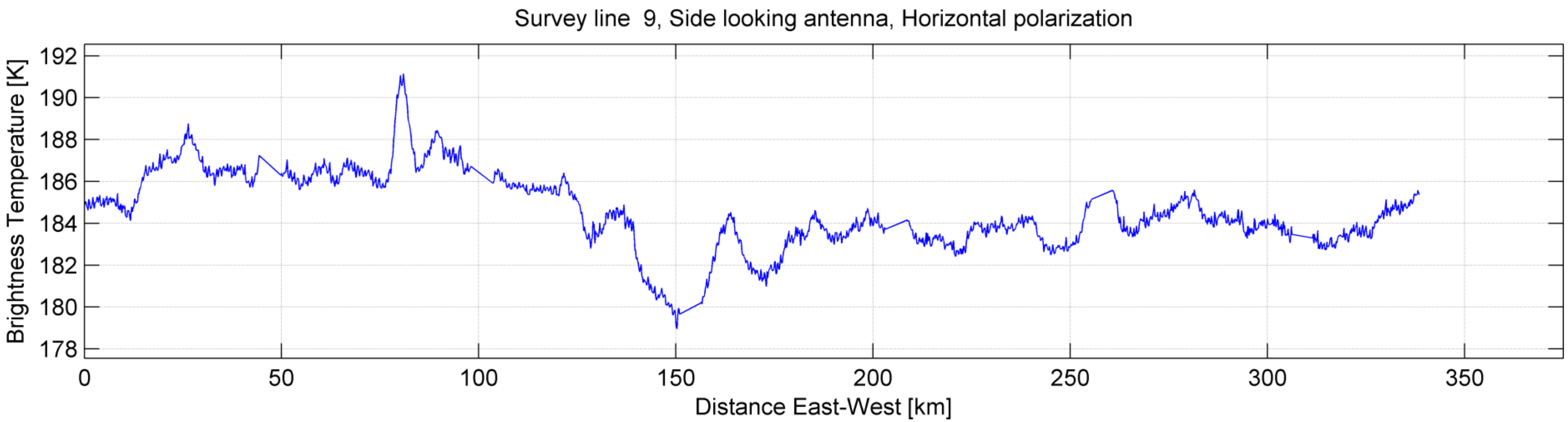


Figure 6.1.18: Survey line 9 profile: Side looking antenna.

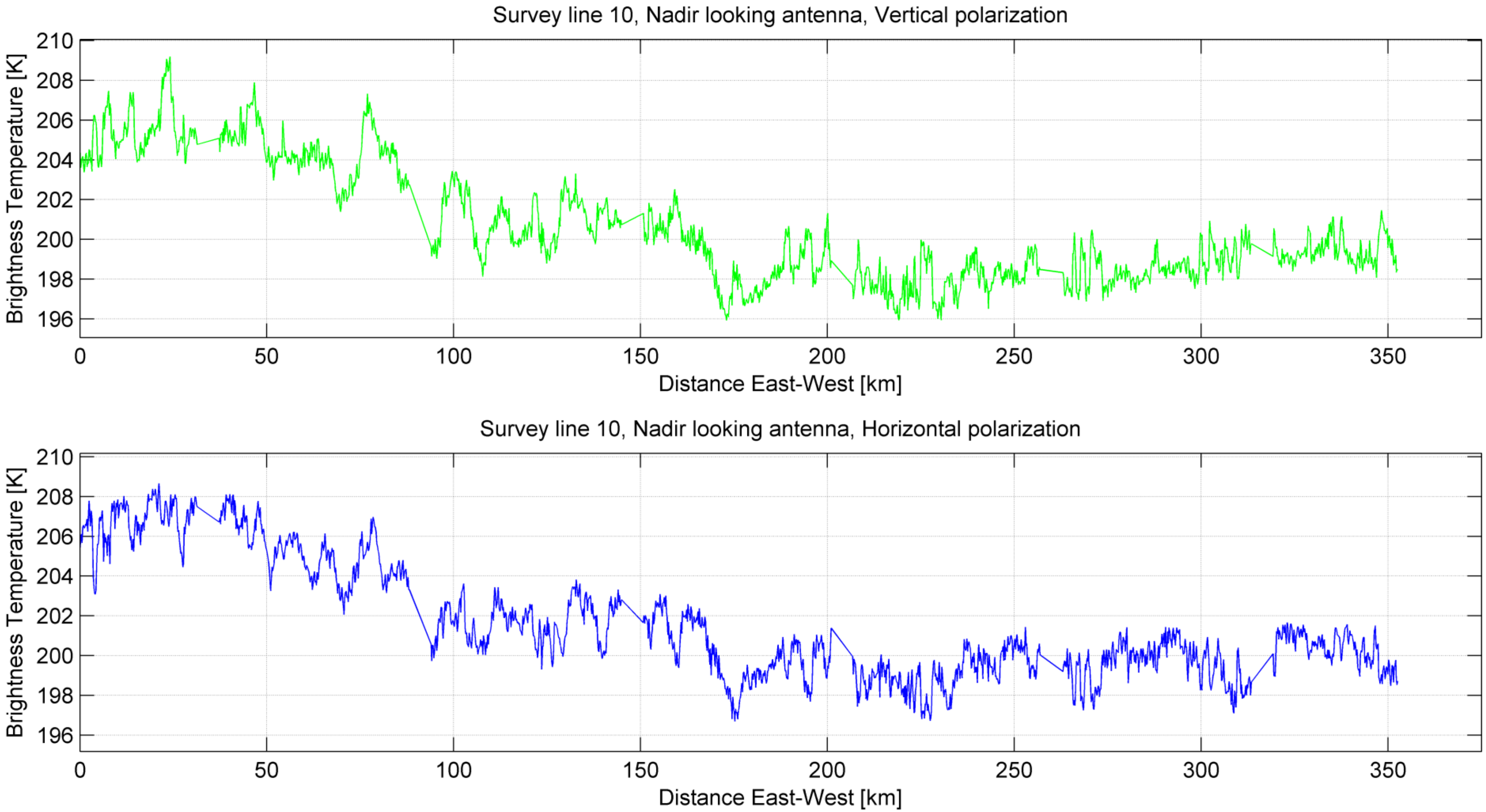


Figure 6.1.19: Survey line 10 profile: Nadir looking antenna.

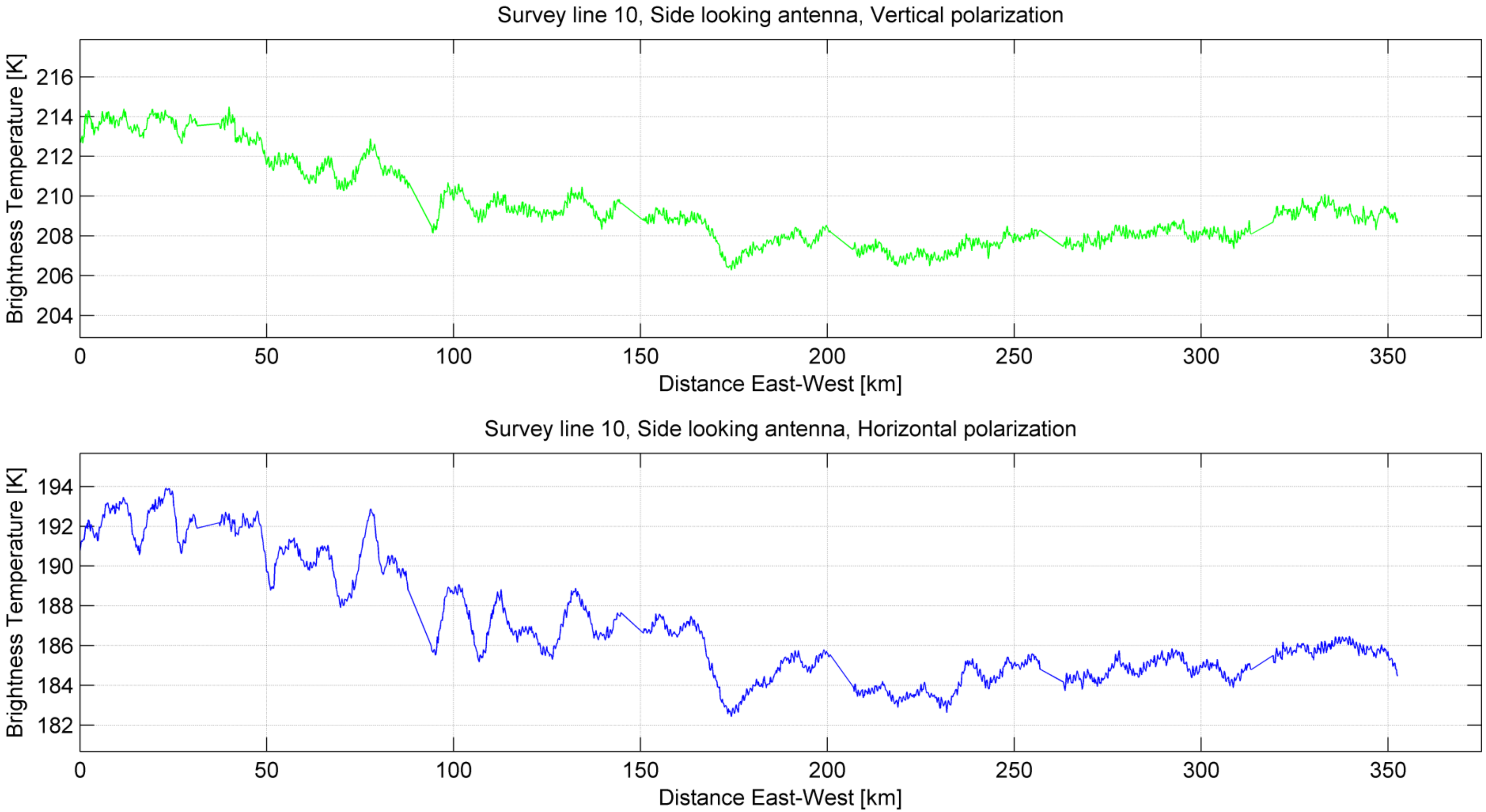


Figure 6.1.20: Survey line 10 profile: Side looking antenna.

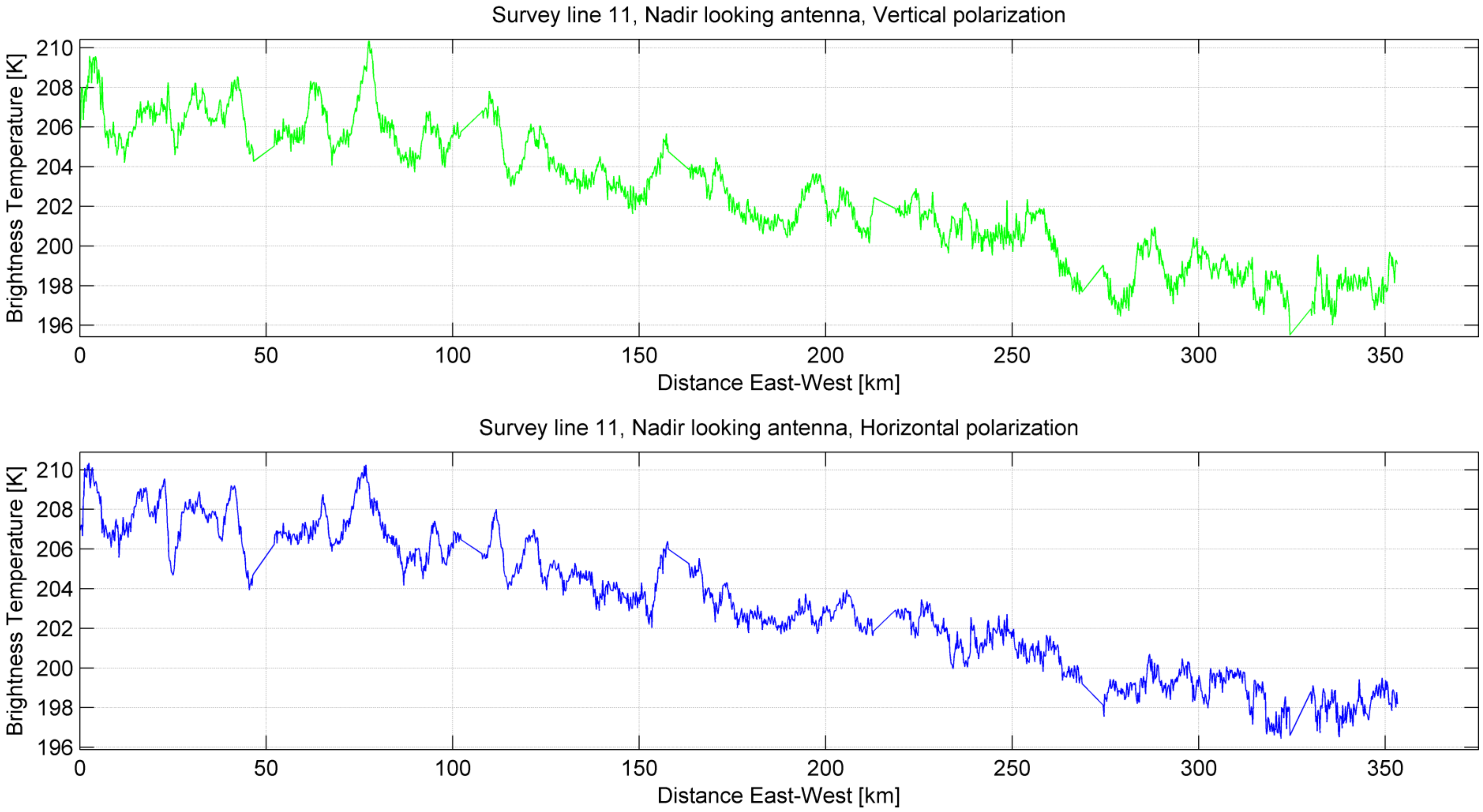


Figure 6.1.21: Survey line 11 profile: Nadir looking antenna.

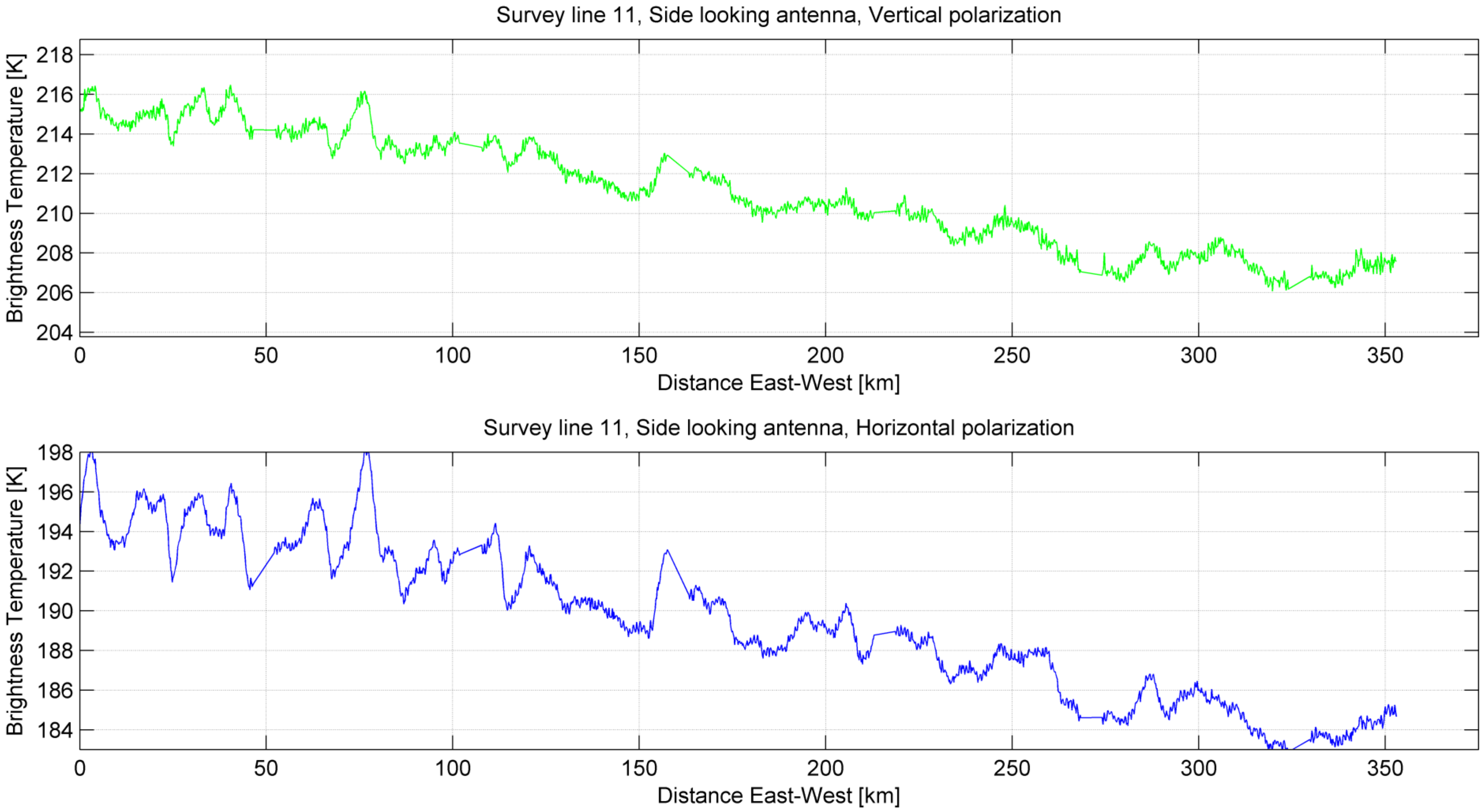


Figure 6.1.22: Survey line 11 profile: Side looking antenna.

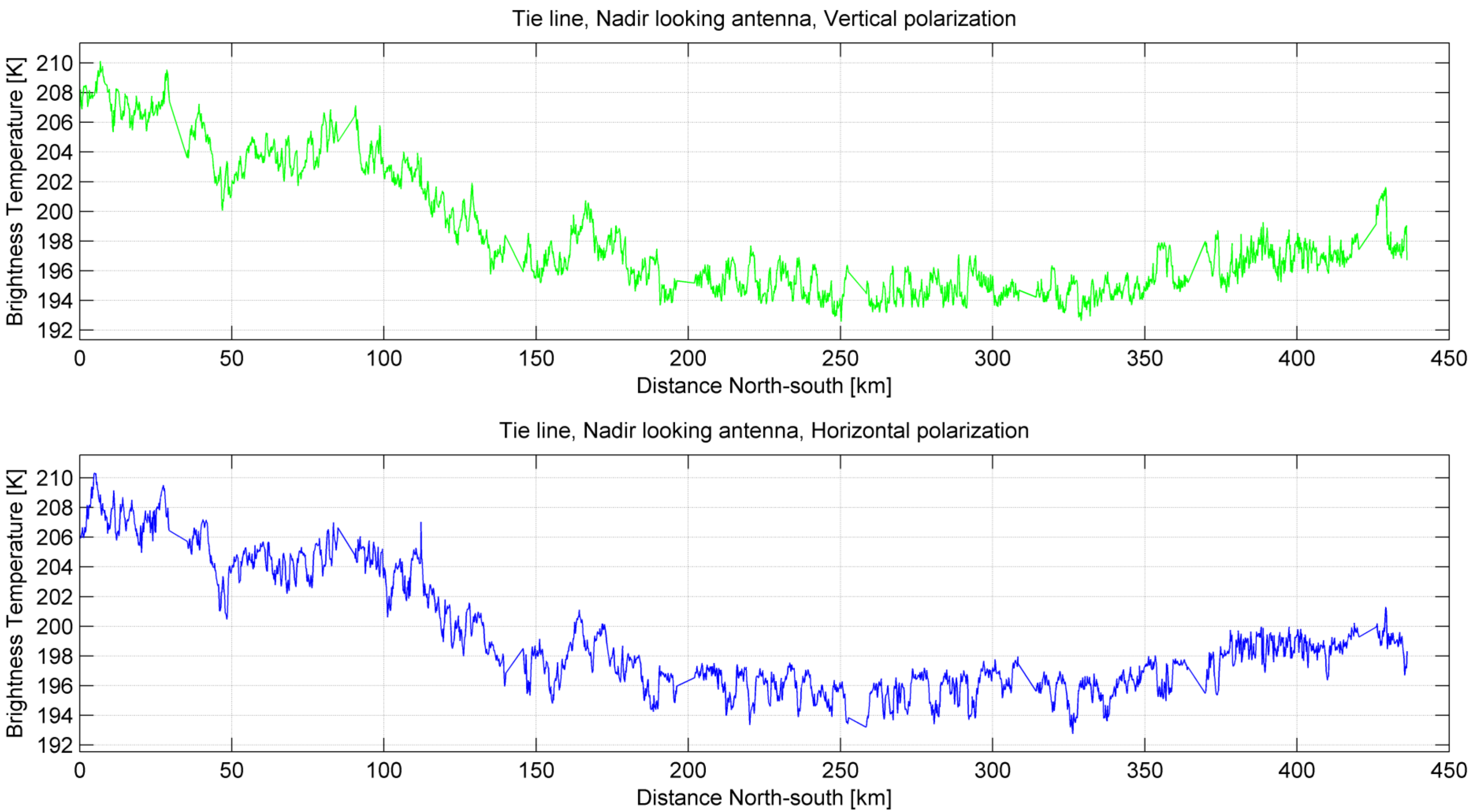


Figure 6.1.23: Tie profile: Nadir looking antenna.

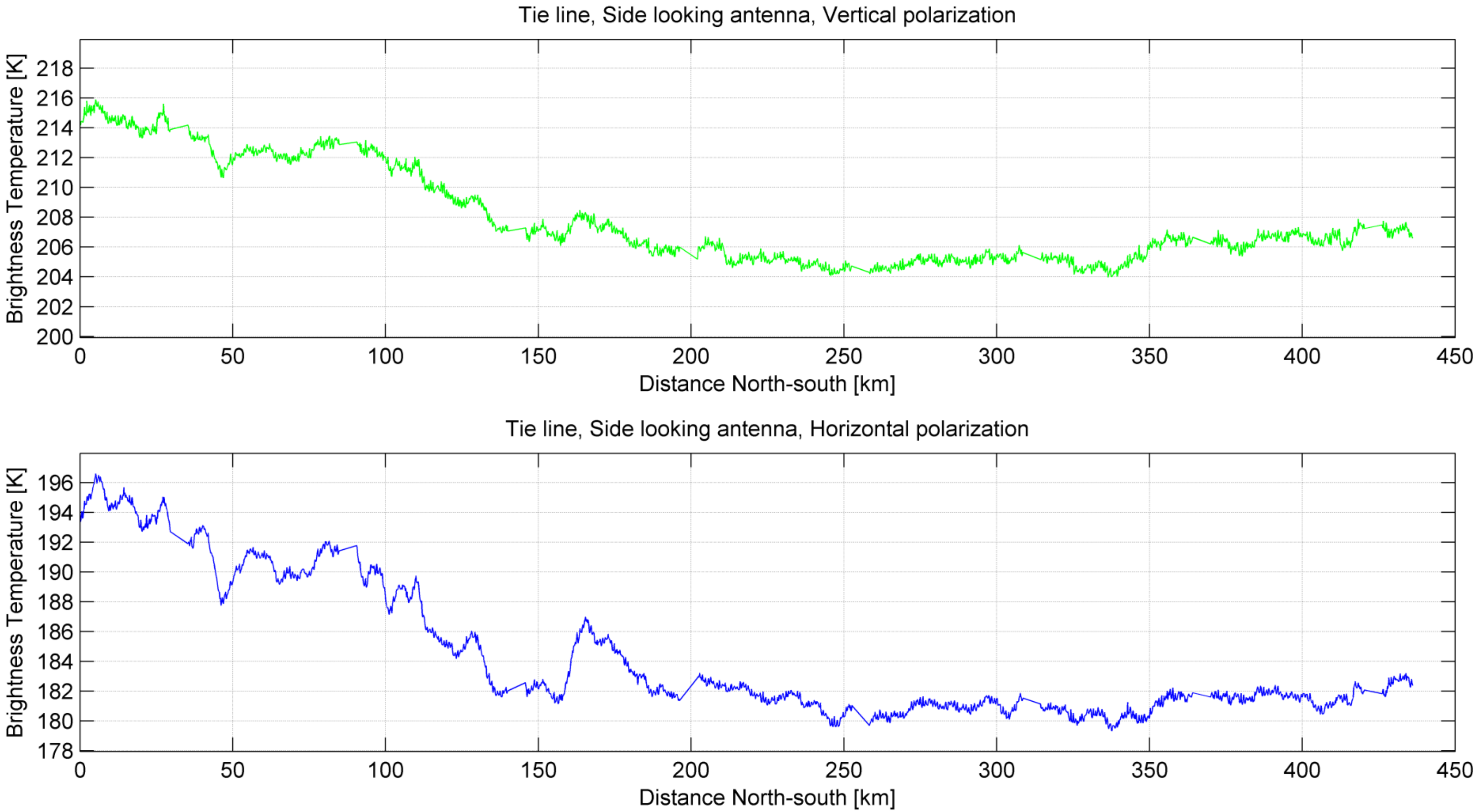


Figure 6.1.24: Tie profile: Side looking antenna.

.

## 6.2 Profiles Convoluted with SMOS and Aquarius Antenna Pattern replicas

In order to assess the influence of the inhomogeneities when observing the area with SMOS and Aquarius eyes, the profiles of the side looking antenna have been convolved with 43 km and 100 km 3dB beamwidth antenna pattern replicas. Since only SMOS is capable of observing the nadir return, profiles from the nadir looking antenna is not used for comparing simulated SMOS and Aquarius outputs.

The SMOS and Aquarius antenna pattern replicas used are Gaussian

$$D(x) = \exp(-\alpha x^2),$$

where D(x) is the along track antenna pattern and α is a width scaling parameter to obtain a specific 3 dB width of the antenna patterns (43 km for SMOS and 100 km for Aquarius). In order to have similar conditions for both antenna patterns with the limited length of the survey lines, the width of both antenna pattern replicas are truncated at a width of twice their respective 3dB widths. When convoluting these two antenna patterns with the survey lines the outermost 100 km at both ends of each survey line becomes invalid in the Aquarius case due to the 200 km width of the Aquarius antenna pattern replica. Hence, only the parts within 100 km of the ends of each survey line is shown and used for calculating the statistics. Figures 6.2.1 to 6.2.2 show some examples, while the statistics for all lines are provided in Table 6.2.1.

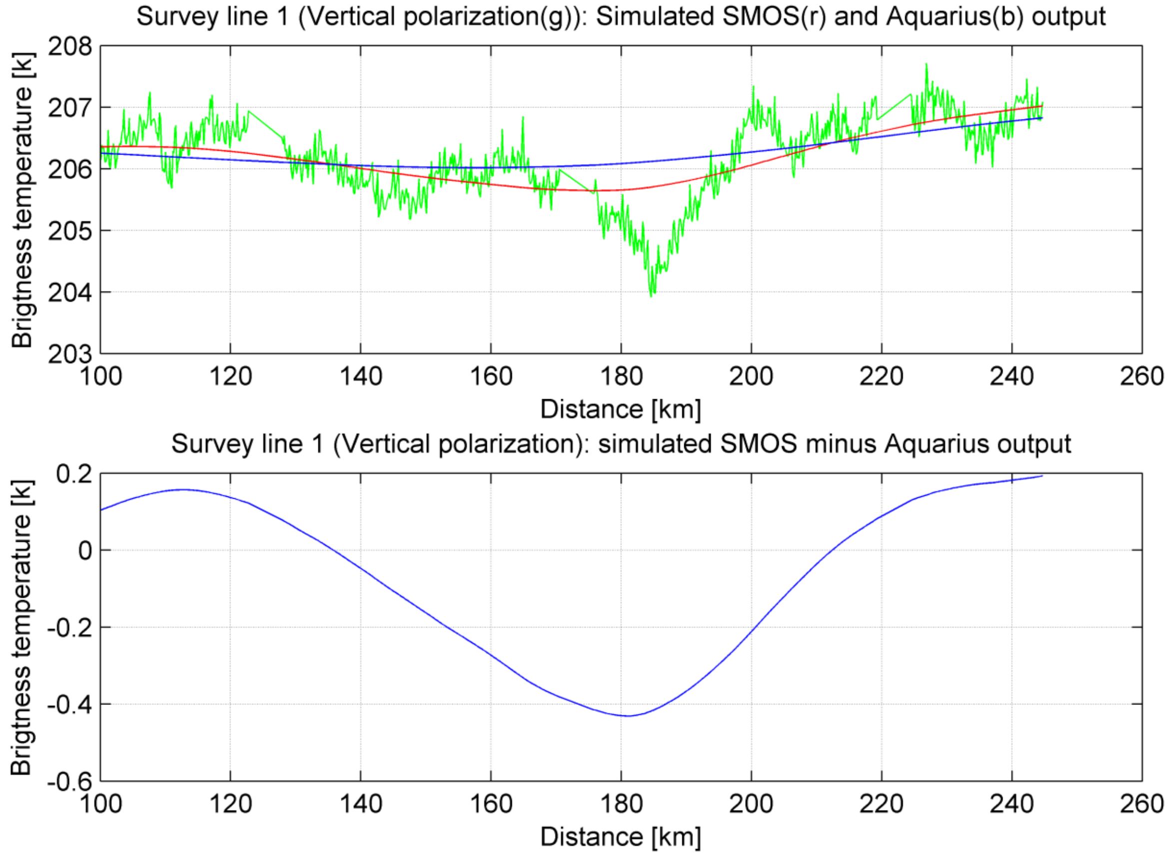


Figure 6.2.1: Central part of survey line 1. Top: EMIRAD-2 data (green), simulated SMOS data (red) and simulated Aquarius data (blue). Bottom: Difference between simulated SMOS data and simulated Aquarius Data.

In the simulated SMOS and Aquarius outputs it is clearly seen how wiggles and waves are integrated out and only large variations and tendencies are left. In Figure 6.2.1 it is seen how a small dip of 4 K in the brightness temperature along survey line 1 produces a 0.4 K difference between simulated SMOS and Aquarius measurements while the more substantial variations along survey line 9 shown in Figure 6.2.2 means that the difference between simulated SMOS and Aquarius measurement can vary more than 1 K. As similar results are seen in the other survey lines only these two examples are shown.

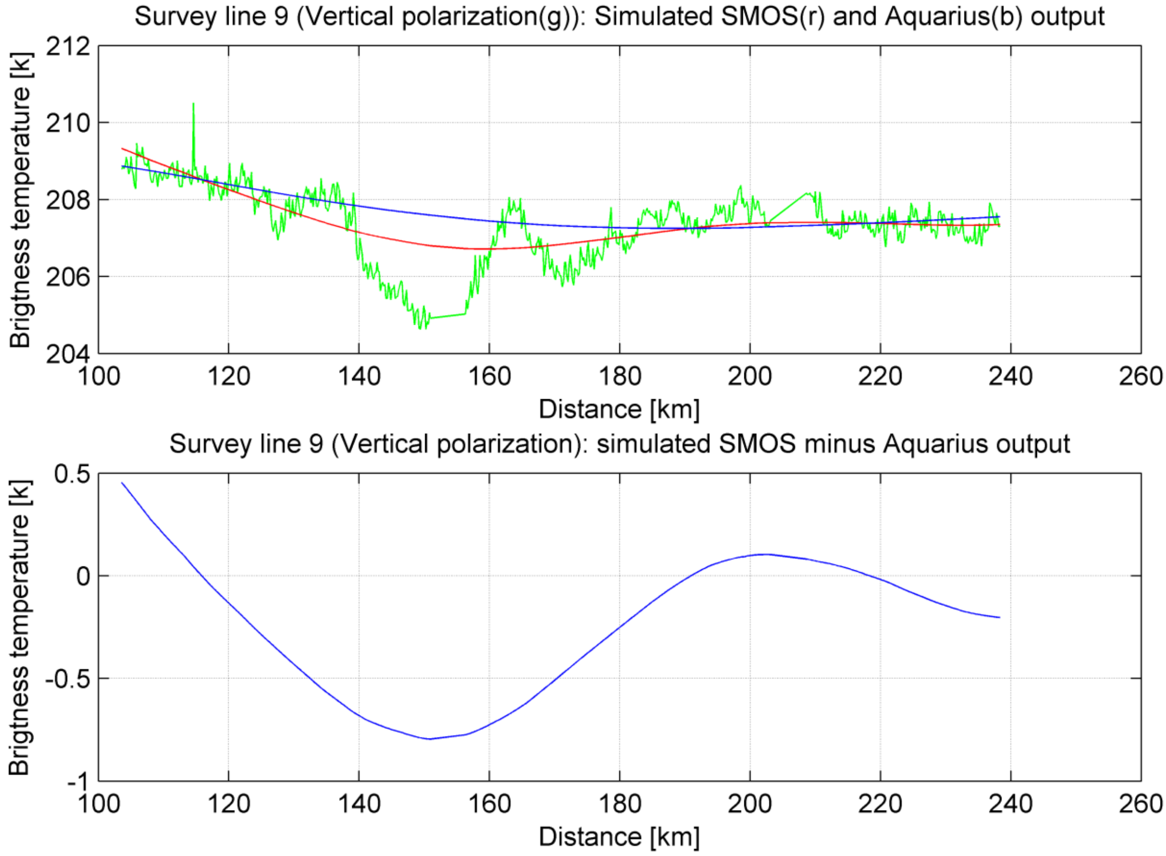


Figure 6.2.2: Central part of survey line 9. Top: EMIRAD-2 data (green), simulated SMOS data (red) and simulated Aquarius data (blue). Bottom: Difference between simulated SMOS data and simulated Aquarius Data.

The statistics in Table 6.2.1 cover all survey lines and show some interesting results. The most obvious result is that the mean value is negative for all except one insignificant value. This is very import because it shows that there will be a systematic difference between SMOS and Aquarius measurements at this site. The reason for this systematic difference is that this site to some extent is a local minimum and that Aquarius measures a higher brightness temperature at local minima due to its wider antenna 3dB width. The standard deviation, maximum and minimum values of these differences also show that there is significant spatial variation when comparing simulated SMOS and Aquarius results and that this must be taken into account if this area is used for calibrating SMOS and Aquarius.

| **Survey Line** | **Mean value** | | **Standard Deviation** | | **Max Difference** | | **Min Difference** | |
|---|---|---|---|---|---|---|---|---|
| | **V** | **H** | **V** | **H** | **V** | **H** | **V** | **H** |
| 1 | -0.075 | -0.153 | 0.209 | 0.216 | 0.194 | 0.211 | -0.431 | -0.474 |
| 2 | -0.114 | -0.116 | 0.198 | 0.188 | 0.114 | 0.254 | -0.463 | -0.441 |
| 3 | -0.162 | -0.261 | 0.195 | 0.154 | 0.079 | -0.032 | -0.504 | -0.550 |
| 4 | -0.120 | -0.146 | 0.109 | 0.141 | 0.062 | 0.111 | -0.340 | -0.326 |
| 5 | -0.089 | -0.135 | 0.218 | 0.206 | 0.190 | 0.076 | -0.400 | -0.478 |
| 6 | -0.056 | -0.008 | 0.302 | 0.484 | 0.342 | 0.654 | -0.579 | -0.767 |
| 7 | -0.032 | -0.057 | 0.112 | 0.393 | 0.172 | 0.540 | -0.162 | -0.545 |
| 8 | -0.088 | -0.122 | 0.236 | 0.368 | 0.395 | 0.642 | -0.450 | -0.755 |
| 9 | -0.238 | -0.265 | 0.317 | 0.489 | 0.455 | 0.796 | -0.795 | -1.145 |
| 10 | -0.204 | -0.285 | 0.133 | 0.217 | 0.091 | 0.186 | -0.359 | -0.550 |
| 11 | 0.004 | -0.020 | 0.064 | 0.146 | 0.149 | 0.197 | -0.086 | -0.229 |

*Table 6.2.1: Mean value, standard deviation, maximum and minimum value of difference between simulated SMOS data and simulated Aquarius data.*

## 6.3 Analysis of Details

Figure 6.3.1 and Figure 6.3.2 zoom in on side looking antenna at the beginning of line 5 with full resolution in order to reveal details. The side looking antenna footprint is approximately 500 m. This footprint size is illustrated in the plots by the dashed line at the bottom of each plot. Each dash (black or white) is equal to the footprint size. The radiometric resolution is 0.1 K for the 1 sec. integration time used here. This produces the typical 0.3 K p-p appearance of the brightness temperature in the plots.

Thus we see a mixture of ΔT and small resolved wiggles in the plots. Also, we see somewhat larger, certainly resolved wiggles/waves. In the full range profiles shown in section 6.1 is clearly seen larger variations as well as tendencies from beginning to end of the profiles (i.e. over some 350 km.

In conclusion: significant brightness temperature variations are observed over a range of scales ranging from a few km to 300 km.

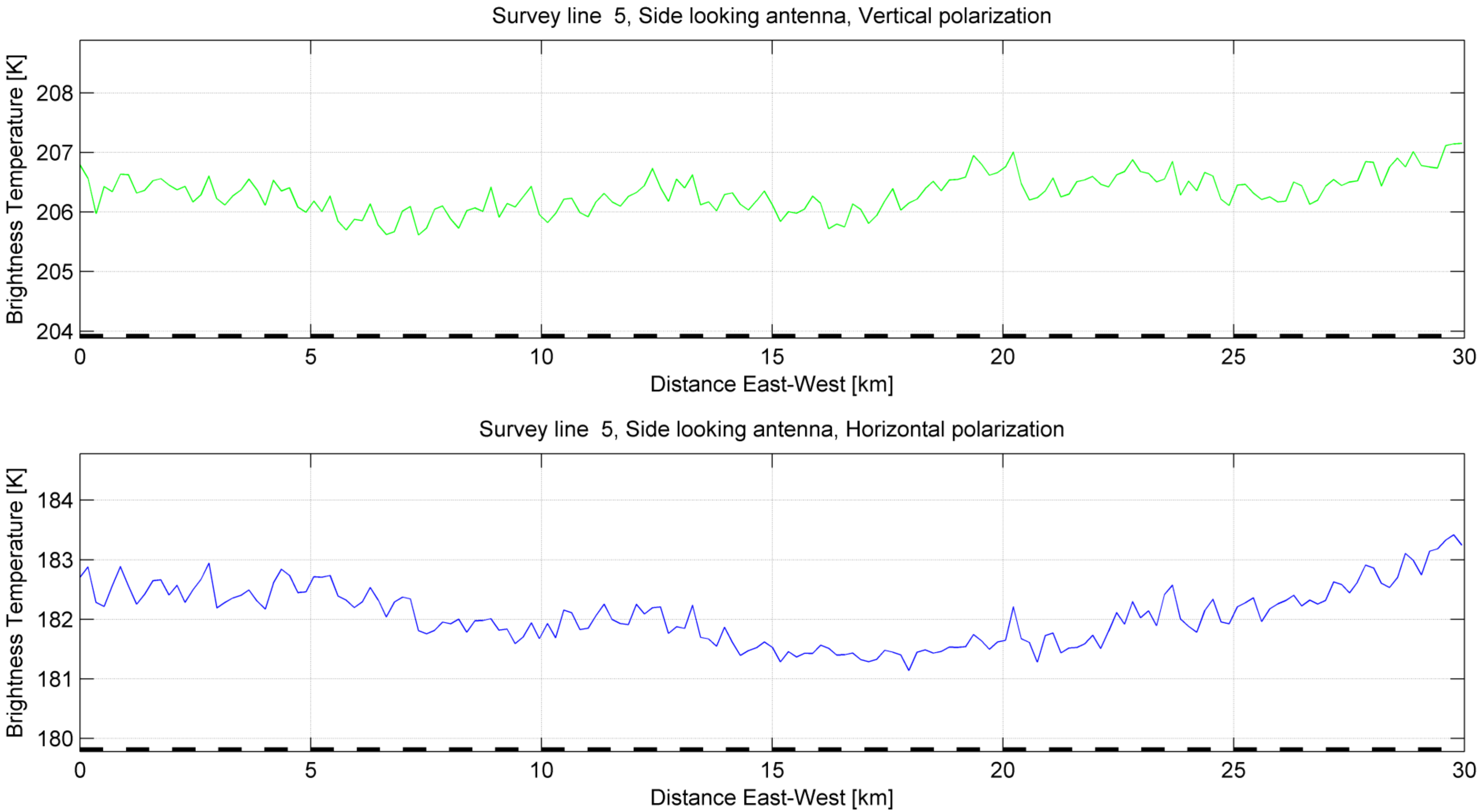


Figure 6.3.1: Survey line 5 profile zoom at beginning of line: Side looking antenna.

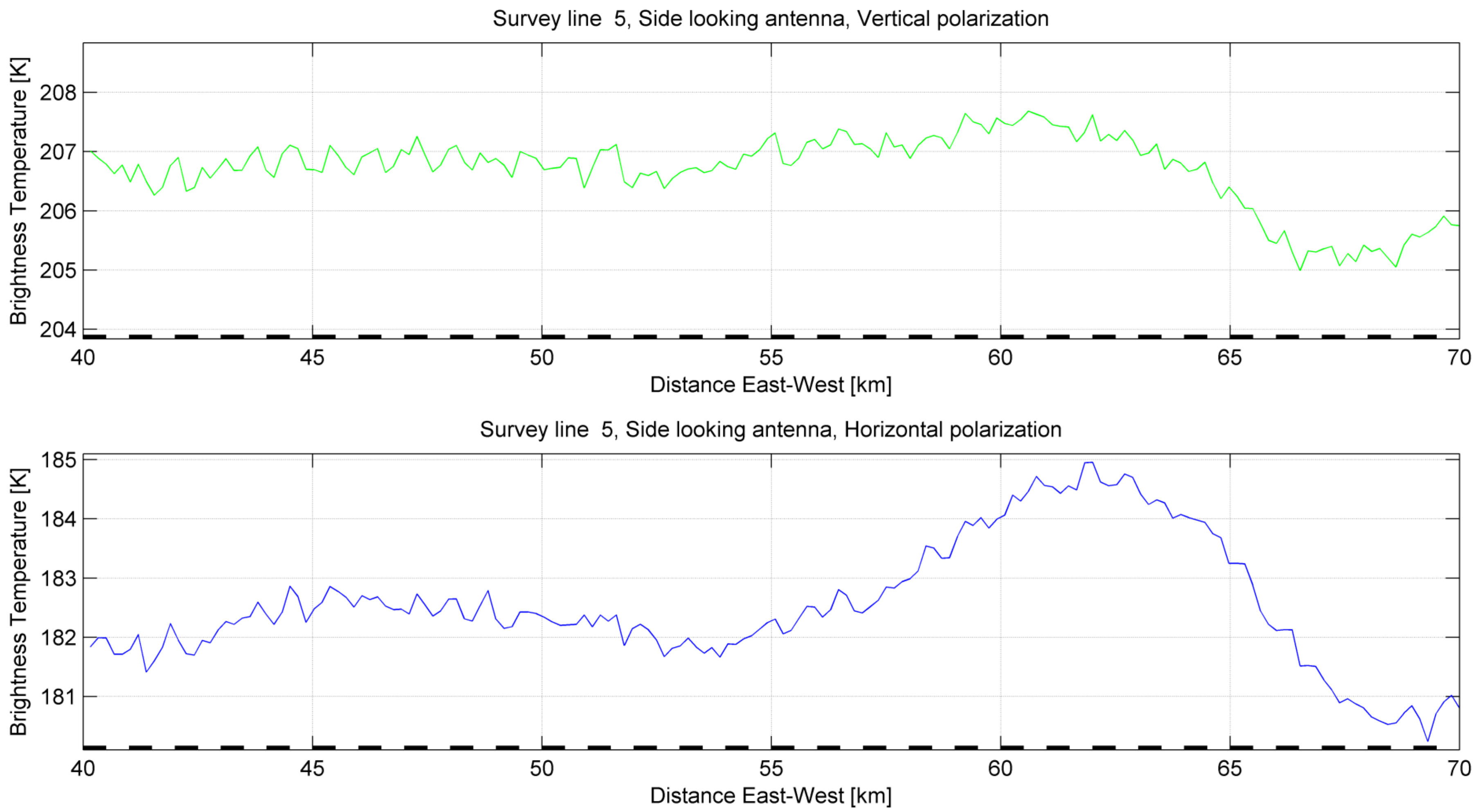


Figure 6.3.2: Survey line 5 profile zoom at beginning of line: Side looking antenna.

## 6.4 Crossing Point Analysis

The tie line crosses the 11 survey lines and it is thus possible to compare the measurements at the 11 crossing points. The samples of the tie line are not located exactly on the 11 survey lines and vice versa, wherefore the brightness temperatures at the 11 crossing point are found using linear interpolation between the samples nearest to the crossing points for both survey lines and tie line. The differences between tie line measurements and survey line measurement are shown in Figure 6.4.1 and the statistics are given in Table 6.4.1.

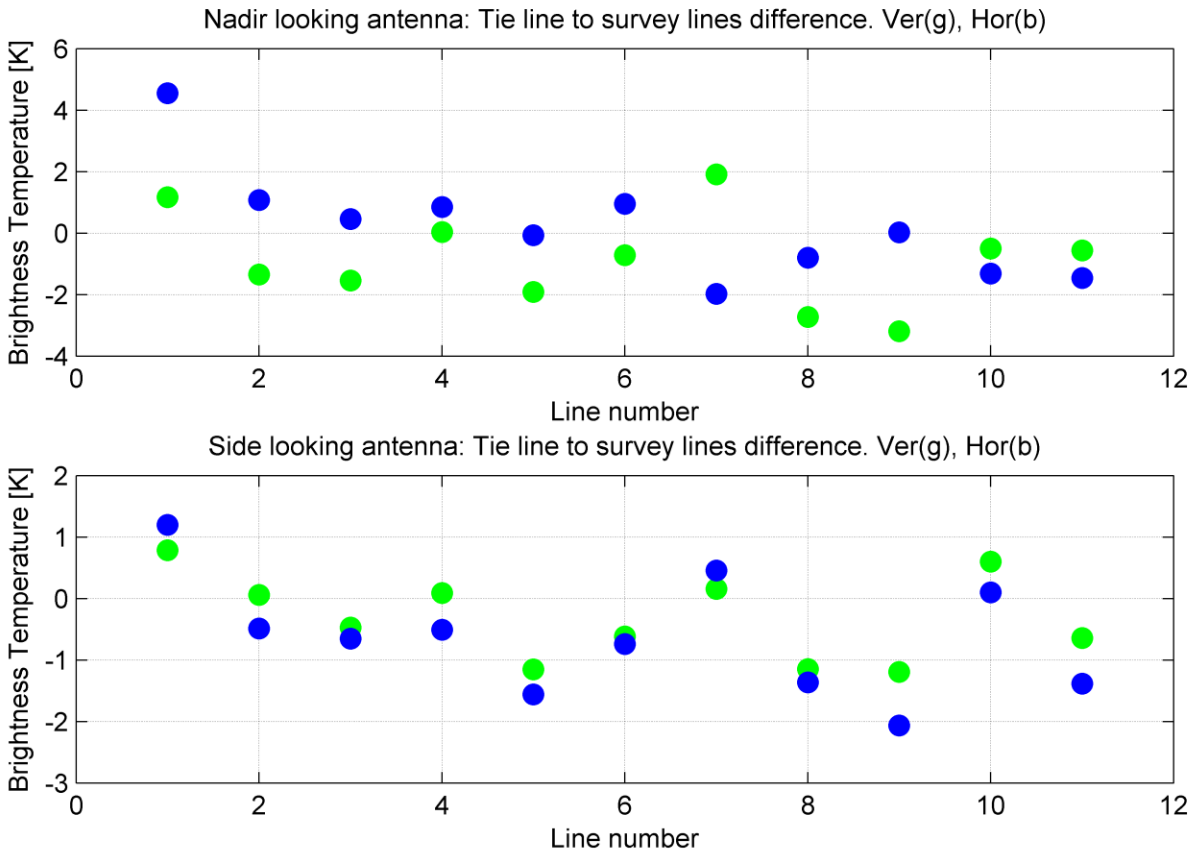


Figure 6.4.1: Difference between Tie line and Survey line measurements.

There is no apparent explanation for the variation between the survey lines and the tie line brightness temperatures being somewhat higher than expected due to ΔT. One could look for a temporal connection. The survey lines and the tie line was recorded in pairs: (1,4), (7,10), (11, Tie), (2,3), (5,6) and (8,9). However, it is difficult to observe any systematic dependence on simultaneous flown data.

| Survey line | Latitude [deg.] | Longitude [deg.] | Nadir looking antenna [K] | | Side looking antenna [K] | |
|---|---|---|---|---|---|---|
| | | | V-pol | H-Pol | V-Pol | H-Pol |
| 1 | -76.105555 | 117.057070 | 1.173 | 4.549 | 0.788 | 1.196 |
| 2 | -75.780422 | 117.162046 | -1.346 | 1.080 | 0.061 | -0.485 |
| 3 | -75.451367 | 117.267584 | -1.546 | 0.455 | -0.470 | -0.653 |
| 4 | -75.129265 | 117.353950 | 0.036 | 0.850 | 0.089 | -0.509 |
| 5 | -74.784391 | 117.449342 | -1.911 | -0.070 | -1.151 | -1.561 |
| 6 | -74.474964 | 117.531267 | -0.717 | 0.948 | -0.616 | -0.739 |
| 7 | -74.149835 | 117.622192 | 1.914 | -1.977 | 0.159 | 0.456 |
| 8 | -73.822919 | 117.699532 | -2.731 | -0.795 | -1.149 | -1.365 |
| 9 | -73.493612 | 117.777563 | -3.190 | 0.030 | -1.194 | -2.062 |
| 10 | -73.169436 | 117.857003 | -0.501 | -1.314 | 0.601 | 0.102 |
| 11 | -72.837197 | 117.929868 | -0.558 | -1.455 | -0.642 | -1.386 |
| Mean value for all crossings | | | -0.852 | 0.209 | -0.320 | 0.637 |
| Standard deviation for all crossings | | | 1.537 | 1.778 | 0.705 | 0.955 |

*Table 6.4.1: Survey lines to Tie line brightness temperature difference at crossing point.*

The star pattern flight lines all passes over the same point and it is thus possible to compare the brightness temperatures of their crossing point as a function of azimuth angle. The deviation of each star line from the mean values of all star lines are shown in Figure 6.4.2 and the statistics are provided in Table 6.4.2. As the azimuth angle of the nadir looking antenna is undefined, the azimuth angle of the side looking antenna is used on the abscissa for both antennas. As the star lines do not pass exactly over the American Tower, the sample nearest to the American Tower on each line has been used in this case.

Again a significant variation is seen without any obvious explanation. The only systematic result is that the standard deviation is smaller for the star lines which could indicate that the larger temporal spacing of the survey lines and tie line adds some variation to the data, but this is not supported by looking at survey/tie lines recorded on the same flight.

The mean value of the side looking antenna brightness temperature for all star lines at the crossing points are provided in the bottom of Table 6.4.2: $T_{BV}$ = 210.3 K and $T_{BH}$ = 186.8 K. This compares well with the values from the DOMEX incidence angle (45°) brightness temperatures shown in Figure 3.9.1.

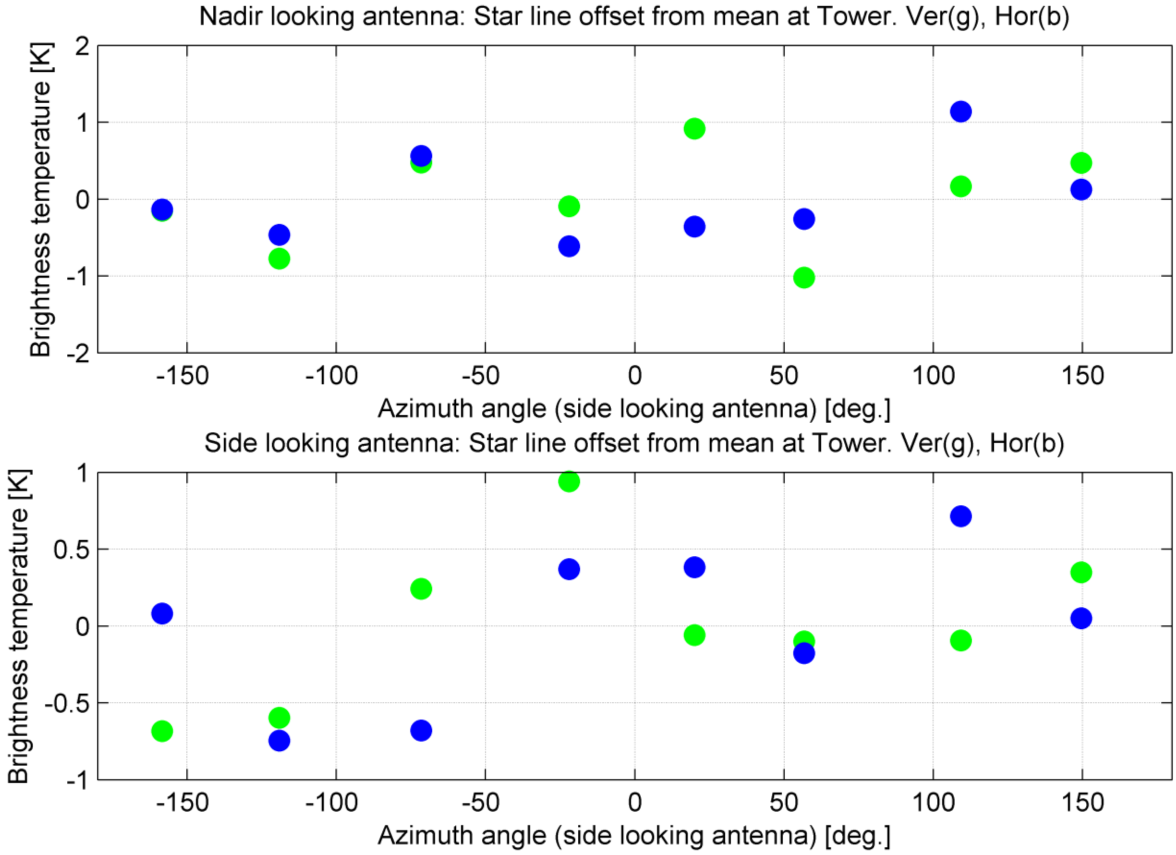


Figure 6.4.2: Star lines offset from mean value of all star lines at American Tower.

| **Star line** | **Nadir looking antenna [K]** | | **Side looking antenna [K]** | |
|---|---|---|---|---|
| | **V-pol** | **H-Pol** | **V-Pol** | **H-Pol** |
| 1 | 199.907 | 199.875 | 209.645 | 186.936 |
| 2 | 199.283 | 199.547 | 209.731 | 186.108 |
| 3 | 200.534 | 200.571 | 210.570 | 186.174 |
| 4 | 199.962 | 199.397 | 211.270 | 187.224 |
| 5 | 200.975 | 199.654 | 210.270 | 187.237 |
| 6 | 199.035 | 199.753 | 210.229 | 186.678 |
| 7 | 200.222 | 201.151 | 210.236 | 187.569 |
| 8 | 200.530 | 200.134 | 210.678 | 186.904 |
| Mean | 200.056 | 200.010 | 210.328 | 186.854 |
| Standard deviation | 0.654 | 0.590 | 0.523 | 0.515 |

*Table 6.4.2: Star lines brightness temperature at American Tower.*

### 6.5 Comparison with geophysical parameters

The spatial variation in data and the fact that no area was observed systematically throughout the campaign rules out the possibility of determining a brightness temperature dependence on the ambient temperature, pressure or humidity during the campaign. It is theoretically not possible to determine to which extend different brightness temperatures measured at different areas at different times are due to spatial variations or changed geophysical parameters such as temperature, pressure or humidity. The tie line crossings with the survey lines presented in the previous paragraph could have provided such data. However, the results of these do not depend on whether the survey lines were flow on the same day or on different days. The only geophysical parameters that could be addressed were the sun and the galactic background radiation, and these parameters has been addressed in Chapter 3. Therefore no further analysis has been performed.

# 7. POLARIMETRIC DATA

## 7.1 V and H statistics

As both V and H polarizations for all survey and tie lines are show in paragraph 6.1, this paragraph only contains a statistical analysis of the difference between V and H polarization, provided in Table 7.1.1.

| Survey Line | Nadir looking antenna | | | Side looking antenna | | |
|---|---|---|---|---|---|---|
| | **Mean [K]** | **S.Dev. [K]** | **Correlation** | **Mean [K]** | **S.Dev. [K]** | **Correlation** |
| 1 | 0.254 | 1.173 | 0.606 | 25.451 | 0.867 | 0.812 |
| 2 | 0.455 | 0.882 | 0.714 | 24.223 | 0.831 | 0.839 |
| 3 | -0.087 | 1.198 | 0.671 | 23.650 | 0.783 | 0.826 |
| 4 | -0.531 | 1.328 | 0.594 | 23.872 | 0.725 | 0.891 |
| 5 | -0.389 | 0.564 | 0.955 | 24.228 | 0.563 | 0.967 |
| 6 | -0.184 | 0.404 | 0.920 | 23.590 | 0.943 | 0.578 |
| 7 | -0.920 | 1.139 | 0.686 | 23.122 | 0.821 | 0.833 |
| 8 | -0.516 | 1.391 | 0.552 | 23.542 | 0.893 | 0.853 |
| 9 | 0.033 | 1.007 | 0.843 | 23.746 | 0.665 | 0.947 |
| 10 | -0.965 | 1.392 | 0.882 | 22.542 | 1.000 | 0.979 |
| 11 | -0.666 | 0.979 | 0.958 | 21.486 | 1.108 | 0.984 |
| Tie | -0.851 | 1.564 | 0.930 | 23.495 | 1.514 | 0.978 |

*Table 7.1.1: Statistic properties of the difference between V and H polarization for both nadir and side looking antenna.*

The statistic difference between V and H polarization in Table 7.1.1 shows that there is a low standard deviation and a high correlation between V and H polarizations for both nadir and side looking antenna. The slightly lower correlation between V and H polarizations for the nadir looking antenna compared to the side looking antenna is probably due to the low mean and higher standard deviation for the difference between V and H polarizations for the nadir looking antenna.

## 7.2 3rd Stokes

Figure 7.2.1 shows the 3rd Stokes parameter for survey line 5 both nadir and side looking antenna. This appearance is typical for all the survey lines. A rather constant value of 0 to -2K for the nadir looking antenna and a constant value of -1 to -3 K for the side looking antenna. The non-zero value is not significant: no special attempt to fully calibrate 3rd and 4th Stokes was carried out, and by default a bias of 1 or 2 K is typical for the EMIRAD instrument (without careful polarimetric calibration). More noise in the nadir looking antenna than in the side looking antenna as is also seen for V and H polarizations. There is no obvious explanation for this difference. So, the interesting observation is that there is no tendency east-west. Some of the profiles were flown east-west, others west-east. No differences observed. The small peak around 303 km in the side looking antenna data could be RFI from Concordia.

Figure 7.2.2 shows the 3rd Stokes for the tie line. In contrast to the normal grid lines, a clear tendency is noted in the side looking plot.

In conclusion, the 3rd Stokes parameter may vary as a function of latitude, but not as a function of longitude.

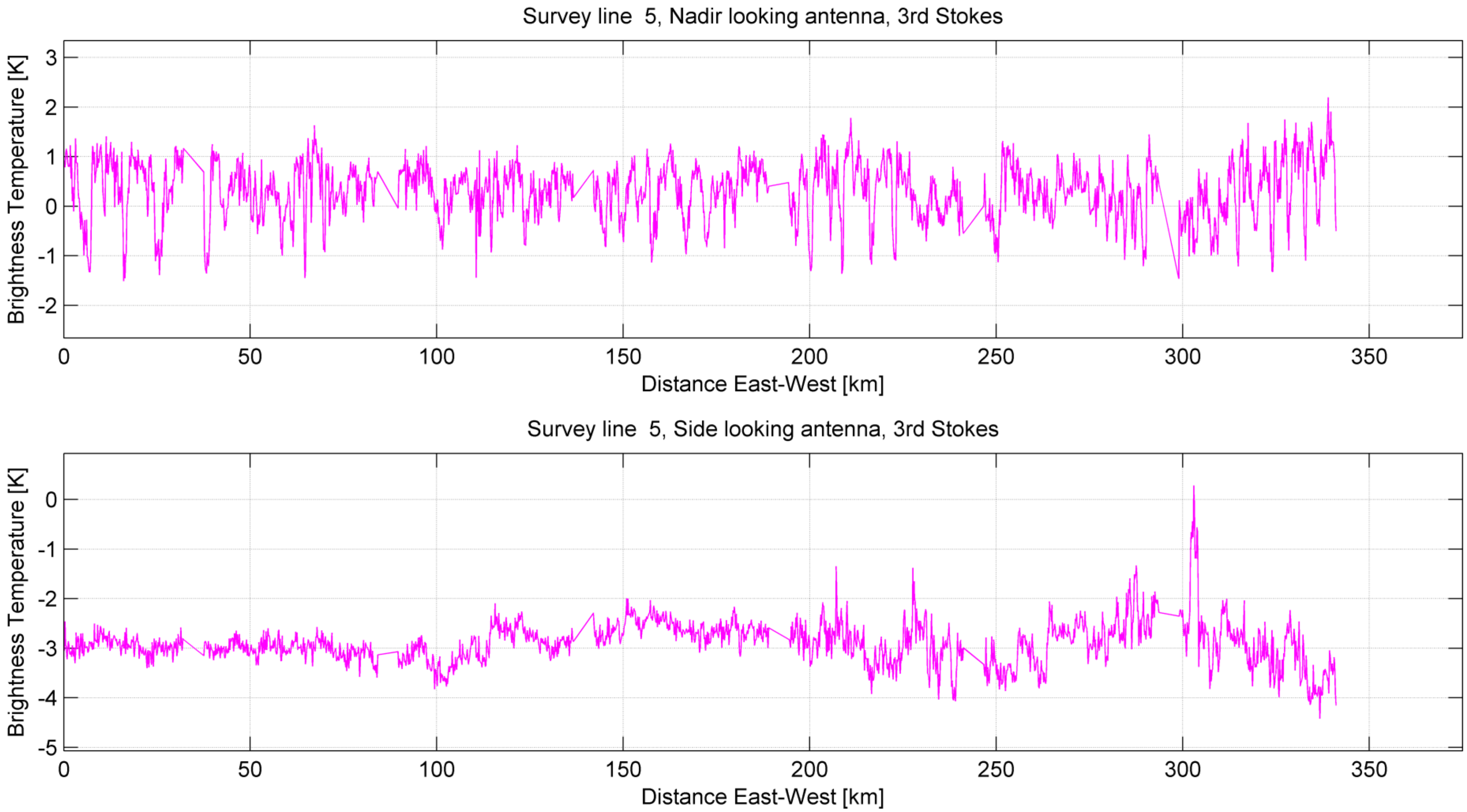


Figure 7.2.1: Third Stokes for survey line 5 both nadir and side looking antenna.

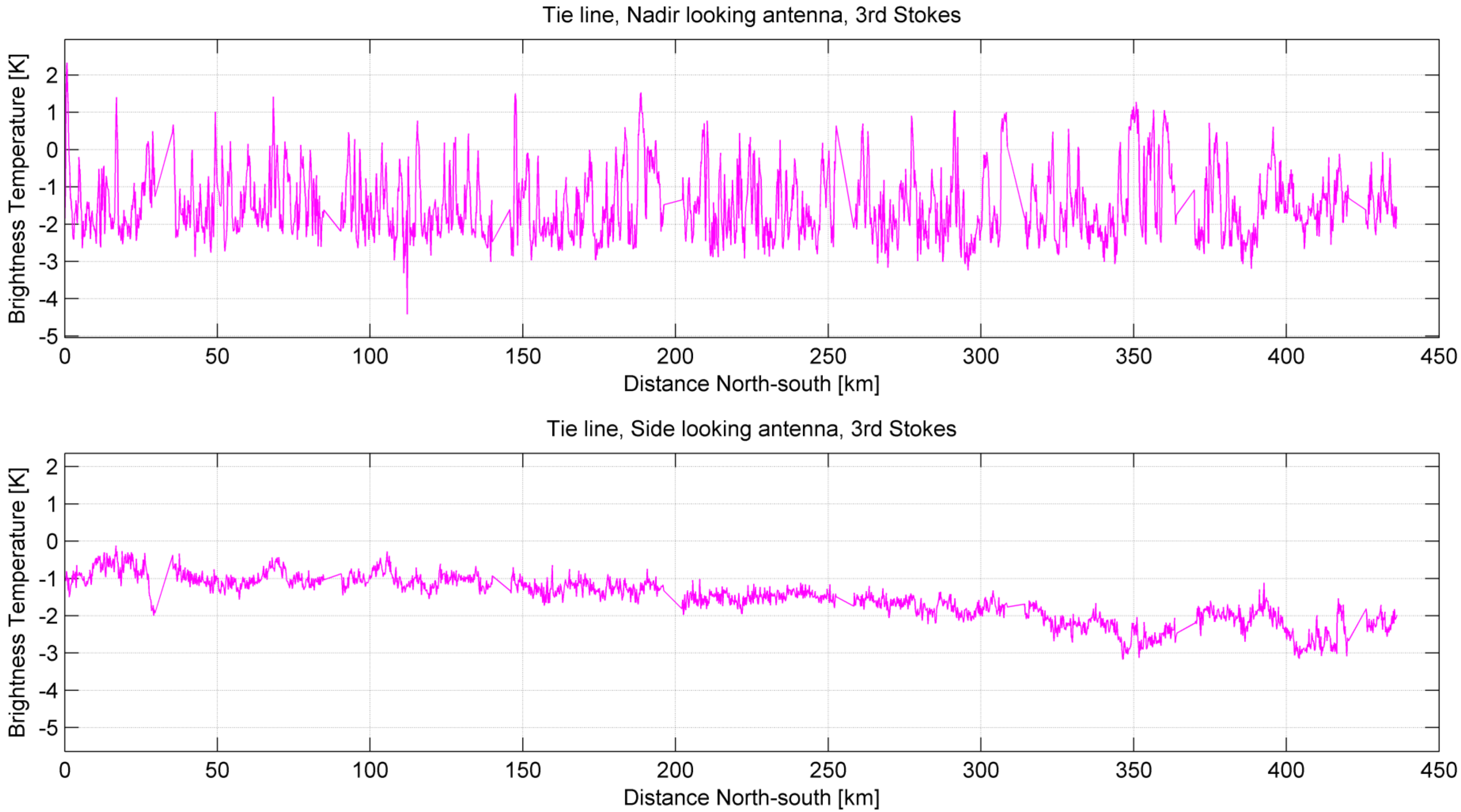


Figure 7.2.2: Third Stokes for tie line both nadir and side looking antenna.

!

### 7.3 4th Stokes

Figure 7.3.1 shows the 4th Stokes parameter for survey line 5 both nadir and side looking antenna. This appearance is typical for all the survey lines. An almost constant level of 0 or a few K for the both antennas. The non-zero value is not significant: no special attempt to fully calibrate 3rd and 4th Stokes was carried out, and by default a bias of 1 or 2 K is typical for the EMIRAD instrument (without careful polarimetric calibration). The 4th Stokes parameter does not have the larger fluctuations in the nadir antenna seen in V, H and 3rd Stokes data. There is a small peak around 298 km in the side look antenna data that could be RFI from Concordia.

Figure 7.2.2 shows the 4th Stokes for the tie line. In contrast to the normal grid lines, a weak tendency is noted in the side looking data. In conclusion, the 4th Stokes parameter may be a weak function of latitude, but not a function of longitude.

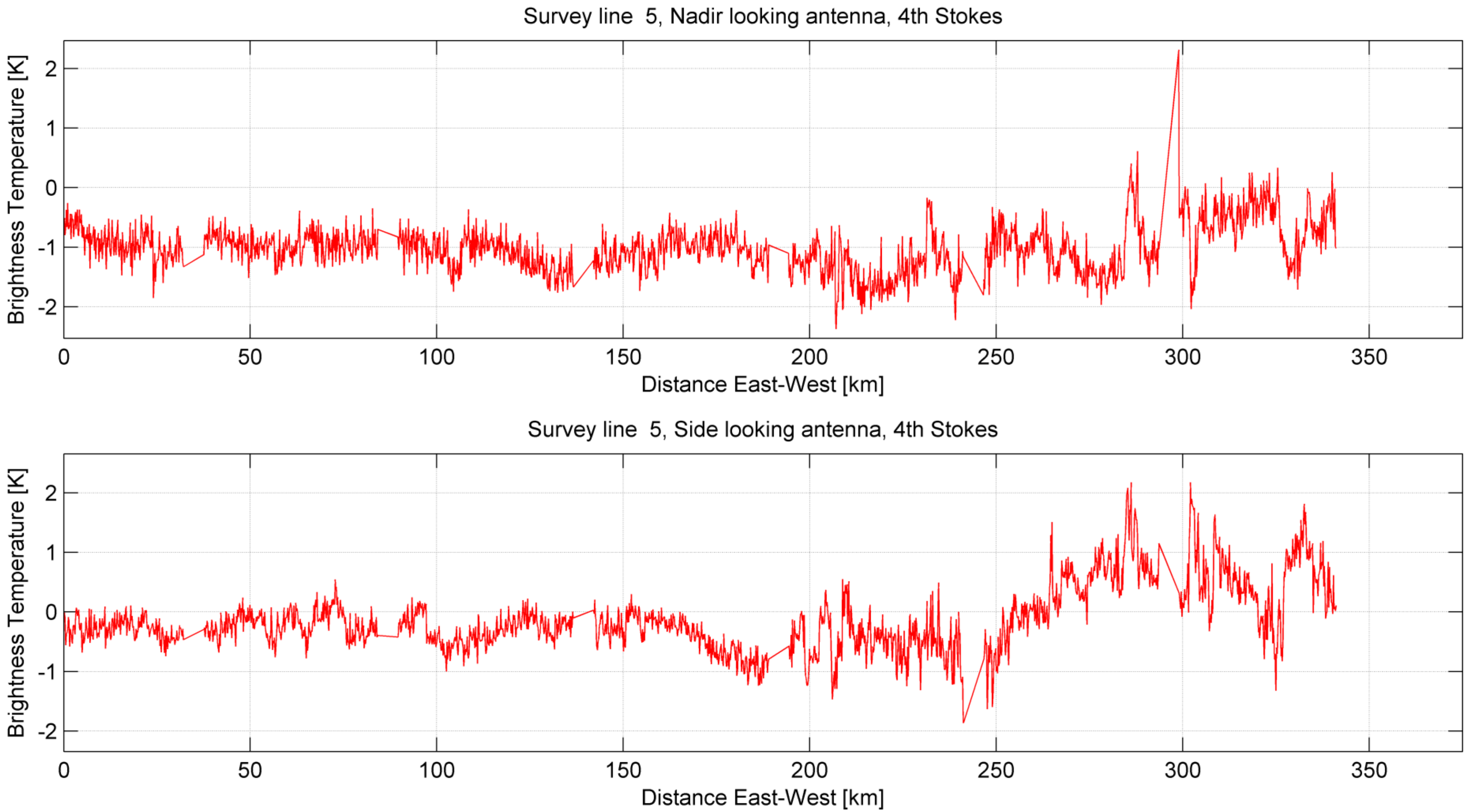


Figure 7.3.1: Fourth Stokes for survey line 5 both nadir and side looking antenna.

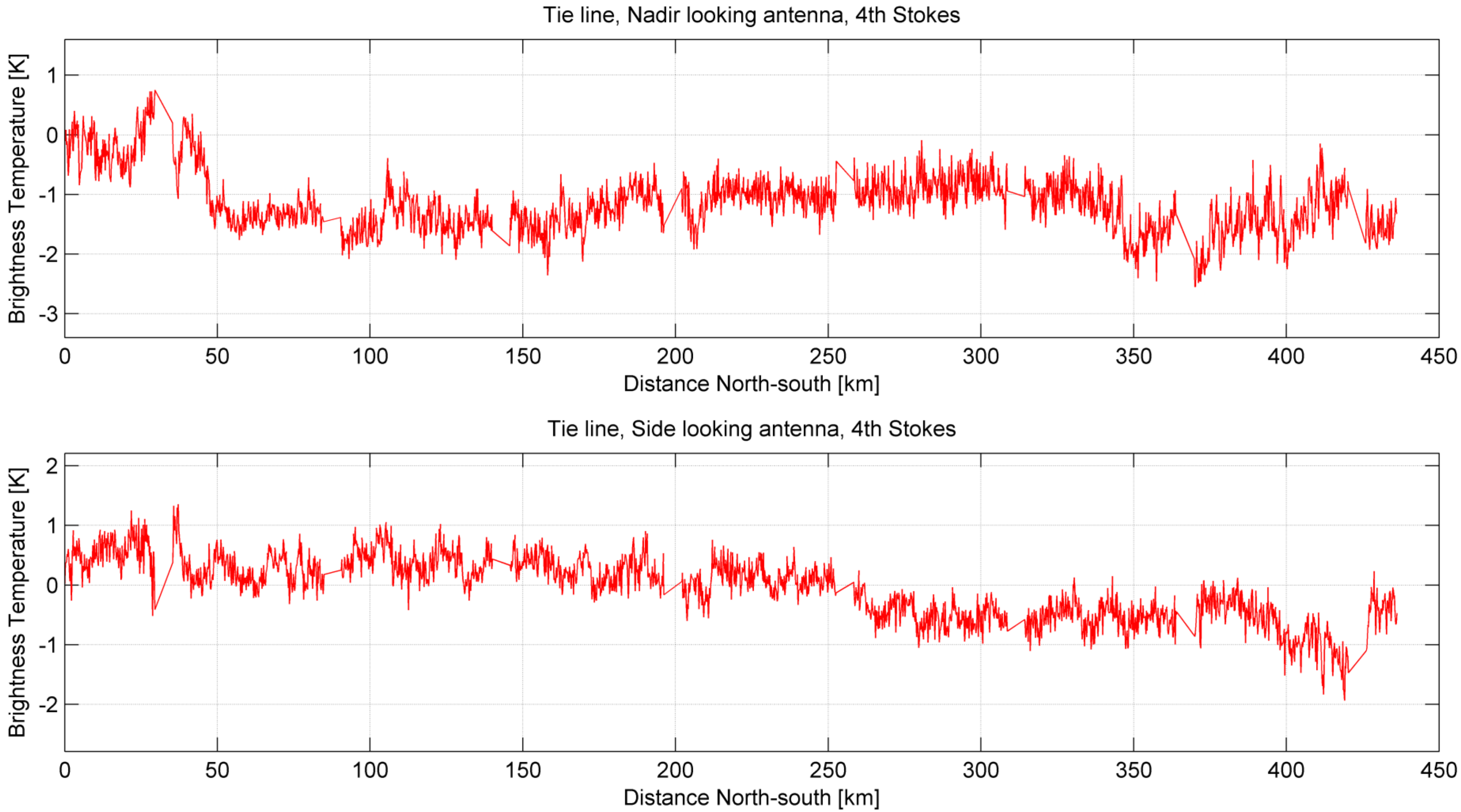


Figure 7.3.2: Fourth Stokes for tie line both nadir and side looking antenna.

## 8. SPATIAL SPECTRUM ANALYSIS

The results so far clearly show a spatial inhomogeneity that was not expected and it is thus necessary to analyze this spatial inhomogeneity in more details. Figure 8.1 shows the power spectrum of survey line 5, side looking antenna data as a function of spatial frequency using a double logarithmic display.

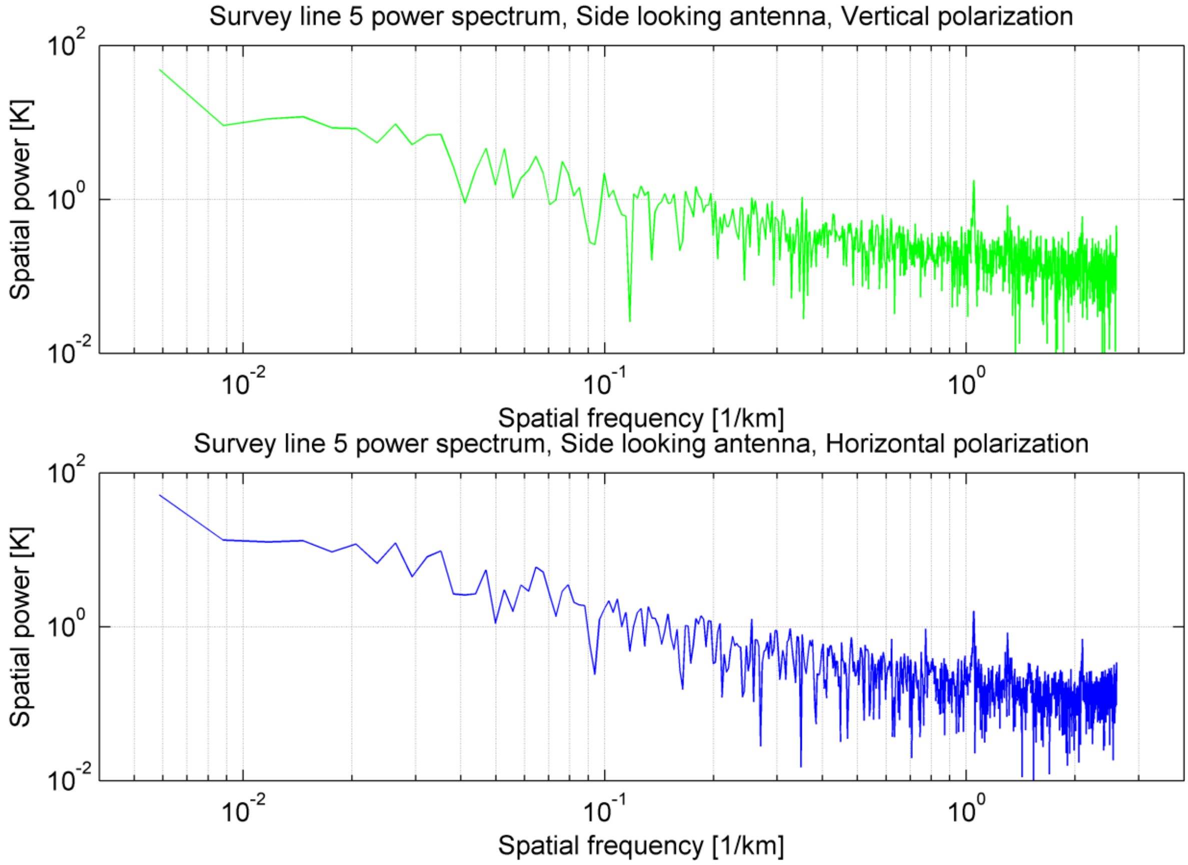


Figure 8.1: The power spectra of survey line 5, side looking antenna.

The power spectra in Figure 8.1 show a clear 1/f dependence from a wavelength spanning the entire survey line down to approximately 1 km wherefrom the spectra slowly level out at approximately 0.1K consistent with a ΔT of 0.1K. Some small peaks in is also seen around a wavelength of 1 km.

The power spectra for both antennas of all other survey lines and the tie line look like the spectra shown in Figure 8.1. The small peaks seen in Figure 8.1 are also present in the power spectra for the other survey and tie lines but their locations shift and in some cases only the peak around 1 km is clear. These peaks are therefore considered random.

The power spectra of the nadir looking antenna, see Figure 8.2, level out level at a systematically slightly higher level than the side looking antenna consistent with what has previously been seen.

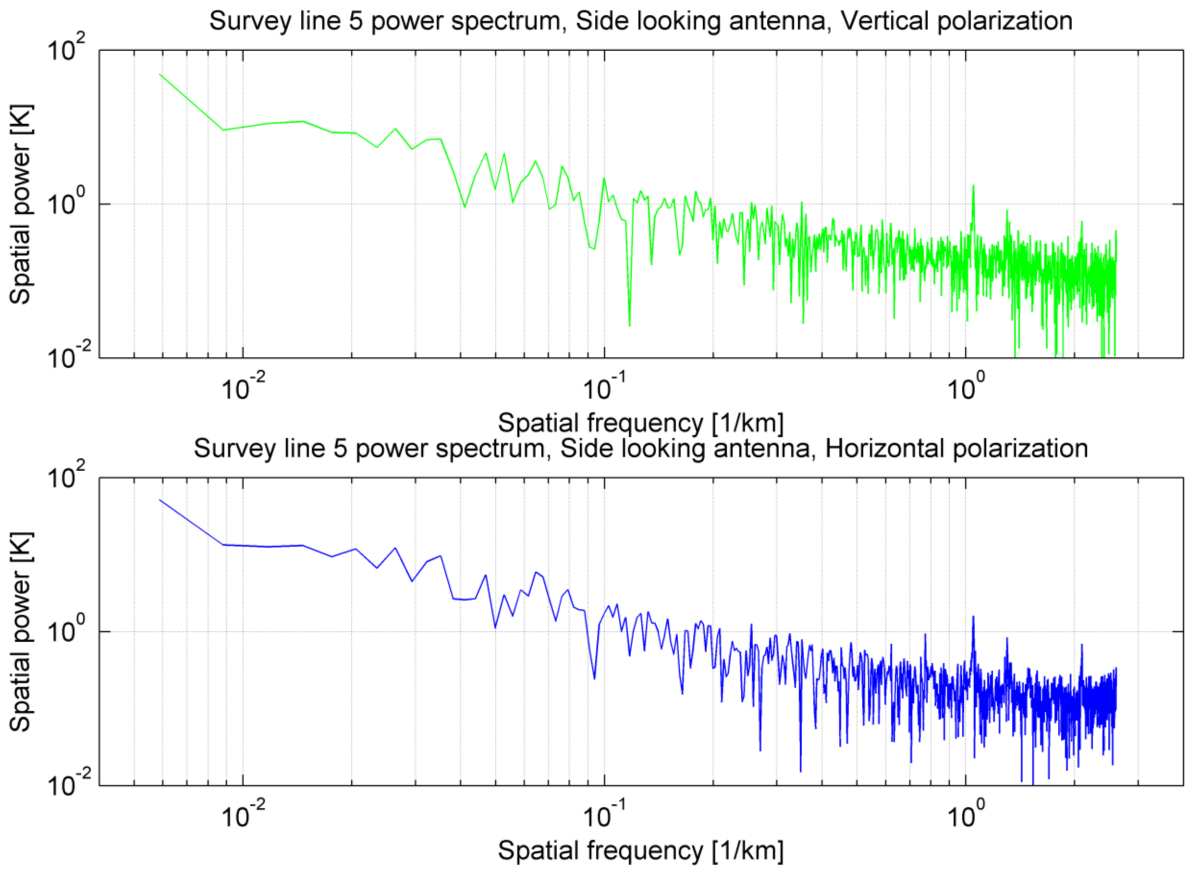


Figure 8.2: The power spectrum of survey line 5, nadir looking antenna.

The 1/f dependence of the power spectra for all the survey lines show that there is no preferred wavelength of the spatial variation observed and suggest a fractal or multiscale process. The spatial variations are not random with a fixed standard deviation as this would have given flat spectra. The spatial variation increases with distance and at wavelengths comparable to the 3dB width of SMOS and Aquarius, the spectral power is in the order of 10K, wherefore also the spatial spectrum analysis shows significant variations.

## 9 COMPARISON WITH SMOS DATA

The EMIRAD data was recorded from January 17th to January 22nd. wherefore all SMOS data within the same time frame has been processed for comparison with EMIRAD data. The 1524 SMOS Earth grid points used are shown in Figure 9.1.

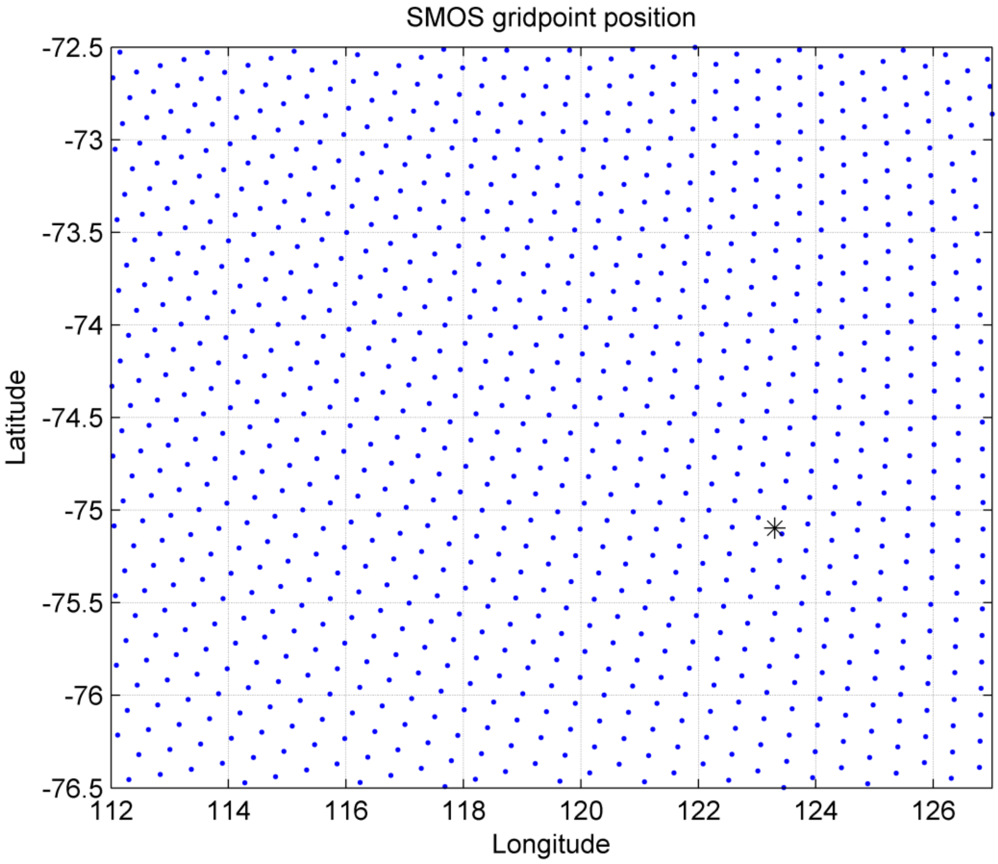


Figure 9.1: The SMOS Earth grid points used for comparison with EMIRAD data. Concordia is marked by an asterisk.

As the SMOS data is homogeneously distributed it was decided to interpolate SMOS data to the locations where EMIRAD data was recorded. Only EMIRAD data recorded by the side looking antenna at 45º is compared to SMOS data as nadir looking data from SMOS is questionable. SMOS data is not recorded at specific incidence angles, but for each swath a number of incidence angle samples are recorded for each grid point. If at least five incidence angle samples from one grid point are recorded during a swath and the incidence angle 45º is within the minimum and maximum value of the incidence angles of these samples, these samples are used to generate one estimate of the brightness temperature at 45º incidence angle for that grid point. The estimate is generated by applying a second order polynomial fit to all samples at the grid point and using the value of that fit at 45º incidence angle. Hence, only one brightness temperature was estimated for a grid point for each swath. However, each grid point in Figure 9.1 was covered by 7 to 21 swaths, wherefore each grid point had from 7 to 21 estimates. Taking the mean value for each grid point for all swaths produced one brightness temperature for each grid point shown in Figure 9.1. These data was used to make the 2D imagery of SMOS V and H polarization data shown in Figures 9.2 and 9.3, respectively. The area displayed and temperature scales used are the same as for the EMIRAD 2D imagery in paragraph 5.1 to ease comparison.

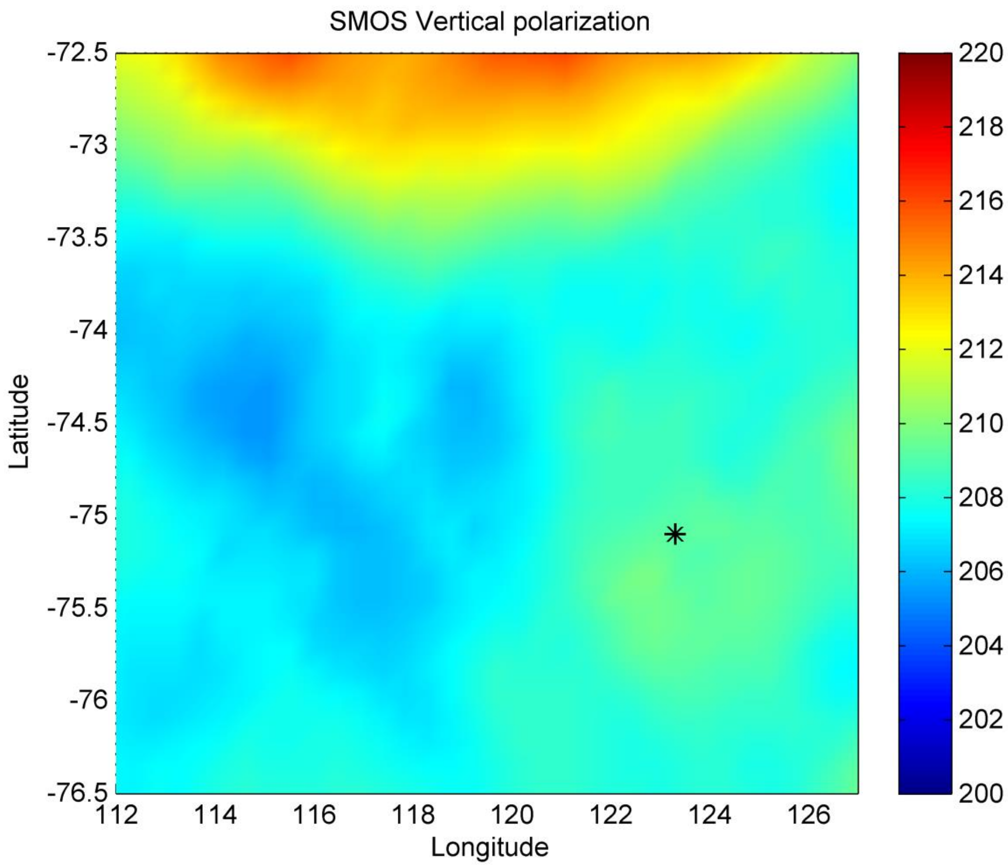


Figure 9.2: SMOS vertical polarization data at 45º incidence angle. Concordia is marked by an asterisk.

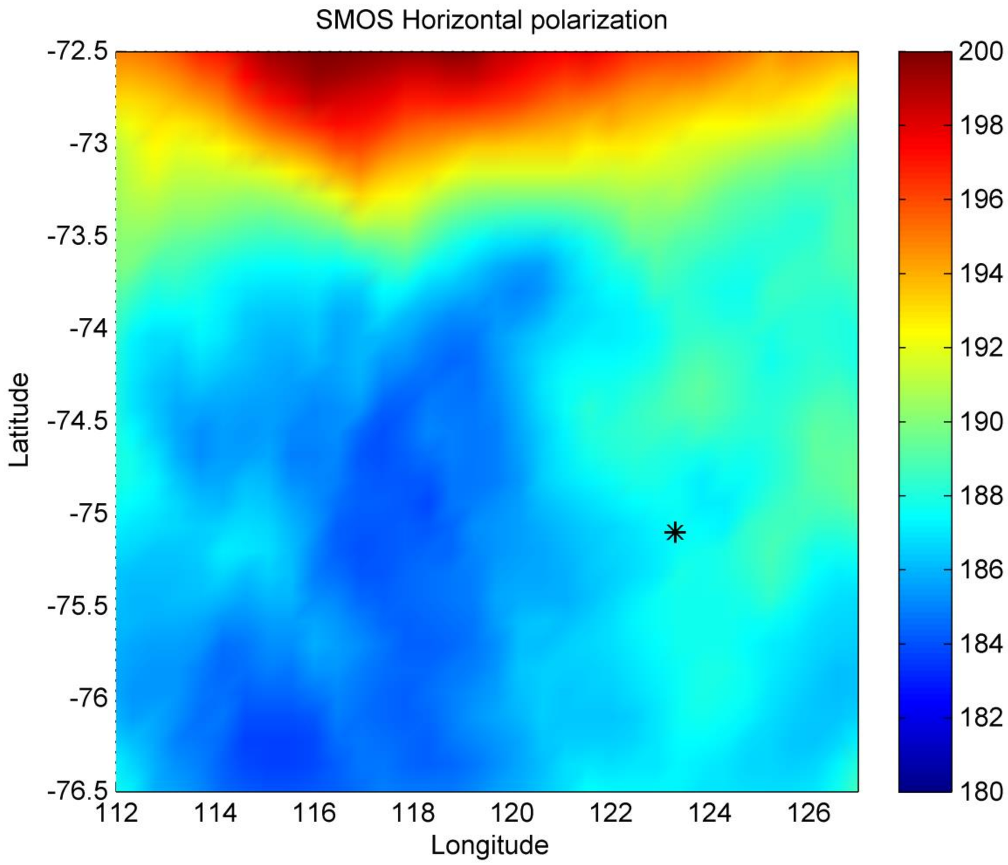


Figure 9.2: SMOS horizontal polarization data at 45º incidence angle. Concordia is marked by an asterisk.

When comparing the 2D imagery of SMOS data with the 2D imagery of EMIRAD data in paragraph 5.1 it is obvious that there are similarities but also differences. And it is necessary to address these differences. The mean value at each grid point used for generating 2D imagery was also used to generate interpolated SMOS data for each 1 second integrated EMIRAD sample, both vertical and horizontal polarization. Figures 9.4 and 9.5 show EMIRAD data, SMOS data resampled to EMIRAD data location and the difference between EMIRAD and SMOS data for vertical and horizontal polarizations, respectively.

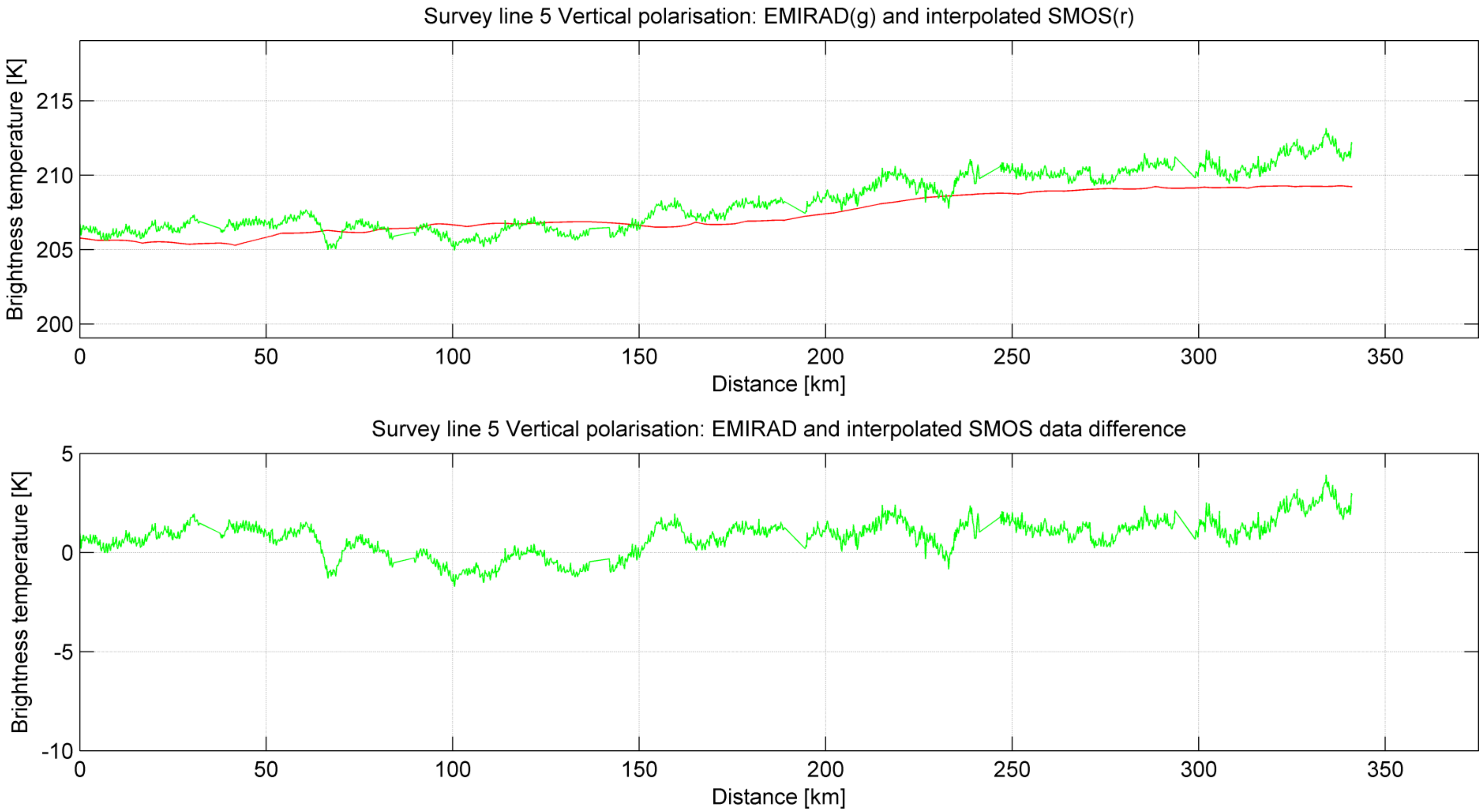


Figure 9.4: Comparison of EMIRAD and SMOS data, vertical polarization.

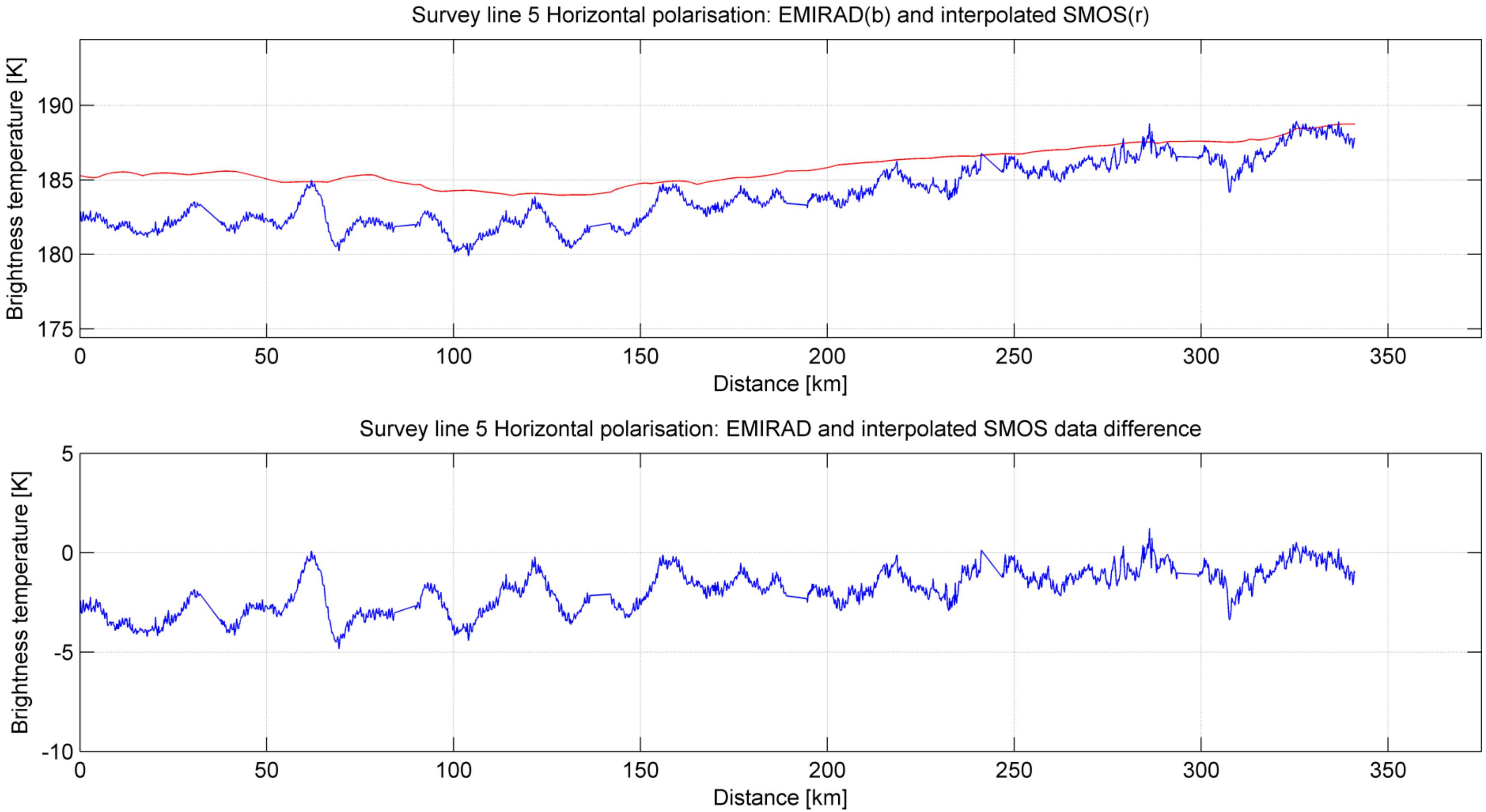


Figure 9.5: Comparison of EMIRAD and SMOS data, horizontal polarization.

The Figures 9.4 and 9.5 are typical for all survey lines. The vertical polarization fits well while the horizontal polarization seems to have an offset of 3 K. The statistics shown in Table 9.1 confirms these results.

| **Survey line** | **Mean value [K]** | | **Standard deviation [K]** | |
|---|---|---|---|---|
| | **V-pol** | **H-pol** | **V-pol** | **H-pol** |
| 1 | -1.10 | -4.42 | 0.64 | 0.65 |
| 2 | -0.56 | -3.04 | 1.04 | 0.62 |
| 3 | -0.78 | -2.88 | 0.61 | 0.77 |
| 4 | -0.81 | -3.01 | 0.51 | 0.52 |
| 5 | 0.80 | -1.90 | 0.92 | 1.11 |
| 6 | -1.49 | -3.99 | 1.15 | 1.65 |
| 7 | -0.84 | -3.35 | 0.70 | 0.98 |
| 8 | -0.07 | -3.09 | 0.68 | 1.25 |
| 9 | -0.17 | -3.71 | 0.95 | 1.14 |
| 10 | -0.55 | -3.73 | 1.21 | 1.27 |
| 11 | -0.41 | -3.53 | 1.01 | 1.27 |
| Average | -0.54 | -3.33 | 0.86 | 1.02 |

*Table 9.1: Statistics on EMIRAD to SMOS data difference for the survey lines.*

In Table 9.1 it is noted that when averaging for all survey lines the SMOS offset from EMIRAD data is -0.5 K for vertical polarization and -3.3 K for horizontal polarization. No explanations for this offset have been found.

# 10. DISCUSSION AND RECOMMENDATIONS

The purpose of this campaign was to assess the merits of the East Antarctic Plateau around Dome C with the Concordia station as a candidate for an Earthly calibration site. The temporal stability has been assessed in the DOMEX framework, so the main purpose of this campaign was to assess the spatial homogeneity of this area. To this purpose a 350 x 350 km area within latitude -77 to -72 and longitude 112 to 126 was selected. This area was surveyed by profiling the brightness temperature along 11 survey lines each being 350 km long and separated by 35 km across. A tie line crossing all survey lines was also recorded.

A star pattern centered on the American Tower (the site of the DOMEX radiometer next to Concordia) of 8 lines at 8 different headings was also flown in order to compare data with DOMEX data and to assess de details around Concordia.

Two circle flights were flown in order to assess azimuth signatures and other azimuth dependent effects such as the sun and the galactic background radiation. In order to separate these effects, one circle flight was flown during forenoon while the other was flown during afternoon (not on the same day) so that there was a shift in the Earth rotation angle of approximately 90 degrees between the two circle flights. It is evident, that the Sun is far the most important concern. It appears clearly in all azimuth signatures, and a worst case of 8 K contribution is found, when looking directly to the reflected Sun at H-Pol. At the -20 dB limit of the antenna patterns (48 degrees off bore sight for nadir looking horn and 38 degrees off bore sight for the side looking horn) a contribution of 200-300 mK from the Sun is still present, although the level should be only 80 mK for perfect flat surface reflection. However, the scattering seems to affect only observations close to the -20 dB limit, and going extra 10 degrees off bore sight removes the contribution completely, Hence the requirement for the flight tracks pointing the side looking antenna more than 45 degrees (azimuth angle not bore sight angle) away from the sun is justified. The Galactic background theoretically adds a down welling contribution up to approximately 6 K at worst case, but reflected contributions from the galactic background could not be identified; possibly due to the Sun position being close to the galactic center for both circle flights and the reflected contribution being too weak. Some azimuth signatures, not connected to neither the Sun nor the Galaxy, were identified; especially for the 3$^{rd}$ and 4$^{th}$ Stokes parameters at higher incidence angles. The geophysical cause for the signatures is not known, but survey data indicate, that the target area for the circle flights is not completely homogeneous.

All EMIRAD data was calibrated according to a three step calibration scheme. First, internal calibration is applied, using two of three built-in calibration sources, Matched Load, Active Cold Load, and Noise Diode. The third calibration point validates the actual calibration, which turns out to be very stable throughout the whole campaign duration. Second, microwave cables between the antennas and the receivers are calibrated out using a liquid Nitrogen cooled target, right before or right after each flight, whenever possible. This calibration step shows very consistent results, and estimated parameters for each cable are well in line with factory specifications. For all channels, results are extremely stable throughout the entire campaign. The third calibration step calibrates out the antennas and the Orthomode transducers, using values found in the laboratory, using a Vector Network Analyzer.

All calibration data is validated using data from a test flight over the ocean, where wing wags, i.e. large scale variation of the incidence angle, were performed. All data channels show offsets, compared to expected values, but as no in-situ data (wind speed and percentage of ice cover) directly from the test area is available, the absolute level cannot be determined. Wing wags over the ice target area confirms the presence of offsets between channels, and values, similar to those from the test flight are estimated. However, as no external calibration site is available close to the target area, no validation of the absolute level can be made, and the desired absolute accuracy of 1 K, aimed at during previous SMOS related campaigns, cannot be guaranteed. Most likely the offsets are caused by small changes in the S-parameters for the antenna system, when installed in the aircraft. Such changes are very stable, and general stability is confirmed by very similar values for the offsets when measured at different flights throughout the campaign.

Concerning RFI, global statistics shows that some 3.7% of the data from the nadir horn was flagged and about 1.4 % from the side looking horn. Removing these data has an insignificant effect on ΔT, but a significant effect on the brightness temperature. It must therefore be concluded that there is significant RFI in Antarctica, but mitigation is possible.

Already the simple overview of brightness temperatures imposed on the flight track lines shown in Chapter 4 indicate an unexpected high variation. This is supported by the 2D data obtained by interpolating survey and tie lines shown in Chapter 5. The high brightness temperatures in the northern end of the area was expected as the altitude is lower, but the inhomogeneities seen around Concordia and at the proposed calibration site west of Concordia were unexpected. The proposed calibration site cannot be detailed further in the 2D data but the star lines centered on the American Tower allow a more detailed 2D image near Concordia showing inhomogeneities of several K within a few km radius from Concordia.

The detailed analysis of the profiles in Chapter 6 shows that the inhomogeneities are present in all survey and tie lines but dominated by the higher brightness temperatures in the northern part of the survey area. A slope of almost 1K per km over several km is seen when zooming in on details. It is also shown using along track simulations that when comparing two sensors with different 3dB footprint widths such as SMOS and Aquarius the inhomogeneities will produce systematic differences between the two sensors of several tenths of K and the peak-peak variation in the difference is more than 1 K. Statistical analysis of the difference between simulated SMOS and Aquarius data shows systematic negative difference which is due to the fact that the proposed calibration site almost at the center of the survey area is some form of local minima which SMOS resolved better due to its higher spatial resolution.

Analysis of data indicates an unexpected high difference in brightness temperatures when comparing different lines crossing each other. No obvious explanation for this result is found. The slightly lower standard deviation of the star line crossings above the American Tower compared to the survey tie line crossings could indicate a larger variation due to the larger time spacing in the survey line recording, but this is not supported when observing survey lines recorded on the same flight, i.e. with time spacing comparable to the star line recording. The statistics on the difference between V and H polarizations show results without any surprises. High correlations, expected mean values and slightly higher standard deviations for the nadir looking antenna compared to the side looking antenna due to higher noise level for the nadir looking antenna. The 3$^{rd}$ and 4$^{th}$ Stokes parameters show no east to west dependence while a weak 1 to 2 K trend in the north to south direction can be observed. This is not significant.

The spatial spectrum analysis shows a clear 1/f trend for spatial wavelength spanning from the entire survey length down to 1 km or less and leveling out at 0.1K at shorter wavelengths. This indicates a multiscale process with a correlation length that increases with the length of the profiles and no preferred wavelength.

Based on the results presented above, it can be concluded that the survey area contains spatial inhomogeneities that will affect the brightness temperature measured by SMOS. The brightness temperature measured by SMOS may shift several tenths of a K if the sampling location is shifted just within less than the 3dB width of the footprint. Absolute calibration of SMOS with tenths of a K accuracy using the East Antarctic Plateau therefore requires a careful characterization of the test site.

The effects of these inhomogeneities is also illustrated clearly when comparing simulated SMOS and Aquarius data where the difference may change several tenths of K depending on spatial location of the samples. Hence, inter calibration of these two sensors also requires either a well characterized area in order to compensate for these spatial inhomogeneities or an area large enough to remove these differences by averaging.

## 11. REFERENCES


Macelloni, G., M. Brogioni, S. Pettinato, F. Montomoli, F. Monti, and T. Casal: "L-band Characterization of Dome-C Region using Ground and Satellite Data", IGARSS'13, pp. 3427 – 3440, July 2013.

Kristensen, S. S.: "DOMECair Campaign. EMIRAD Data Acquisition Report", v. 1.1, DTU Space, Technical University of Denmark, April 2013.

Skou, N. and R. Forsberg: "DOMECair Campaign Implementation Plan", v. 1.2, DTU Space, Technical University of Denmark, November 2012.

Søbjærg, S. S., S. S. Kristensen, J. Balling, and N. Skou: "The Airborne EMIRAD L-band Radiometer System", IGARSS'13, pp. 1900-1903, July 2013.

# DOMECair Campaign
# EMIRAD data acquisition report – Part I

Version 1.1

Prepared by
Steen Savstrup Krisensen
DTU Space

## DISTRIBUTION LIST

| Name | Organization | Issue | Date |
|---|---|---|---|
| Malcolm Davidson | ESA | 1.1 | 19/4/13 |
| Tânia Casal | ESA | 1.1 | 19/4/13 |
| Daniel Steinhage | AWI | 1.1 | 19/4/13 |
| Giovanni Macelloni | IFAC | 1.1 | 19/4/13 |
| Niels Skou | DTU-Space | 1.0 | 19/4/13 |
| Sten Søbjerg Smidl | DTU-Space | 1.0 | 19/4/13 |
| Jan Balling | DTU-Space | 1.0 | 19/4/13 |
| Steen Savstrup Kristensen | DTU-Space | 1.2 | 19/4/13 |

## DOCUMENT CONTROL DATA

| Issue | Revision | Date | Description |
|---|---|---|---|
| 1 | 0 | 19/4/13 | Draft for internal review |
| 1 | 1 | 30/4/13 | First edition |

## Contents

# 1 Introduction

This report gives an overview of the EMIRAD-2 radiometer system data acquired during the DOMECair Campaign taking place over Antarctica January 2013.

# 2 Instrumentation

As this report only describes data acquired with the EMIRAD-2 radiometer system, only this instrument is described in this chapter. The EMIRAD-2 L-band radiometer system has been developed by DTU, and operated by DTU in a range of campaigns, known as the CoSMOS campaigns, in support of SMOS. It is a fully polarimetric (4 Stokes parameters) system with advanced RFI detection features (kurtosis and polarimetry). The system has operated successfully on different aircrafts (Aero Commander and Skyvan) in Denmark, Norway, Finland, Germany, France, Spain, Australia). The main features of the system are:

- Correlation radiometer with direct sampling
- Fully polarimetric (i.e. 4 Stokes parameters)
- Frequency: 1400.5 – 1426.5 MHz (-3 dB BW)<br>1392 - 1433 (-60 dB BW)
- Digital radiometer with 139.4 MHz sampling
- Digital I/Q demodulation and correlation for accurate estimation of 3rd and 4th Stokes
- Advanced analogue filter for RFI suppression.
- Additional digital filter bank: 4 sub-bands.
- RFI flagging by kurtosis and polarimetry.
- Data integrated to 1 msec recorded on primary storage PC.
- "Fast data" pre-integrated to 14.4 μsec. recorded on dedicated PC.
- Sensitivity: 0.1 K for 1 sec. integration time
- Stability: better than 0.1 K over 15 min. before internal calibration.
- Calibration: internal load, noise diode, and Active Cold Load (ACL).
- 2 antennas - one nadir pointing, one side looking at 45 deg. incidence angle
- Antennas are Potter horns with 37.6 deg & 30.6 deg HPBW
- Nadir horn has 415 m footprint from 2000 ft flight altitude
- Tilted horn has 490 m by 640 m footprint, again from 2000 ft flight altitude.
- Each data package time stamped using GPS 1PPS signal with 100 ns accuracy.
- Minimum operating altitude: 250 m above terrain @ 140 knots

Further information about EMIRAD-2 is found in [Skou et al, 2006] and [Skou et al, 2010].

The installation and functionality of the radiometer system on-board the aircraft was tested during a test flight off Bremerhaven carried out September 24.

# 3 Data overview

This Chapter provides tables for the campaign flights, the transit flights, the installation verification flight, the liquid nitrogen calibrations and the navigation data acquired during the DOMECAir campaign.

A list of notes common to all tables is provided in the last paragraph of this chapter.

## 3.1 Campaign flights

**Table 3.1** provides a list of the EMIRAD data recorded during the campaign flights that took place near Concordia polar station.

| Date | Time (UTC) | Purpose | Special circumstances | Notes |
|---|---|---|---|---|
| 20130117 | 01:43-03:53 | Circle flight AM | Initial part of flight data not available due to missing time synchronization data | a) |
| 20130117 | 06:38-10:10 | Line 1 and 4 | | a) |
| 20130118 | 00:48-04:57 | Tie Line and Line 11 | | a) |
| 20130118 | 06:32-10:03 | Line 7 and 10 | | a) |
| 20130119 | 00:50-04:27 | Star pattern | Internal calibrations scheduled manually to ensure mapping over tower. | b) |
| 20130119 | 06:26-09:10 | Line 5 and 6 | | |
| 20130121 | 05:47-08:18 | Line 8 and 9 | | |
| 20130121 | 08:19-11:10 | Circle flight PM | | |
| 20130122 | 05:58-08:51 | Line 2 and 3 | | |

Table 3.1: EMIRAD data recorded during campaign flights.

**Figure 3.1** shows the campaign flights flown from Concordia.

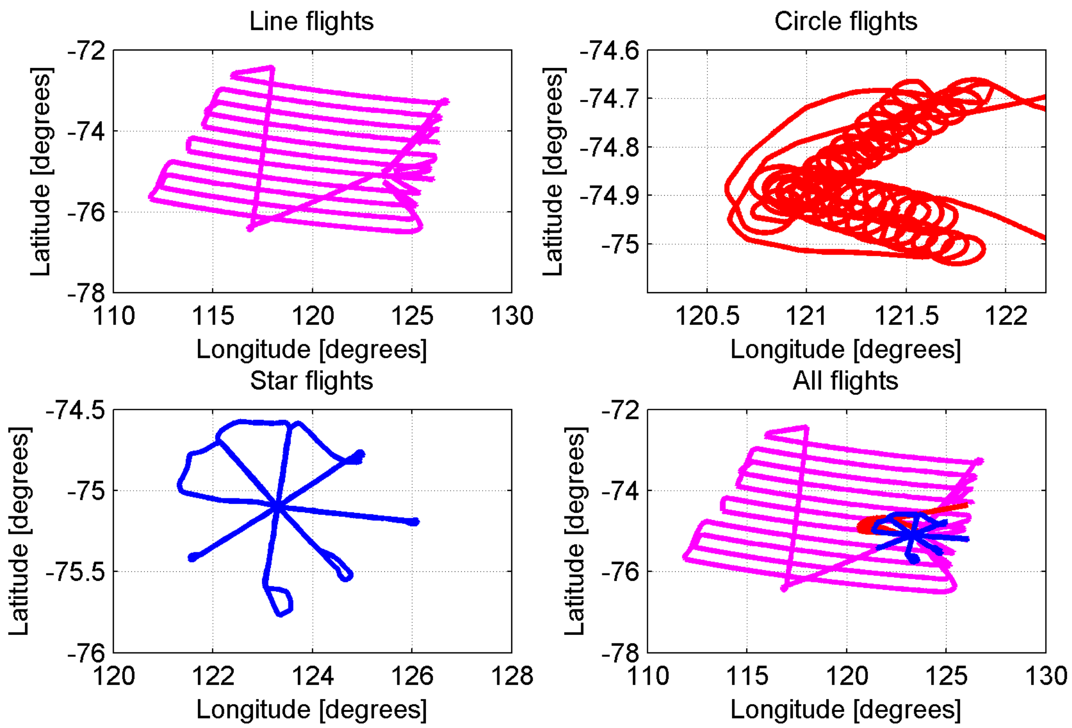


Figure 3.1: Campaign flights for recording the lines.

## *3.2 Transit flights*

**Table 3.2** provides a list of the EMIRAD data recorded during transit flights from the installation base Novo to Concordia and back.

| Date | Time (UTC) | Route | Special circumstances | Notes |
|---|---|---|---|---|
| 20130113 | 14:36-16:13 | Novo-Kohnen | Data not valid due to power supply failure | |
| 20130113 | 18:05-23-22 | Kohnen-South | Data not valid due to power supply failure | |
| 20130115 | 20:14-23:18 | South-Concordia | Data not valid due to power supply failure | c) d) |
| 20130115 | 23:37-00:32 | South-Concordia | Data not valid due to power supply failure | c) d) |
| 20130116 | 00:57-01:14 | South-Concordia | Data not valid due to power supply failure | c) d) |
| 20130122 | 13:38-13:51 | Concordia-Concordia | | e) |
| 20130122 | 14:00-14:50 | Concordia-Concordia | | |
| 20130123 | 02:00-02:39 | Concordia-South | | e) |
| 20130123 | 02:43-07:35 | Concordia-South | | |
| 20130123 | 09:10-14:30 | South-Kohnen | | d) |
| 20130124 | 09:15-09:43 | Kohnen-Novo | Data not reliable due to EGI problems | b) e) |
| 20130124 | 09:46-11:09 | Kohnen-Novo | Data not reliable due to EGI problems | b) |

Tabel 3.2: EMIRAD data recorded during Transit Flights EMIRAD.

**Figure 3.2** provides an overview of the transit flights.

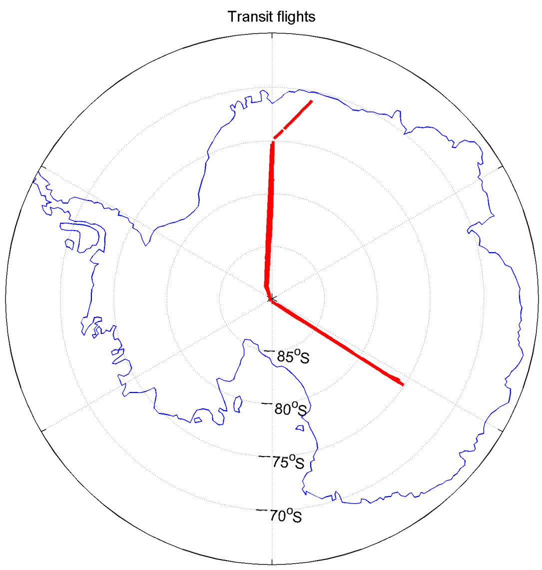


Figure 3.2: Transit flights overview

## 3.3 Instrument validation flight

**Table 3.3** provides a list of the EMIRAD data recorded during the instrument validation flight that took place over the ocean north of Novo.

| Date | Time (UTC) | Route | Special circumstances | Notes |
|---|---|---|---|---|
| 20130112 | 11:03-11:38 | Novo-Ocean | | |
| 20130112 | 11:43-12:00 | Ocean Nose and Wing wags | Instrument validation maneuverers. | |
| 20130112 | 12:04-12:31 | Ocean-Novo | | |

Tabel 3.3: Instrument validation flight EMIRAD data

**Figure 3.3** shows the instrument validation flight. Blue and magenta colours show the transit flights from Novo to ocean and back while read shows the nose and wing wags performed over the ocean to validate the radiometer.

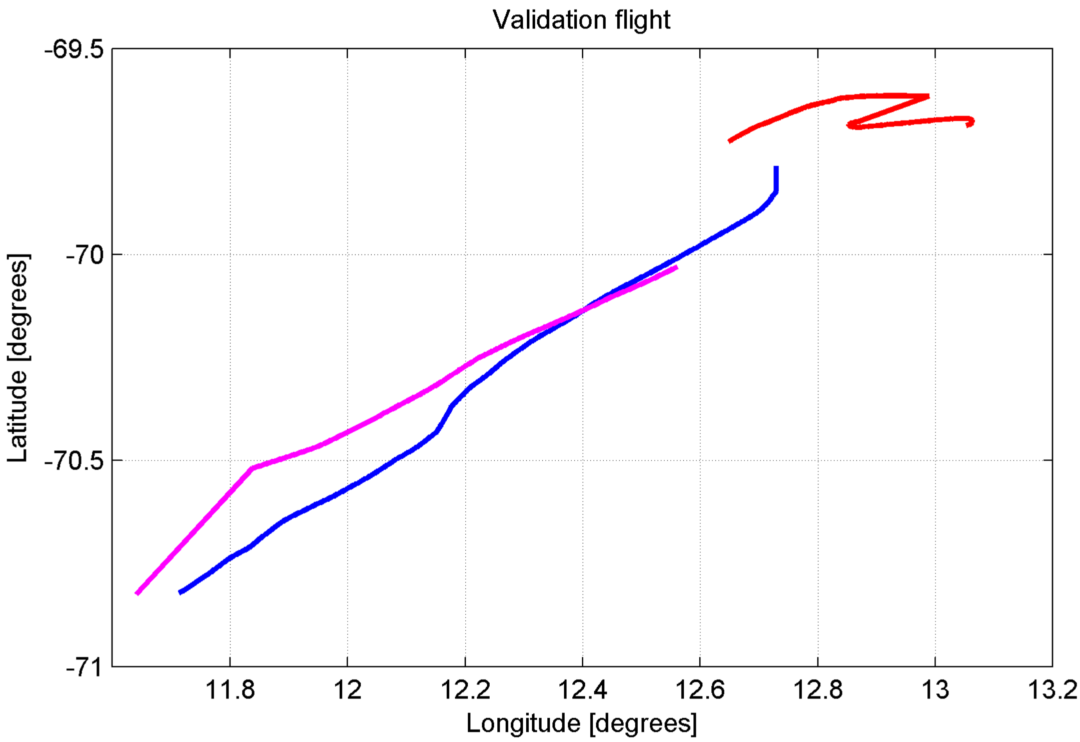


Figure 3.3: Instrument validation flight.

## 3.4 Liquid Nitrogen calibrations

**Table 3.4** provides a list of the liquid nitrogen calibrations preformed at Concordia. The EGI was not turned on during liquid nitrogen calibrations; hence these data are not time stamped.

| Date | When | Special circumstances |
|---|---|---|
| 20130117 | Before afternoon flight | Calibration done twice in succession to assess repeatability. |
| 20130118 | Before morning flight | |
| 20130119 | Before morning flight | Calibration done twice to asses temperature drifts |
| 20130119 | Before afternoon flight | Calibration done twice in succession to assess repeatability. |
| 20130120 | Never | LN2 was evaporated. No time to get more. |
| 20130121 | Before morning flight | Done three times. The first to assess repeatability of high THB value. The third after a complete system restart to assess repeatability of high THB value. Calibration results not usable. |

Table 2.4: LN2 Calibrations at Concordia.

## 3.5 Navigation data

**Table 3.5** provides a list of the navigation data recorded during all flights.

| Date | When (UTC) | Route | Special circumstances | Notes |
|---|---|---|---|---|
| 20130112 | 11:03-11:38 | Novo-Ocean | | |
| 20130112 | 11:43-12:00 | Ocean Nose and Wing wags | | |
| 20130112 | 12:04-12:31 | Ocean-Novo | | |
| 20130113 | 14:36-16:13 | Novo-Kohnen | | |
| 20130113 | 18:05-23-22 | Kohnen-South | Problems with GPS when approaching 90 S. | |
| 20130115 | 20:14-23:18 | South-Concordia | | d) |
| 20130115 | 23:37-00:32 | South-Concordia | | d) |
| 20130116 | 00:57-01:14 | South-Concordia | | d) |
| 20130117 | 01:43-03:53 | Circle flight AM | | a) |
| 20130117 | 06:38-10:10 | Line 1 and 4 | | a) |
| 20130118 | 00:48-04:57 | Tie Line and Line 11 | | a) |
| 20130118 | 06:32-10:03 | Line 7 and 10 | | a) |
| 20130119 | 00:50-04:27 | Star pattern | | b) |
| 20130119 | 06:26-09:10 | Line 5 and 6 | | |
| 20130121 | 05:47-08:18 | Line 8 and 9 | | |
| 20130121 | 08:19-11:10 | Circle flight PM | | |
| 20130122 | 05:58-08:51 | Line 2 and 3 | | |
| 20130122 | 13:38-13:51 | Concordia-Concordia | | |
| 20130122 | 14:00-14:50 | Concordia-Concordia | | |
| 20130123 | 02:00-02:39 | Concordia-South | | |
| 20130123 | 02:43-07:35 | Concordia-South | | |
| 20130123 | 09:10-14:30 | South-Kohnen | | d) |
| 20130124 | 09:15-09:43 | Kohnen-Novo | | f) |
| 20130124 | 09:46-11:09 | Kohnen-Novo | | f) |

Table 3.5: Navigation data recorded from all flights.

### 3.6 Table notes:

a) Fast data and filter bank data missing due to problems with the fast data storage PC.
b) Problems with EGI altitude update from GPS.
c) Restarts performed while trying to identify the instrument error
d) Degraded navigation data as the EGI cannot align south of latitude -80 deg.
e) Instrument restart after setting new internal temperature target due to new ambient temperature inside aircraft.
f) GPS failure in the EGI.

# 4 Processing

### 4.1 Calibration

The data set has been calibrated according to the following scheme:

1) Internal calibrations are used to characterise internal system gain and noise, including the effects of internal physical temperature variations.

2) LN2 measurements have been carried out during the campaign. These are used to characterise the losses in the antenna cables and validate the internal calibrations.

3) Laboratory measured characteristics of the EMIRAD antennas and OMTs have been taken into account. This is considered sufficient as these are robust passive components. Measurements during nose and wing wags over ocean are used to validate the calibration, but any effect of actual installation on the antenna pattern has not been assessed.

### 4.2 Integration and RFI mitigation

Data have been integrated to 1 second integration time, which provides oversampling with respect to antenna footprint size. Prior to temporal integration, the following has been carried out:

1) The data set has been screened for RFI by evaluating kurtosis, polarimetric, and TB anomalies.

All data samples found to be affected by RFI have been removed from the data set. This, however, does not guarantee that the data samples still contained within the data set are indeed free from RFI.

2) Due to a mechanical problem with one of the microwave switches of the EMIRAD system, the horizontal channel of the side-looking antenna from time to time exhibits elevated brightness temperature levels. These elevated levels are easily detectable, and have been removed from the data set.

3) The data set has been corrected with respect to antenna rotation.

# 5 Data inventory

**Table 5.1** provides a list of the data files constituting the processed output of the EMIRAD-2 radiometer from the DOMECAir Campaign January 2013. There are separate files for the nadir and side looking antennas. Both files contain both radiometer data and navigation data.

All recorded data are listed in the table below, but only valid data are included in the inventory. In the case of invalid or questionable data, such data is not provided and the term “NA” (Not Available) is used to signify this.

## 5.1 Inventory table

| Date | When (UTC) | Route | Nadir looking Antenna | Side looking Antenna |
|---|---|---|---|---|
| 20130112 | 11:03-11:38 | Novo-Ocean | 01211030.e61 | 01211030.e62 |
| 20130112 | 11:43-12:00 | Ocean Nose and Wing wags | 01211430.e61 | 01211430.e62 |
| 20130112 | 12:04-12:31 | Ocean-Novo | 01212040.e61 | 01212040.e62 |
| 20130113 | 14:36-16:13 | Novo-Kohnen | NA | NA |
| 20130113 | 18:05-23-22 | Kohnen-South | NA | NA |
| 20130115 | 20:14-23:18 | South-Concordia | NA | NA |
| 20130115 | 23:37-00:32 | South-Concordia | NA | NA |
| 20130116 | 00:57-01:14 | South-Concordia | NA | NA |
| 20130117 | 01:43-03:53 | Circle flight AM | 01701430.e61 | 01701430.e62 |
| 20130117 | 06:38-10:10 | Line 1 and 4 | 01706380.e61 | 01706380.e62 |
| 20130118 | 00:48-04:57 | Tie Line and Line 11 | 01800480.e61 | 01800480.e62 |
| 20130118 | 06:32-10:03 | Line 7 and 10 | 01806320.e61 | 01806320.e62 |
| 20130119 | 00:50-04:27 | Star pattern | 01900500.e61 | 01900500.e62 |
| 20130119 | 06:26-09:10 | Line 5 and 6 | 01906260.e61 | 01906260.e62 |
| 20130121 | 05:47-08:18 | Line 8 and 9 | 02105470.e61 | 02105470.e62 |
| 20130121 | 08:19-11:10 | Circle flight PM | 02108190.e61 | 02108190.e62 |
| 20130122 | 05:58-08:51 | Line 2 and 3 | 02205580.e61 | 02205580.e62 |
| 20130122 | 13:38-13:51 | Concordia-Concordia | 02213380.e61 | 02213380.e62 |
| 20130122 | 14:00-14:50 | Concordia-Concordia | 02214000.e61 | 02214000.e62 |
| 20130123 | 02:00-02:39 | Concordia-South | 02302000.e61 | 02302000.e62 |
| 20130123 | 02:43-07:35 | Concordia-South | 02302430.e61 | 02302430.e62 |
| 20130123 | 09:10-14:30 | South-Kohnen | 02309100.e61 | 02309100.e62 |
| 20130124 | 09:15-09:43 | Kohnen-Novo | NA | NA |
| 20130124 | 09:46-11:09 | Kohnen-Novo | NA | NA |

Table 5.1: DOMECAir campaign EMIRAD data inventory (NA: Not Available).

## 5.2 Data format

Data is provided as ASCII files with 14 columns each. All data files follow the naming convention "`xxxhhmm0.zzz`" where

`xxx` = day of year

`hh` = Hour at start of measurement (UTC)

`mm` = Minute at start of measurement (UTC)

`zzz` = File type, which can be one of the following:

`e61` : Calibrated data from nadir antenna

`e62` : Calibrated data from side-looking antenna

The content of each column is given in **Table 5.2**.

| Column | Definition |
|---|---|
| 1 | Measurement time, UTC [UNIX time] (http://en.wikipedia.org/wiki/Unix_time) |
| 2 | Vertical TB [Kelvin] |
| 3 | Horizontal TB [Kelvin] |
| 4 | 3rd Stokes parameter [Kelvin] |
| 5 | 4th Stokes parameter [Kelvin] |
| 6 | Aircraft position latitude [degrees] |
| 7 | Aircraft position longitude [degrees] |
| 8 | Aircraft altitude [m] |
| 9 | Aircraft roll [degrees, positive numbers correspond to right turn] |
| 10 | Aircraft pitch [degrees, positive numbers correspond to nose up] |
| 11 | Aircraft true heading, relative to Earth North [degrees, positive numbers = east, negative numbers = west] |
| 12 | Antenna incidence angle, antenna boresight in relation to nadir [degrees] |
| 13 | Antenna pointing angle, antenna boresight in relation to north [degrees, positive numbers = east, negative numbers = west] |
| 14 | Antenna rotation, antenna reference frame in relation to Earth reference frame [degrees] |

Table 5.2: Contents of each column for file types `e61` and `e62`.

# 6 Conclusion

The data acquisition was a success as all data at the campaign site was acquired according to plans except a small fraction of one of the four circle flight tracks. However, this missing fractions does not affect the outcome as the assessment of a possible azimuth signature may be derived from the acquired data.

# 7 References

Skou, N., S. S. Søbjærg, J. Balling, and S. S. Kristensen: "A Second Generation L-band Digital Radiometer for Sea Salinity Campaigns", Proceedings of IGARSS'06, 4p., July 2006.

Skou, N., S. S. Søbjærg, J. Balling, S. S. Kristensen, and A. Kusk: "EMIRAD-2 and its use in the SMOS Cal/Val Campaign“, DTU Space, AR 502, pp. 1-59, June 2010.